JAMES | Journal of Advances in Modeling Earth Systems

RESEARCH ARTICLE
10.1029/2023MS003922

The Land Component LM4.1 of the GFDL Earth System Model ESM4.1: Model Description and Characteristics of Land Surface Climate and Carbon Cycling in the Historical Simulation

E. Shevliakova[1], S. Malyshev[1], I. Martinez-Cano[2], P. C. D. Milly[3], S. W. Pacala[4], P. Ginoux[1], K. A. Dunne[9], J. P. Dunne[1], C. Dupuis[5], K. L. Findell[1], K. Ghannam[6], L. W. Horowitz[1], T. R. Knutson[1], J. P. Krasting[1], V. Naik[1], P. Phillipps[1], N. Zadeh[1], Yan Yu[7], F. Zeng[1], and Y. Zeng[8]

[1]NOAA Geophysical Fluid Dynamics Laboratory, Princeton, NJ, USA, [2]Le Laboratoire des Sciences du Climat et de l'Environnement, IPSL-LSCECEA/CNRS/UVSQ Saclay, Gif-sur-Yvette, France, [3]NOAA/GFDL Affiliate, Princeton, NJ, USA, [4]Department of Ecology and Evolutionary Biology, Princeton University, Princeton, NJ, USA, [5]Lamont-Doherty Earth Observatory, Columbia Climate School, Palisades, NY, USA, [6]Department of Civil and Environmental Engineering, Northeastern University, Boston, MA, USA, [7]Peking University, Beijing, China, [8]University of Maryland, Baltimore, MD, USA, [9]Retired

Key Points:

- A new land model LM4.1 is developed at the Geophysical Fluid Dynamics Laboratory (GFDL) for the next-generation Earth System Model (ESM) ESM4.1
- LM4.1 integrates age-height structured vegetation dynamics, multi-layer canopy-soil-snow energy exchanges, and prognostic fires and mineral dust
- ESM4.1/LM4.1 improves patterns of land surface climate and carbon cycle compared to the previous generation GFDL model ESM2G/LM3.0

Correspondence to:
E. Shevliakova,
Elena.Shevliakova@noaa.gov

Citation:
Shevliakova, E., Malyshev, S., Martinez-Cano, I., Milly, P. C. D., Pacala, S. W., Ginoux, P., et al. (2024). The land component LM4.1 of the GFDL Earth System Model ESM4.1: Model description and characteristics of land surface climate and carbon cycling in the historical simulation. *Journal of Advances in Modeling Earth Systems*, *16*, e2023MS003922. https://doi.org/10.1029/2023MS003922

Received 7 AUG 2023
Accepted 15 JAN 2024

Author Contributions:
Conceptualization: E. Shevliakova, S. Malyshev
Data curation: E. Shevliakova, S. Malyshev
Formal analysis: E. Shevliakova, S. Malyshev, I. Martinez-Cano, P. C. D. Milly, P. Ginoux, K. A. Dunne, C. Dupuis, K. L. Findell, K. Ghannam, T. R. Knutson, Yan Yu, F. Zeng, Y. Zeng

Abstract We describe the baseline model configuration and simulation characteristics of the Geophysical Fluid Dynamics Laboratory (GFDL)'s Land Model version 4.1 (LM4.1), which builds on component and coupled model developments over 2013–2019 for the coupled carbon-chemistry-climate Earth System Model Version 4.1 (ESM4.1) simulation as part of the sixth phase of the Coupled Model Intercomparison Project. Analysis of ESM4.1/LM4.1 is focused on biophysical and biogeochemical processes and interactions with climate. Key features include advanced vegetation dynamics and multi-layer canopy energy and moisture exchanges, daily fire, land use representation, and dynamic atmospheric dust coupling. We compare LM4.1 performance in the GFDL Earth System Model (ESM) configuration ESM4.1 to the previous generation component LM3.0 in the ESM2G configuration. ESM4.1/LM4.1 provides significant improvement in the treatment of ecological processes from GFDL's previous generation models. However, ESM4.1/LM4.1 likely overestimates the influence of land use and land cover change on vegetation characteristics, particularly on pasturelands, as it overestimates the competitiveness of grasses versus trees in the tropics, and as a result, underestimates present-day biomass and carbon uptake in comparison to observations.

Plain Language Summary The Geophysical Fluid Dynamics Laboratory (GFDL) has developed a new Land Model (LM4.1) as part of its 4th generation coupled model development. This model includes advances from the previous generation and introduces a new vegetation demography model, multi-layer canopy, plant hydraulics, fire, and land use representation as well as dynamic atmospheric dust coupling. Coupled within an Earth System Model (ESM4.1), LM4.1 features an improved representation of many ecological processes from the previous generation of GFDL ESMs.

1. Introduction

More than four decades ago, the possibility of anthropogenic climate change driven by CO_2 emissions from fossil fuel consumption and deforestation motivated global carbon cycle studies with a simplified representation of climate-carbon interactions (Broecker et al., 1979; Siegenthaler & Oeschger, 1978). Grassl (2000) argued that to increase understanding of climate system variability and to make long-term projections of climate change, the scientific community needs to develop "a 3D general circulation model of the global atmosphere coupled to the 3D world ocean, including sea ice dynamics and a representation of land surface processes (including vegetation)." Concurrently, Cox et al. (2000) demonstrated the possibility of carbon-cycle feedback that amplified climate change using a fully coupled, three-dimensional carbon-climate model HadCM3 with a prognostic component able to predict sub-grid fractions of different vegetation types.

The Coupled Model Intercomparison Project, Phase 5 (CMIP5 Taylor et al., 2012) had contributions from six coupled carbon-climate Earth System Models (ESMs) with prognostic vegetation distribution capabilities (as

Funding acquisition: E. Shevliakova
Investigation: E. Shevliakova, S. Malyshev, J. P. Krasting
Methodology: E. Shevliakova, S. Malyshev, P. C. D. Milly, S. W. Pacala, P. Ginoux, J. P. Dunne, L. W. Horowitz, V. Naik
Project administration: E. Shevliakova, J. P. Dunne
Resources: S. W. Pacala, J. P. Dunne
Software: E. Shevliakova, S. Malyshev, I. Martinez-Cano, P. Ginoux, P. Phillipps, N. Zadeh
Supervision: E. Shevliakova, J. P. Dunne
Validation: E. Shevliakova, S. Malyshev, P. C. D. Milly, S. W. Pacala, P. Ginoux, J. P. Dunne, P. Phillipps, N. Zadeh
Visualization: E. Shevliakova, S. Malyshev, I. Martinez-Cano, P. C. D. Milly, P. Ginoux, K. A. Dunne, C. Dupuis, K. L. Findell, K. Ghannam, T. R. Knutson, Yan Yu, F. Zeng, Y. Zeng
Writing – original draft: E. Shevliakova, S. Malyshev, I. Martinez-Cano, P. C. D. Milly, P. Ginoux, C. Dupuis, K. L. Findell, K. Ghannam, Y. Zeng
Writing – review & editing: E. Shevliakova, S. Malyshev, P. C. D. Milly, S. W. Pacala, P. Ginoux, J. P. Dunne, K. L. Findell, L. W. Horowitz, J. P. Krasting, V. Naik

opposed to a prescribed current vegetation distribution used in pre-industrial, historical, idealized, and future scenarios experiments), including two ESMs from Geophysical Fluid Dynamics Laboratory (GFDL), ESM2M and ESM2G (Dunne et al., 2012, 2013). Both GFDL ESMs used the land model LM3.0 (Shevliakova et al., 2009, 2013). Since CMIP5, climate centers pursued different strategies for improving the representation of land-atmosphere interactions such as coupled carbon-nitrogen-phosphorus cycling (e.g., E3SM (Q. Zhu et al., 2019)); plant hydraulics, soil water, and snow processes (e.g., CESM/CLM5 (Lawrence et al., 2019)), energy and moisture coupling at the soil/atmosphere interface (e.g., IPSL-CM6A-LR (Cheruy et al., 2020)), and water resources and crop management with land use decision-making model based on economic activities (e.g., MIROC-INTEG-LAND (Yokohata et al., 2020)). In the above examples, as in most other ESMs, vegetation distributions are prescribed on unmanaged lands and their fractions are modified via land-use scenarios while ignoring the effects of climate change on biogeography (i.e., vegetation type).

There are only *five* CMIP6 ESMs with prognostic dynamic vegetation distribution capabilities: UKESM1 (Sellar et al., 2019), MPI-ESM1.2 (Mauritsen et al., 2019), AWI-ESM (Shi et al., 2020), EC-Earth3 (Döscher et al., 2022), and GFDL-ESM4.1 (Dunne et al., 2020a). The first three models include a first-generation dynamic global vegetation model (DGVM)—updated TRIFFID (Harper et al., 2018) and JSBACH (Reick et al., 2021) and an earlier version of JSBACH (Stevens et al., 2013)—characterized by a simplified treatment of plants' structure and competition. Only two ESMs, EC-Earth3 and GFDL ESM4.1, attempted to include second-generation vegetation models with an explicit treatment of ecosystem demography, particularly age-height structured vegetation competition for light. However, while EC-Earth3 includes an ecosystem demography model LPJ-GUESS (Smith et al., 2001, 2014), its land surface HTESSEL (Balsamo et al., 2009) and vegetation dynamics (and thus terrestrial carbon cycle) components do not have a consistent treatment of soil water and energy exchanges; that is, plants and the hydrological cycle "experience" different states of water. To our knowledge, LM4.1 is the first land component with a fully consistent treatment of ecosystem demography, multi-layer ($n > 2$) vegetation canopy, and land surface processes, used in the Diagnostic, Evaluation, and Characterization of Klima (DECK) CMIP6 (Eyring et al., 2016) simulations as well as in projection scenarios (ScenarioMIP; B. C. O'Neill et al., 2016), the coupled climate-carbon cycle (C4MIP; C. D. Jones et al., 2016), atmospheric chemistry and aerosols (AerChemMIP; Collins et al., 2017), land use (LUMIP; Lawrence et al., 2016), carbon dioxide removal (CDRMIP; Keller et al., 2018), and detection and attribution (DAMIP Gillett et al., 2016) among others.

While future scenarios for mitigation and adaptation anticipate major contributions from land, including bioenergy and afforestation (IPCC, 2019), ESMs' capabilities to simulate simultaneous changes in climate and vegetation, including terrestrial carbon stocks and fluxes, remain very limited. At the same time, changes in vegetation also feed back to the regional surface climate, hydrological cycle, exchanges of energy, biogeochemical tracers, and short-lived climate forcers, for example, dust (Jia et al., 2019). Here we demonstrate that comprehensive ESMs, such as ESM4.1, are able to maintain quality simulations of surface climate and capture vegetation structure and distribution on centennial scales over the historical period.

The three main goals of this paper are to (a) provide an overview of the terrestrial component LM4.1 of the GFDL-ESM4.1 model, including major advances in representing ecosystem processes as compared to the previous GFDL terrestrial component LM3.0 used in the GFDL CMIP5-class models (Dunne et al., 2012, 2013); (b) evaluate characteristics of land biosphere and surface climate in the historical greenhouse gas (GHG) concentration-driven experiments with ESM4.1 for 1850–2014, including historical trends and the current state of hydrological and carbon cycle metrics, and (c) and compare the ESM4.1/LM4.1 simulation with the CMIP5-class simulations of the ESM2G/LM3.0 model (Dunne et al., 2012, 2013) to document areas of improvement or degradation in the new model. Since LM4.1 includes a new treatment of vegetation dynamics, canopy structure, and plant hydraulics, we include detailed equations for the multi-layer energy balance, plant allometry and hydraulics, carbon allocation, stomatal conductance, and water limitation on photosynthesis (Appendices). Representations of other processes are briefly summarized; detailed equations are provided in previous publications describing their development. It is important to point out that LM4.1 was not tuned or calibrated in the historical ESM4.1 simulations during the ESM4.1 development following the philosophy that historical climate change and thus changes in land physical, biogeochemical, and ecological characteristics should emerge from the model's underlying parameterizations in response to historical anthropogenic forcing, including changes in land use and atmospheric CO_2 concentration, rather than be calibrated. The paper concludes with a brief discussion of model biases and limitations and ongoing developments to address them.

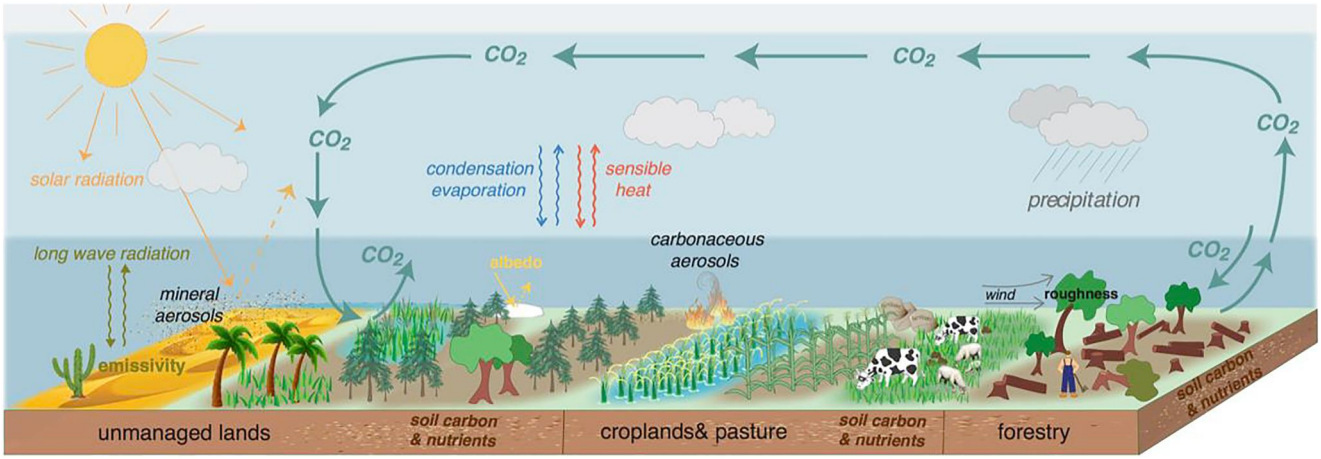

Figure 1. Schematic of land surface processes (e.g., dynamic vegetation competition, land use) and land-atmosphere interactions including radiative, hydrological, CO_2, and dust fluxes in Geophysical Fluid Dynamics Laboratory LM4.1 land model.

2. New Features in the LM4.1 Model

The LM4.1 model (Figure 1) is the fourth-generation successor to the GFDL ESM terrestrial component LM3.0 used in the CMIP5 GFDL ESM2M and ESM2G (Dunne et al., 2012, 2013) and CM3 (Donner et al., 2011) models, and is the land component of ESM4.1 (Adcroft et al., 2019; Dunne et al., 2020a; Horowitz et al., 2020). The main improvements in LM4.1 focus on the representation of ecological processes such as plant community dynamics, biophysical processes such as plant hydraulics and stomatal controls on evaporation, natural and anthropogenic disturbances such as wildfire and deforestation and agricultural biomass appropriation, and land-atmospheric interactions such as dust emission. Previously, LM3.0 predicted the distribution of vegetation as a function of climate, atmospheric CO_2 concentration, and anthropogenic land use. Vegetation was represented by a single-layer canopy of homogeneous vegetation (i.e., no tree or grass mixtures) which accounted for the attenuation of the incident light through the canopy in computing plant photosynthesis and average stomatal conductance (Leuning, 1995). Fire disturbance was applied annually, with carbon smoke emissions released into the atmosphere throughout the subsequent year. Soil carbon was represented by one box with an average over multiple soil layer temperatures and soil moisture. Major updates in LM4.1 are summarized in Table 1.

LM4.1 is a fully consistent, energy- and matter-conserving modeling system simulating the evolving land radiation, heat, hydrological, and carbon cycles as well as emissions of dust on time scales from minutes to multiple centuries. In CMIP6 ESM4.1 simulations, all land components (e.g., plants, soil, and snow) "participate" in moisture and energy exchanges with the atmosphere and ocean (via runoff). Each plant cohort in a multi-layer canopy has its own energy balance (e.g., sensible and latent heat fluxes and net absorbed radiation) and as a result, its own leaf temperature, intercepted water or snow storage, and stomatal conductance which are all updated on the atmospheric physics time step (i.e., 30 min). In turn, the biomass pools of cohorts' leaves, roots, sapwood, and wood (thus, cohorts' heights) are updated daily due to growth and/or mortality and affect land surface characteristics such as albedo, surface roughness, and leaf area index (LAI). In addition, land surface characteristics are affected by phenology, fire disturbance (daily), and land use land cover change (LULCC) processes (e.g., harvesting for pastures daily and croplands annually; logging and agricultural abandonment occur annually).

LM4.1 changes in vertical vegetation structure and plant competition are governed by the novel theoretical framework Perfect Plasticity Approximation (PPA) (Martínez Cano et al., 2020; Strigul et al., 2008; Weng et al., 2015). In addition, LM4.1 includes a new treatment of plant hydraulics and leaf stomatal conductance (Wolf et al., 2016), a new daily fire model FINAL v2 (Rabin et al., 2015, 2018; Ward et al., 2018) with distinct parameterizations for croplands, pastures, and unmanaged lands (i.e., secondary and primary) and a new prognostic dust emission model (Evans et al., 2016, 2019). The belowground carbon model is based on the CORPSE soil carbon model with an explicit treatment of microbes, which was previously coupled to the LM3.0 model (Sulman et al., 2014, 2019). CORPSE represents the vertical distribution of soil carbon following the discretization of the

Table 1
Major Changes in Land Model Structure and Parametrization

Feature	LM3.0	LM4.1
Canopy layers and radiation exchange	One with a two-stream radiation exchange	Multiple prognostic layers with a separate radiation exchange for each layer
Source of land cover heterogeneity (i.e., new sub-grid tiles)	Land use, glacier, lake	Land use, glacier, lake/river, fire, background mortality in the canopy layer
Number of vegetation cohorts per tile	One	Multiple cohorts per layer, of different ages and vegetation types with cohort-specific energy balance and intercepted water/snow
Plant allometry and carbon allocation	Carbon gain is allocated daily to leaves, fine roots, and sapwood following an empirical allocation scheme (Shevliakova et al., 2009)	Carbon gain is allocated daily to leaves, fine roots, sapwood, seeds, and non-structural carbon pools following the tree and grass allometric relationship (Martínez Cano et al., 2020; Weng et al., 2015)
Plant hydraulics	Fine roots resistance	Fine roots, xylem, and leaf resistances (Wolf et al., 2016)
Stomatal conductance	Leuning (1995) parameterization; Saturated specific humidity inside the leaf	Wolf et al. (2016) parameterization; Prognostic specific humidity inside the leaf does not require saturation
Soil carbon vertical structure	One box, separate for each sub-grid tile (Shevliakova et al., 2009)	Layers consistent with hydrological layers, a column per sub-grid tile (Sulman et al., 2014)
Soil BGC	Simplified Century first order decay (Shevliakova et al., 2009)	Explicit microbes-soil organic matter interactions, based on CORPSE (Sulman et al., 2014)
	Fine and coarse litter	Fine and coarse litter and root exudates
Fire	Annual, empirical, prescribed return rate by vegetation type	FINAL v2 model, prognostic daily, with multi-day fires in the boreal zone; prescribed regional cropland/pastureland fires; prognostic wildfires (Rabin et al., 2018; Ward et al., 2018)
Dust emissions	None	Prognostic (Evans et al., 2016, 2019)
Land use	Gross transitions between primary, secondary, cropland, and pastureland from Hurtt et al. (2020) CMIP5 scenarios; pasture and cropland harvesting annually at the end of the year	Gross transitions between primary, secondary, cropland, pastureland, and rangelands from Hurtt et al. (2020) CMIP6 scenarios; pasture grazing daily, crop harvesting annually according to a prescribed schedule

soil column for soil hydrology and thermodynamics (Milly et al., 2014). Among the unique features of LM4.1 is a heat tracer in land hydrology to track water temperature from the top of the soil/snow through the soil column and river routing system (Milly et al., 2014).

While many advancements in representing coupled carbon and nitrogen cycles for plant-soil-riverine systems (e.g., plant-microbial C-N interactions (Sulman et al., 2014, 2019), riverine C-N dynamics (Lee et al., 2019)) were implemented in the previous version of the GFDL terrestrial component LM3.0 with simplified vegetation dynamics (Shevliakova et al., 2009), the coupled C-N dynamics was not included into ESM4.1 because of GFDL's limited experience with representing C-N plant processes within the PPA framework in an ESM in the CMIP6 multi-century simulations and a desire to treat the suite of advances sequentially.

2.1. Second-Generation Vegetation Demography

The LM4.1 integrates PPA (Strigul et al., 2008; Martínez Cano et al., 2020; Weng et al., 2015, Figure 2) with multi-layer canopy energy, moisture and CO_2 exchanges, and soil physics, hydrology, and carbon cycling. LM4.1 enables the representation of ecosystem demography and currently is referred to as a second-generation DGVM (Fisher et al., 2017). Ecosystem demography models (e.g., the ED-derived models such as ED (Moorcroft et al., 2001), ED2 (Medvigy et al., 2009), ED2.v2 (Longo et al., 2019), CLM-ED (Fisher et al., 2017), FATES (Koven et al., 2019)) capture age-height structure in forest canopies, competition for light, changes in plants density, gap formation due to natural mortality and fire—the critical processes for predicting future carbon storage in forests and their distribution. These processes determine the rates of carbon accumulation in changing environments, tree mortality, and competition among different types of vegetation. In turn, these processes affect

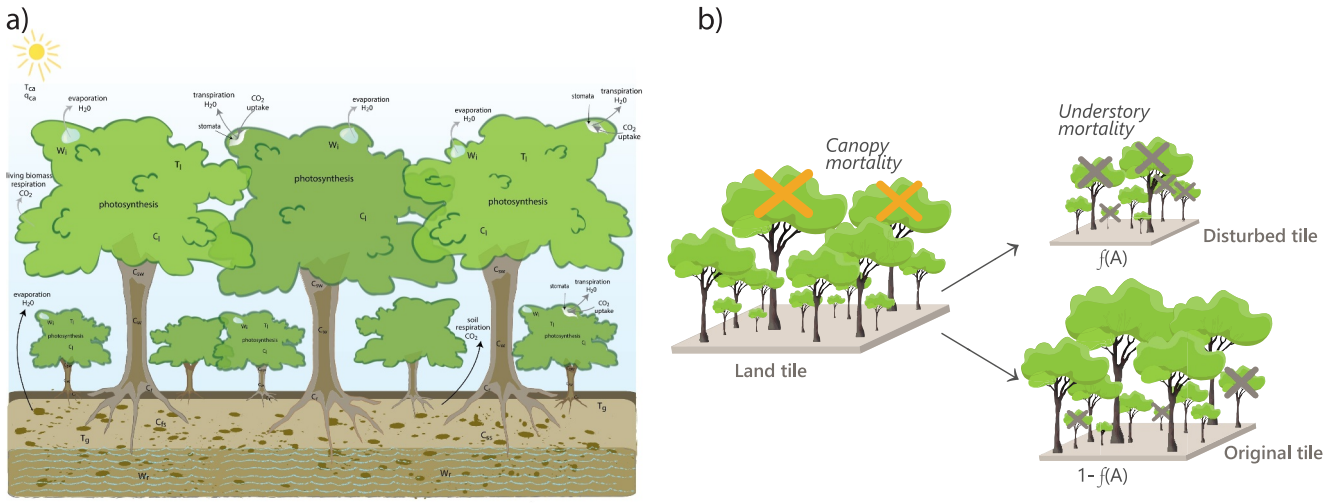

Figure 2. (a) Cohort structure within a single natural or secondary tile. Each tile can have an arbitrary number of layers determined by Perfect Plasticity Approximation dynamics and a mixture of vegetation types. Each cohort has a prognostic physical and biogeochemical state (a) and it is affected by tile dynamics due to natural disturbance due to background mortality or fire (b).

many land surface characteristics such as albedo and surface roughness which affect the atmosphere (i.e., biophysical feedback) or land CO_2 fluxes (i.e., biogeochemical feedback).

The cohorts interact and compete for light and water, simulating the processes responsible for the formation of ecosystems. According to the PPA, the canopies of each cohort fill the available space in a tile based on their height and crown areas (Strigul et al., 2008), so the tallest cohorts form the upper canopy layer, then the next tallest cohorts fill up the space in the second layer, and so on. As the vegetation evolves in time, the cohorts are rearranged so their crowns collectively fill the entire tile area in each of the canopy layers (Figure 2a). The PPA approximation predicts the height at which a new layer is formed (Martínez Cano et al., 2020; Strigul et al., 2008; Weng et al., 2015), so the number of vegetation layers in each LM4.1 tile is an emergent dynamic property. In addition, similarly to ED-based models, natural (e.g., large fires, upper canopy tree mortality) and anthropogenic (e.g., logging) disturbances generate new tiles (Figure 2b).

2.2. Sub-Grid Land Heterogeneity

LM4.1 represents sub-grid scale heterogeneity of the land surface using a mosaic approach that splits each land grid cell into multiple tiles. Each tile represents a fraction of the grid cell with unique physical and biological properties. For example, different tiles within the same grid cell may represent natural (i.e., primary) vegetation, cropland, pasture, rangeland, and secondary vegetation at different stages of regrowth (up to 16 secondary tiles capturing the age of the vegetation after logging or abandonment). Open water surfaces (lakes and rivers) and glaciers are also represented as separate tiles, similar to LM3.0 (Milly et al., 2014), and have separate energy exchanges with the atmosphere. The number of tiles in every model grid cell is dynamic, driven by human disturbances (changes in land use), fire (assumed to be wildfire on primary and secondary tiles), or gap dynamics resulting from forest canopy layer tree mortality. For computational efficiency, LM4.1 merges tiles with similar physical and biological properties. Atmospheric exchange of energy, water, and tracers, including stability, are calculated separately for each tile, enabling the model to consider differences among tiles in land-atmosphere interactions.

Within each tile, vegetation is represented by a dynamic set of cohorts arranged in different canopy layers according to PPA (Martínez Cano et al., 2020; Weng et al., 2015). Each cohort represents a collection of plants with identical properties including vegetation type, size, rooting depth, age, etc. The set of cohorts represents the vegetation size/age structure and distribution of its properties within a tile. In ESM4.1 simulations, the model solves the equations of land surface energy, water, and CO_2 exchanges with atmospheres using an implicit time-stepping scheme with a time step of 30 min. The equations of land surface energy and water mass balance are described in Appendix A.

2.3. Soil Carbon Dynamics

The soil carbon cycling in LM4.1 follows the approach of the Carbon, Organisms, Rhizosphere, and Protection in the Soil Environment (CORPSE) model, described by Sulman et al. (2014). This model explicitly simulates a dynamic microbial biomass pool to control soil organic carbon transformation and decomposition. The original CORPSE implementation and parameter set did not allow for a multi-century stabilization of carbon pools in the preindustrial climate control simulations, and as a result violated the CMIP6 recommendation that the long-term average land carbon fluxes in ESM control experiments should be stable in time and not exceed 0.1 PgC yr^{-1} (Eyring et al., 2016). To meet this requirement, the accumulation of carbon in protected pools was prohibited, and an upper limit of 500 years was imposed on the time scale of carbon decomposition. These assumptions imply that the accumulation of very slowly decomposing carbon in high latitudes may not reach as high carbon content values as estimated from available observations. On the other hand, given the current state of knowledge, such very slow processes would be very hard to constrain observationally, and small changes in model parameters could potentially result in very different equilibrium states of carbon accumulation even if they could be reached in multi-millennial (or longer) simulations.

2.4. Fire

In ESM2G/LM3.0 a simple fire parameterization was applied annually to capture the effects of fire disturbance on vegetation carbon, with a prescribed fire return interval specified for each vegetation type. The mortality rate due to fire was further modulated by an annually accumulated empirical factor reflecting above-ground biomass (AGB) as a proxy for fuel availability (Shevliakova et al., 2009). The annual loss of vegetation carbon due to fire mortality was emitted to the atmosphere throughout the subsequent year.

The fire component of ESM4.1/LM4.1 advances previous fire treatment and largely follows the FINAL v2 global fire model in LM3.0 (Rabin et al., 2015, 2018; Ward et al., 2018), with additional generalization to account for multiple cohorts in each of the vegetation tiles in LM4.1. For example, the averaging depth used to estimate soil moisture input to the fire factor was calculated as a weighted average of all cohort e-folding root depths scales, with each cohort's fine root biomass used as the weight. Likewise, the rate of fire spread is calculated as a weighted average of vegetation in individual cohorts, with a total crown area of each type used as an averaging weight. This weighting is required to ensure that the factor is scaled properly in the locations with mixed grass/tree coverage. In the ESM4.1 historical experiment, changes in population density (B. Jones & O'Neill, 2016) affect fire ignition and fire suppression rates.

Fire in LM4.1 is applied daily at each of the sub-grid tiles; when a fire occurs and if an area burned exceeds a specified threshold, it creates a new sub-grid tile (if several of the original vegetation tiles are affected, the model will create several fire tiles) where the vegetation is affected by fire, while the vegetation in the rest of the land surface area is not disturbed. This allows proper accounting for fire scars and their recovery after disturbance. As an example, the probability of fire re-occurring on tiles recently disturbed by fire is reduced under the same climate conditions because of the reduction in fuel consumed by the previous fire. In the burning fraction of the landscape, fire affects different cohorts depending on their specific fire-related parameters, including combustion completeness of various types of tissues, and fire mortality. Agricultural fires in LM4.1 are treated differently from fires in the regions on unmanaged vegetation, as described by Rabin et al. (2018). Note that LM4.1 treats fires on rangelands the same as on natural and secondary vegetation, while fires on pastures are considered human-controlled.

2.5. Dust Emissions

A novel feature in the dust emission parameterization in ESM4.1/LM4.1 is its dependency on a combination of meteorological, geomorphological, vegetation, and land use conditions: soil moisture, temperature, bareness, snow cover, land use type, and surface wind speed are calculated dynamically within each tile of LM4.1. The emission flux is then passed to the atmospheric model AM4.1 where dust particles are transported and removed by dry and wet deposition. This approach allows simulation of the observed low-frequency (inter-annual and beyond) variability of dust concentrations by modulating dust emission with climate change through soil moisture and vegetation responses (Evans et al., 2016). In addition, this scheme allows to estimate the contribution of anthropogenic activities to dust emission associated with land use changes (Evans et al., 2019). The model uses the global erodibility map of Ginoux et al. (2001), but the source areas (bare surfaces) are calculated as a

decreasing exponential function of the sum of LAI and 10 times the Stem Area Index (SAI), with emissions set to zero if LAI or SAI is greater than 0.1 and 0.01, respectively.

On land use tiles, bare surface is assumed to occupy 3.25% of the tile area for cropland and pasture. Dust emission occurs when the surface wind reaches the threshold speed to initiate sandblasting, a necessary process to eject dust particles from the soil. Although the threshold of surface wind speed varies considerably between sources and even within a source (Pu et al., 2020), we use fixed values of 1 m s^{-1} for primary, secondary, and rangeland; 6 m s^{-1} for pasture; and 8 m s^{-1} for cropland. Dust emissions are deactivated if ice content in the top 15 cm of the soil is greater than 5% or if the snow water equivalent on the surface is greater than 10 g m^{-2}. In the simulations analyzed here, the dependency on soil moisture was not activated. The global dimensional constant of dust emission, C in Equation 2 of Ginoux et al. (2001) is equal to 1.5 μgs^2 m^{-5}. This constant is derived from fitting surface dust concentration measured over 20 island sites worldwide (Ginoux et al., 2001; Prospero, 1996).

2.6. Land Use

Similarly to LM3.0, LM4.1 represents land use via wood harvesting and deforestation during agricultural conversion (Shevliakova et al., 2009), following the scenarios of gross transitions (Hurtt et al., 2020) among undisturbed lands (i.e., "primary" or "potential"), croplands, pastures, and lands either previously harvested or used in agriculture (i.e., "secondary," up to 10 age classes). The model represents the harvesting of primary and secondary forests for wood via removal of carbon on areas of land use transitions from primary to secondary, or from secondary to secondary, respectively. The annual rates of transitions are imposed in terms of gross areas of transitions, but the amount of harvested carbon per unit area involved in the transitions is calculated based on the existing state of the vegetation on disturbed tiles. Regardless of the plant size, vegetation is removed, and the plant carbon in the harvested pools is gradually released into the atmosphere with time scales of one year to one hundred years.

Pastures in LM4.1 are grazed daily, with 5% of leaves being consumed every day toward an imposed LAI lower limit of 1 m^2 m^{-2}. LM4.1 introduces a new type of land use tile, rangeland. Note that a transition to rangeland does not involve any disturbance to or removal of the vegetation in the converted fraction of a grid cell; only grazing after the transition distinguishes the carbon dynamics on such tiles from their previous land use states. Grazing of rangelands is treated the same as pasture grazing, except that the vegetation taller than 3 m is not grazed, representing the limited ability of grazers to reach canopies of taller trees. In both cases, grazed biomass is accumulated in the harvesting pool, which is gradually released into the atmosphere over a time scale of 1 year. The model also includes crops' growing seasonal cycles (i.e., prescribed planting and harvesting dates). Cropland planting and harvesting occur at prescribed times during the year, using an observation-based data set of planting and harvesting dates (Paulot et al., 2018; Portmann et al., 2010). Note that this data set does not support double cropping, which may result in some biases in patterns of LAI and crop biomass evolution, especially in subtropical and tropical regions where this practice may be widespread (Arvor et al., 2013; Morillas et al., 2019). At the crop planting date, the croplands are seeded with small initial biomass (0.1 kgC m^{-2}) and start growing until they are harvested. Similar to grazing, harvested biomass is accumulated in the intermediate carbon pool, which is gradually released into the atmosphere over 1 year. The model represents crops as C3 or C4 grasses; the type of the crop is determined by simple biogeographical rules (Shevliakova et al., 2009) based on annual mean temperature and precipitation.

2.7. Soil/Snow Hydrology

The LM4.1 soil water dynamics and soil energy balance formulations follow Milly et al. (2014) with changes implemented in the development of AM4.0 (Zhao et al., 2018) and CM4.0 (Held et al., 2019). The current configuration uses the distribution of soil properties from Shangguan et al. (2014).

Similar to the CMIP5-class GFDL land models LM3.0 and LM3.1 as well as the CMIP6-class LM4.0 model used in CM4 (Held et al., 2019) and SPEAR (Delworth et al., 2020) models, LM4.1 assumes a steady-state groundwater (i.e., below the water table) flow. The horizontal groundwater flow at any point is a balance between a recharge uphill from that point and the horizontal hydraulic gradient (Milly et al., 2014, Section 2d). The rate of subsurface water discharge to surface water is the vertical integral of the lateral flow divergence at each subgrid tile, conceptualized as having a characteristic hillslope structure described in detail in Milly et al. (2014).

A grid-scale river and lake network model simulates the transport of water runoff to the oceans. For each river reach, LM4.1 simulates depth-averaged liquid mass, ice mass, and sensible heat content. The hydraulic geometry of Leopold and Maddock (1953) governs river flow. LM4.1 computes prognostic liquid water content, ice content, and temperature for multi-layer soil (10 m depth), lake, and snowpack. The soil is treated as a dual-domain (Beven & Germann, 1982), saturated-unsaturated, soil-bedrock continuum with water vertical flow represented by the Richards equation (Hillel, 1980). LM4.1, similarly to LM3.0, represents parameterized effects of idealized macropores and sub-grid infiltration and discharge to rivers (Milly et al., 2014). Depending on the lake size, lakes are represented by one or more vertical columns, with density-driven stratification and overturning. To ameliorate the occurrence of super polynyas in the Southern subpolar ocean in ESM4.1, the near-infrared albedo of snow on Greenland and Antarctica glaciers was increased from ∼0.73 in LM3.0 (Milly et al., 2014) to ∼0.82 in LM4.1 following the experience with the two other GFDL coupled physical models SPEAR (Delworth et al., 2020) and CM4.0 (Held et al., 2019).

3. Experimental Setup

This paper presents an evaluation of ESM4.1/LM4.1 (Dunne et al., 2020a) land hydrological, biogeochemical, and ecological characteristics from the historical simulations contributed to CMIP6 DECK (Eyring et al., 2016) and comparisons with ESM2G/LM3.0 (Dunne et al., 2012) land characteristics from the historical simulations contributed to CMIP5 (Taylor et al., 2012). The historical experiments are designed to cover the Earth's response to anthropogenically driven changes in concentrations of greenhouse gases and short-lived climate forcers as well as land use land cover change (for details see https://pcmdi.llnl.gov/mips/cmip5/forcing.html and https://pcmdi.llnl.gov/CMIP6/Guide/modelers.html#2-experiment-design).

ESM2G includes AM2.0 atmospheric component and Generalized Ocean Layer Dynamics ocean component. ESM2G has a resolution of ∼2° for the atmosphere and land, ∼1° for the ocean and sea ice, 24 vertical layers in the atmosphere, 50 vertical layers in the ocean, and 20 layers in the soil.

ESM4.1 consists of GFDL's AM4.1 atmospheric model with full chemistry and 49 hybrid sigma-pressure layers at 1° resolution (Horowitz et al., 2020; Zhao et al., 2018), Modular Ocean Model version 6 at 0.5° resolution (MOM6; Adcroft et al., 2019), Sea Ice Simulator version 2 (SIS2; Adcroft et al., 2019), ocean biogeochemical model COBALT (Stock et al., 2020), and the terrestrial model LM4.1 described here. Land for the 1850 pre-industrial DECK experiment (piControl) was initialized with potential vegetation (i.e., no land use), followed by a 1-year bridge run applying land use transitions to the 1850 state (area fractions) of crops and pastures (no logging or shifting cultivation or abandonment and thus no secondary forest) for an estimate of mid-nineteenth century land use, with fractions of crops and pasture kept constant throughout the pre-industrial simulation (i.e., no land use *change*). To initialize the 1850 land state in the historical ESM4.1 simulation, we first conducted a separate bridge run before 1850 to represent the transient effects of the land use history on the age and biomass of forests recovering from previous logging activities, agricultural land abandonment, and associated evolving size of soil carbon pools. This bridge experiment was run for 100 years with all pre-industrial control forcings but 1750–1849 land use change transitions to allow the secondary forests to spin up to a realistic state of regrowth (see Dunne et al. (2020a, 2020b) for details). The historical 1850–2014 simulation included the time-evolving greenhouse gas (GHG) and ozone-depleting substance concentrations, aerosol and ozone precursor emissions and solar irradiance consistent with CMIP6 specifications (Dunne et al., 2020a), and the land use gross transitions reconstruction scenario (Hurtt et al., 2020, https://luh.umd.edu/data.shtml). A three-member ensemble of historical simulations was performed using ESM4.1, branching from different points in the pre-industrial control run. The analysis presented here is based on one ensemble member except where noted.

4. Surface Climate and Water Budgets

On the global scale, the surface climate is the main determinant of the spatial distribution of vegetation and related land characteristics, including those that control land carbon, energy, and water cycles. Human influences are more apparent at regional and local scales and in long-term trends. In this section, we evaluate elements of land-surface climate (temperature, precipitation, and radiation) and water budgets (evapotranspiration, runoff, soil moisture, and permafrost). Analysis of the spatial distribution and temporal trends of climate over the twentieth century is critical for interpreting the distribution and evolution of land hydrological and biogeochemical states.

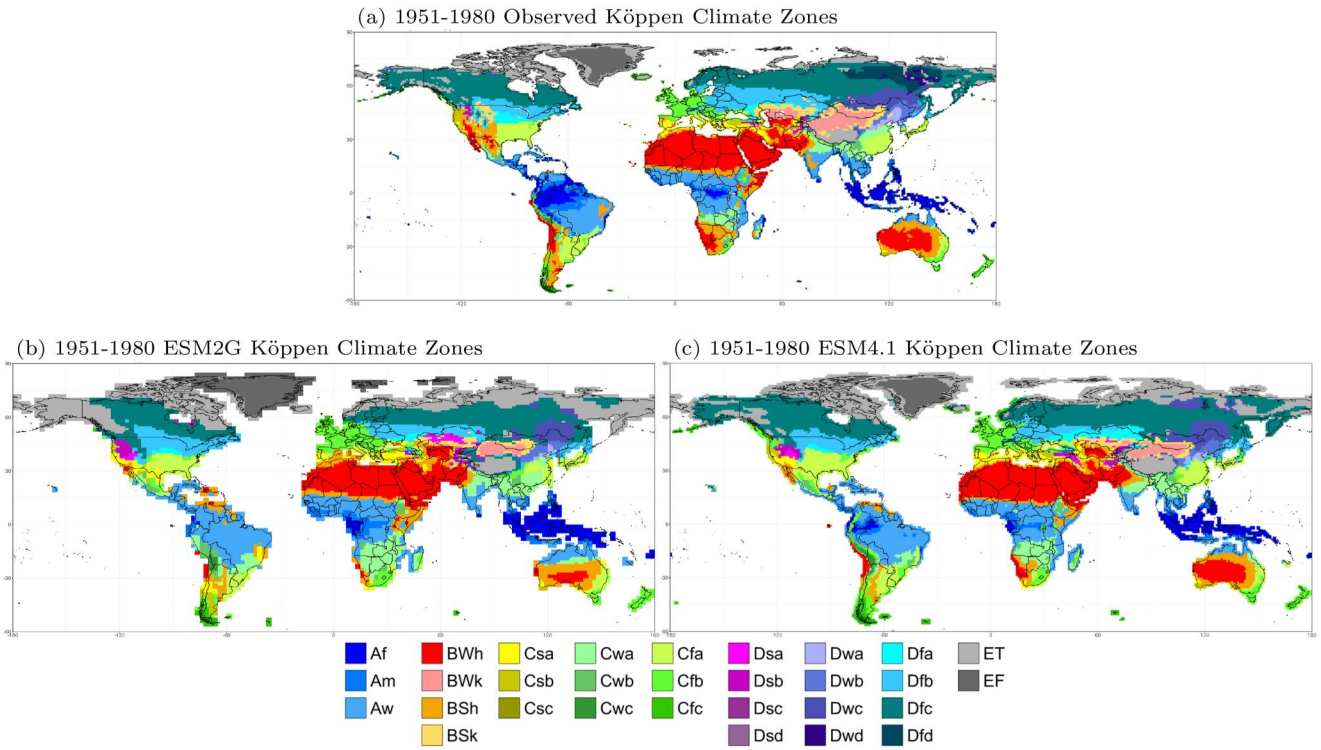

Figure 3. Köppen climate zone distribution based on observed, ESM2G, and ESM4.1 climates. The legend description is provided in Appendix F. Köppen climate zones are calculated based on 1951–1980 climatologies for both model data and empirical data. Empirical climatologies are generated using $1° \times 1°$ monthly Berkeley Earth land surface temperature data, and $1° \times 1°$ monthly GPCC precipitation data. We generate climatologies of temperature and precipitation for each grid point. We follow the Köppen-Geiger scheme, using -3°C as our coldest-month threshold, rather than 0°C (as in Kottek et al. (2006)). The Köppen climate maps provided borrow the color scheme used in Peel et al. (2007) and Beck et al. (2018).

Identification of model transient climate biases is therefore an important aspect of interpreting land ecological and biogeochemical responses in the ESM framework.

The land is but one component of the climate system. The realism of modeled land states in any earth-system model reflects the realism of all that earth-system model's interacting component models. Conversely, biases of land states arise from deficiencies in all component models. Similar statements can be made about the improvement or deterioration of a simulation from one model generation to the next. As much as possible within the framework of a coupled model, here we distinguish between biases that are attributable to shortcomings of the land model versus those that are attributable to the climate (i.e., coupled atmosphere and ocean) that drives the land model. While we recognize that climate biases themselves may be influenced to some extent by the land model, quantification of such feedback is outside the scope of the present analysis.

4.1. Köppen Climate Zones

The comparison of Köppen climate zones in Figure 3 indicates that ESM4.1 generally simulates a realistic major world climate distribution while having difficulty capturing the extent and location of tropical rainforest climate (Af), particularly in Amazonia, sub-arctic (Dfc), and severe-winter subarctic (Dfd) zones in Eurasia, and several climate zones in the Western US and Southern Africa. Compared to ESM2G, there are some improvements in Arctic boreal zones and some arid regions. However, there are still biases in moist tropical climates, in particular in Amazon region, that may contribute to the biases in vegetation geographical distribution and carbon accumulation.

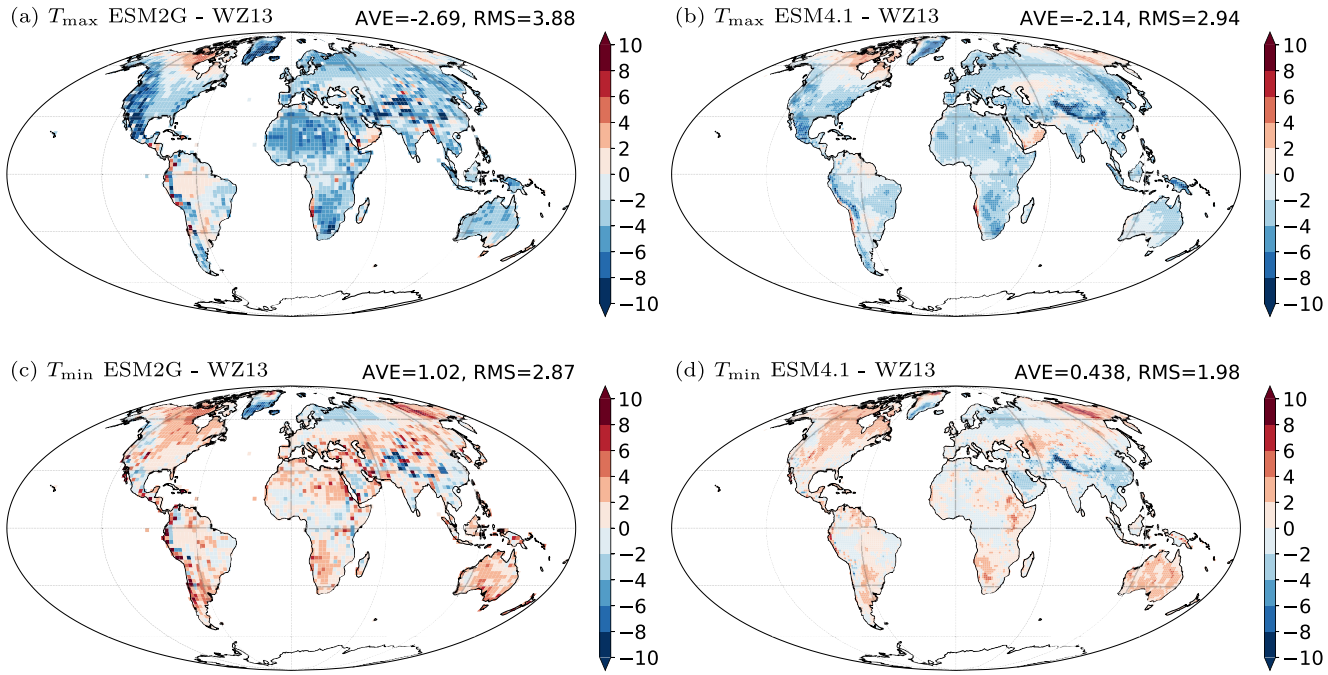

Figure 4. Annual mean difference in near-surface air temperature between the last 25 years of the historical simulations and the observation-based data product of A. Wang and Zeng (2013) (1985–2009 for comparison with ESM4.1 and 1981–2005 for comparison with ESM2G). WZ13 adjusts reanalysis data sets to better match the diurnal cycle of surface air temperature observations in the Climate Research Unit Time Series version 3.10 (CRU TS3.10) for the years 1948–2009. The resultant downscaled and bias-corrected final products are hourly, 0.5° grid-cell products with the same monthly minimum (T_{min}) and maximum (T_{max}) as the CRU data. Here we use the ECMWF Interim Reanalysis (ERA-Interim) version of the data product. The WZ13 data are first converted from hourly to monthly mean diurnal cycles to match the temporal frequency of the model output and are then converted to the ESM4.1 grid or the ESM2G grid.

4.2. Mean State

4.2.1. Near-Surface Air Temperature

Here we provide a comparison between the monthly mean diurnal cycle of 2 m air temperature (T2M) over land with the observation-based land surface air temperature (LSAT) product (1985–2009 for comparison with ESM4.1 and 1981–2005 for comparison with ESM2G) of A. Wang and Zeng (2013, hereafter WZ13). The patterns of differences between the models' maximum daily temperatures (T_{max}) and the WZ13 data are similar with slightly smaller biases and root mean square errors in ESM4.1. T_{max} is, on average, cooler than the observational estimates in both models, by 2.7°C in ESM2G versus 2.1°C in ESM4.1 (Figures 4a and 4b). The root mean square error is also smaller in ESM4.1 (2.9°C compared to 3.9°C). Minimum daily temperatures (T_{min}) simulated by both models are closer to the WZ13 data than T_{max}. T_{min} in ESM2G is, on average, 1.0°C warmer than the observations, while ESM4.1 is 0.4°C warmer (Figures 4c and 4d). ESM4.1 also has a smaller root mean square difference of 2.0°C compared to 2.9°C in ESM2G. In both models, most regions have a larger cold bias in T_{max} than warm bias in T_{min}, leading to a cold bias in the mean surface air temperature.

To investigate the seasonal dependence of any biases in the diurnal cycle of temperature, monthly mean diurnal cycles are calculated for various latitudinal bands (Figure 5). Though both models have smaller diurnal temperature ranges than the WZ13 data, in each latitudinal band the monthly mean diurnal cycles of ESM4.1 are closer to the observations than those of ESM2G, with global root mean square errors over land reduced from 1.51°C for ESM2G to 1.19°C for ESM4.1. The mean diurnal cycle differences show that nighttime values from both models are, in general, in much closer agreement with the reanalysis data than mid-day values.

4.2.2. Precipitation

The global distribution of precipitation over land in ESM4.1 ($r^2 = 0.87$) is an overall improvement upon that of ESM2G ($r^2 = 0.76$) (Figures 6a and 6b, Table 2). In both models, global precipitation over land has a positive bias of about 100 mm yr^{-1}, compared to a global mean of about 800 mm yr^{-1}. The global patterns of biases in the two

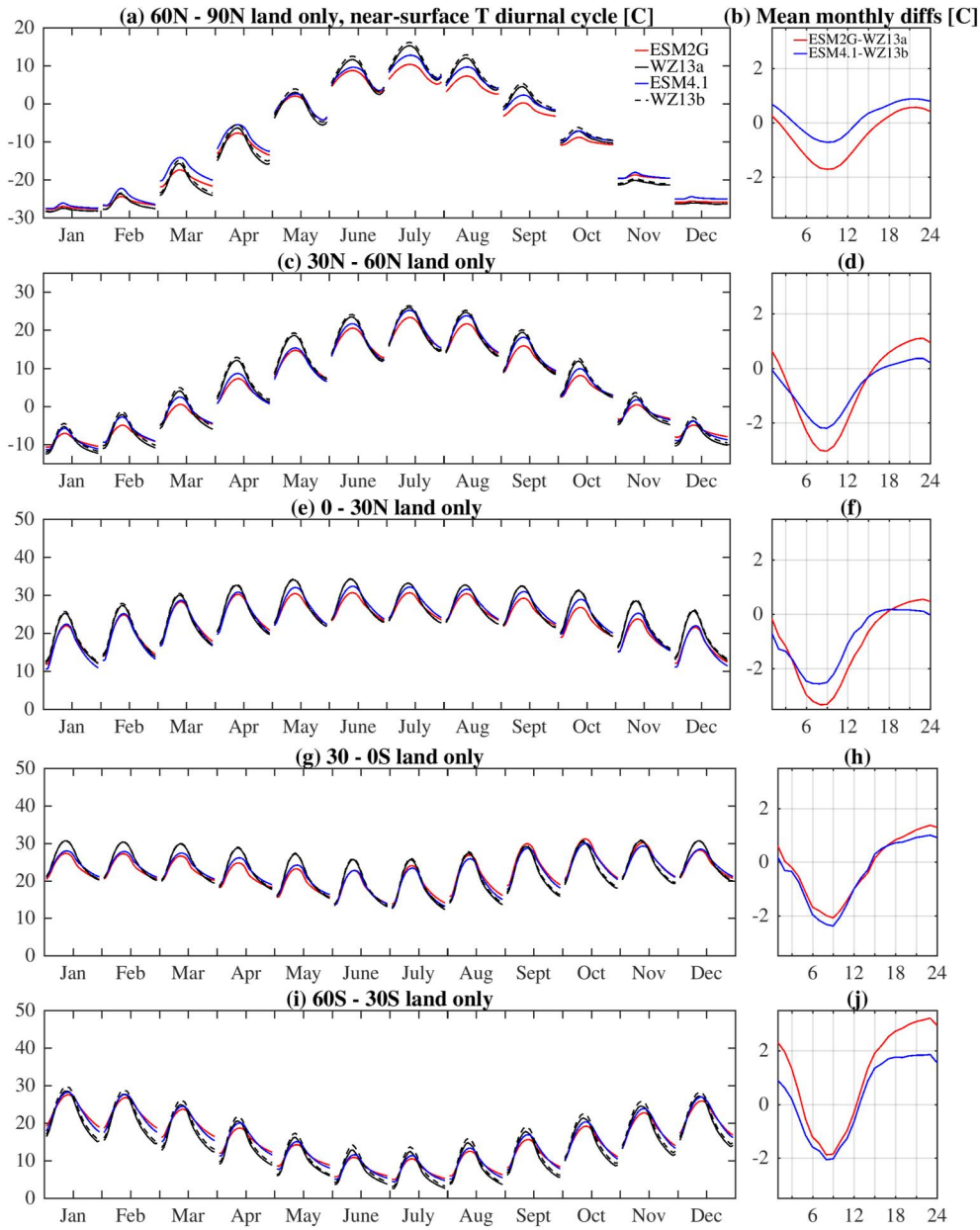

Figure 5. Left column: Monthly mean diurnal cycles averaged over land areas in zonal bands of 30° latitude each from ESM2G (red), ESM4.1 (blue), and the WZ13 observation-based data product of A. Wang and Zeng (2013) (WZ13a for years matching ESM2G, WZ13b for years matching ESM4.1; see Figure 4 caption for details). Right column: Corresponding annual mean differences in diurnal cycles, model—observations (ESM2G—WZ13a in red; ESM4.1—WZ13b in blue). The horizontal axis is the local time of day.

models are similar, but the bias magnitudes are generally smaller in ESM4.1. This improvement is especially marked in some arid to semi-arid regions of the world (northern and southern Africa, Australia, and southwestern North America), where biases in ESM2G exceed 100%. ESM2G's large negative biases in much of South America are also improved in ESM4.1. The most notable area of degradation of modeled precipitation amounts from ESM2G to ESM4.1 is the northwestern region of the South Asian monsoon.

4.2.3. Surface Radiation and Albedo

Surface net radiation is the main determinant of energy available for evapotranspiration. Therefore, together with precipitation, it determines the partitioning of precipitation into evapotranspiration and runoff. In both ESM2G

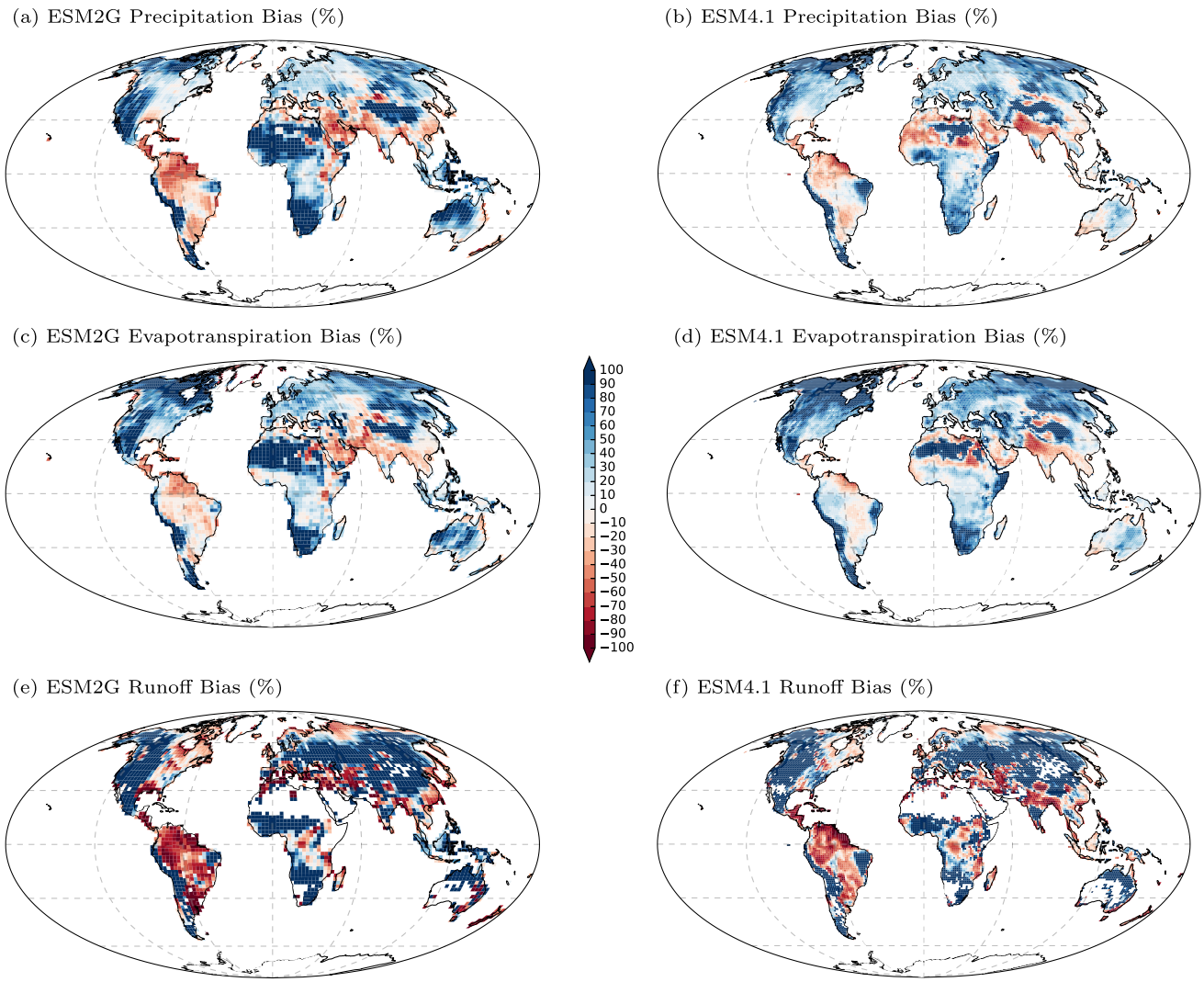

Figure 6. ESM2G and ESM4.1 annual mean water-budget flux biases, expressed as percent differences relative to observational estimates. (a and b) Precipitation, (c and d) evapotranspiration, and (e, f) runoff. Model fluxes are averaged over the period 1985–2014. Precipitation observations from the Global Precipitation Climatology Centre (Schneider et al., 2018) are for 1985–2014. The observation-based estimate of evapotranspiration (Zhang et al., 2016) is for the period 1981–2012. The observation-based estimate of runoff (Fekete et al., 2011) is for 1986–1995.

Table 2
Statistics of Model Surface Fluxes

	P, mm yr^{-1}		Rn/L, mm yr^{-1}		E, mm yr^{-1}		R, mm yr^{-1}	
	ESM2G	ESM4.1	ESM2G	ESM4.1	ESM2G	ESM4.1	ESM2G	ESM4.1
Observations	800	790	1,131	1,117	504	501	298	294
Model-Obs	106	108	−134	−113	88	116	18	−15
r^2	0.76	0.87	0.97	0.97	0.87	0.90	0.37	0.61

Note. P, Rn, E, and R are precipitation, net radiation, evapotranspiration, and runoff, respectively. L is latent heat of vaporization of water. Statistics are computed after regridding of observations to model grids, so the global observation values differ slightly between models.

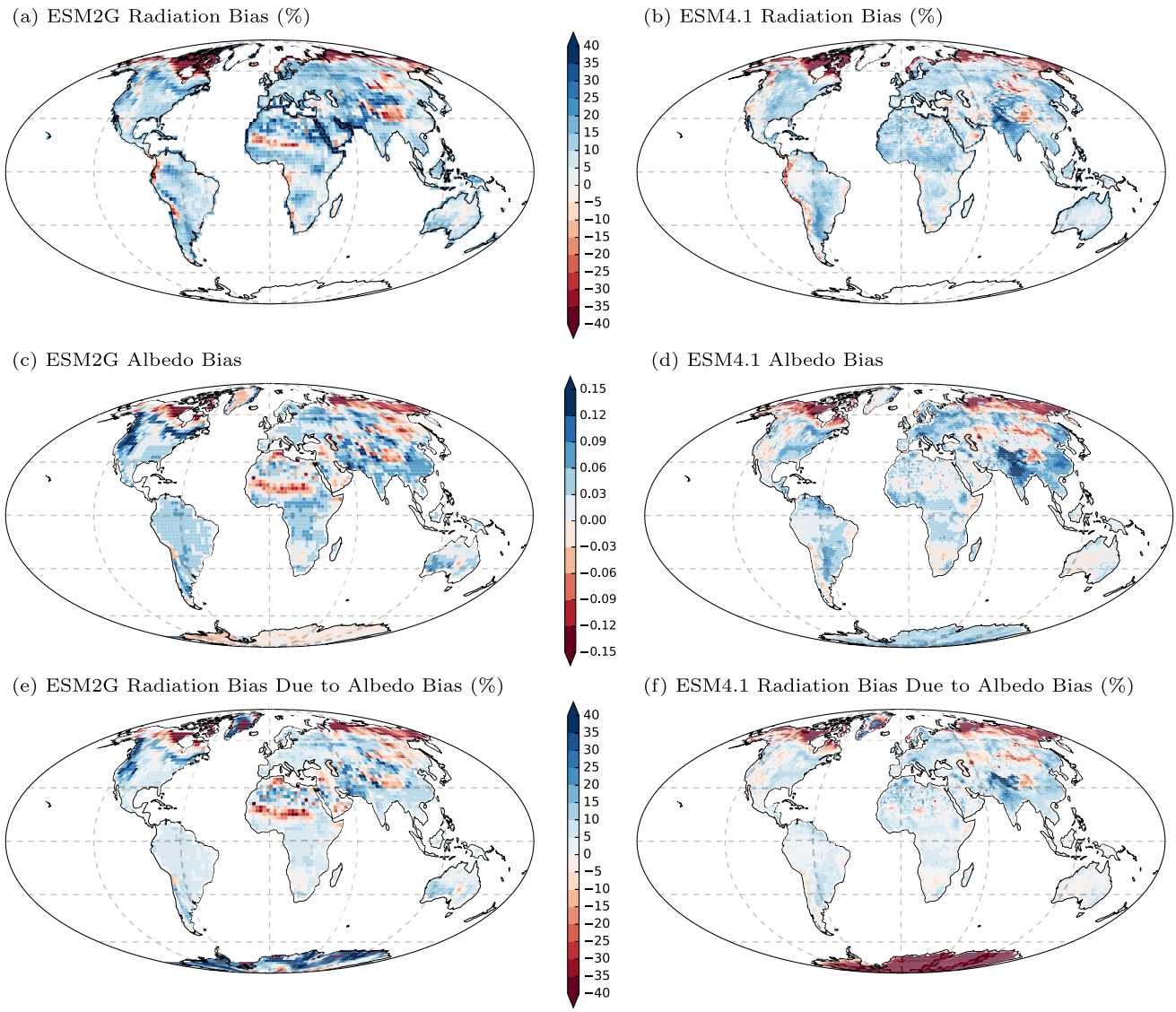

Figure 7. Surface net radiation and albedo. (a and b) Bias in radiation in ESM2G and ESM4.1, percent; (c and d) bias in effective surface albedo in ESM2G and ESM4.1; (e and f) bias in radiation directly attributable to bias in surface albedo in ESM2G and ESM4.1, percent. Model fluxes are averaged over the period 1985–2014. Radiation observations are from Clouds and the Earth's Radiant Energy System surface irradiance product (Kato et al., 2018) and are limited to the available period of record (March 2000 through March 2018). Effective surface albedo is calculated as annual upward shortwave radiation divided by annual downward shortwave radiation.

and ESM4.1, the spatial correlation of land net radiation with observations is high (0.97) (Table 2), but the global average land net radiation has a substantial positive bias in both ESM2G (18%) and ESM4.1 (16%). Accordingly, a uniformly positive bias is seen over the most land area (Figures 7a and 7b). Notable exceptions are in the high northern latitudes and the region of the Tibetan Plateau.

The pattern of biases in surface net radiation common to both models is associated with biases in effective annual surface albedo (i.e., the ratio of annual upwelling to annual downwelling shortwave radiation). In the models, albedo (Figures 7c and 7d) is close to observations in arid regions, where it is determined by soil albedo (which has been specified in both ESM2G/LM3.0 and ESM4.1/LM4.1 based on satellite observations, Milly et al. (2014)). In densely vegetated regions of the low and middle latitudes, modeled albedo is excessively high. In the high latitudes of North America and Asia, on the other hand, albedo has a strong negative bias. The albedo biases create biases in the absorption of shortwave radiation (Figures 7e and 7f), which contribute considerably to the overall bias in net radiation over most land areas. The albedo bias in high latitudes is related to the excessive

northward extension of the models' boreal forests relative to the real world, which will be discussed in the next section. Surface albedo is much reduced by a forest canopy, compared to what it would be in sparsely vegetated tundra.

To estimate the strength of the snow albedo feedback in the model, we follow the seasonal cycle method of Qu and Hall (2006) and Hall and Qu (2006). They define the strength of feedback as the difference in climatological land surface albedo between April and May, averaged over the 30°–90°N region using insolation as averaging weight, and divided by the April-May difference in surface air temperature averaged over the same region. The ESM4.1 value for the 1982–1999 period (same as in Qu & Hall, 2006) is $-0.81\%\ K^{-1}$, lower in magnitude than the observational estimate of -1.01 to $-1.13\%\ K^{-1}$ of Qu and Hall (2006). The lower value of the albedo feedback in ESM4.1 compared to the observational estimate is largely due to the northward extension of the boreal forest noted above, which reduces the sensitivity of land surface reflectance to snow cover and snow amount. The magnitude of ESM2G value of albedo feedback is $-0.87\%\ K^{-1}$ is also lower in magnitude than observational estimates, but higher than ESM4.1. Tree cover extent in ESM2G is also biased northward as illustrated in Figure 7, but its effect is compensated by a different formulation of vegetation snow overlap.

4.2.4. Evapotranspiration and Runoff

From a global perspective, ESM4.1 evapotranspiration (Figure 6d) and runoff (Figure 6f) are better correlated ($r^2 = 0.90$ and 0.61, respectively) with observations than are the fluxes in ESM2G ($r^2 = 0.87$ and 0.31) (Figures 6c and 6e). In both ESM2G and ESM4.1, global patterns of bias of both variables are similar to those for precipitation. In general, runoff biases are larger in percentage terms than the precipitation biases that drive them. This is a consequence of the fact that the fraction of precipitation resulting in runoff increases as land gets wetter because the atmospheric demand for evapotranspiration becomes increasingly satisfied.

Although the biases in evapotranspiration and runoff generally are positively correlated with those of precipitation, some departures from strict proportionality result from regional limitations on evapotranspiration. In humid areas, where evapotranspiration is limited more by energy than by water availability (e.g., the Amazon basin and the region of Africa bordering the Gulf of Guinea), precipitation biases are reflected more in the runoff than in evapotranspiration. In arid to semi-arid regions (e.g., much of Australia), the opposite is true.

In both models, negative runoff biases that cannot be explained by the precipitation biases are present in the Arctic and Tropics. In the Arctic, this discrepancy is explained by the excessive net radiation and resultant excessive evapotranspiration. In the Tropics, however, extensive model deficits in runoff cannot be explained by either water or energy supply. We next examine what role the land model itself plays in biasing evapotranspiration and runoff.

Consideration of the relation between long-term mean radiation and water balances yields further insight into the behavior of land in both models and effectively accounts for biases in modeled precipitation and radiation. We fit the Turc-Mezentsev-Priestley-Taylor (TMPT) model (see Appendix D) to the observations and model data. The TMPT model is $E/P = [1 + (E_p/P)^{-\nu}]^{-1/\nu}$ with E_p given by $E_p = \frac{\alpha\Delta(R_n - G)}{\Delta + \gamma}$. The parameter α essentially measures the magnitude of potential evapotranspiration relative to the available energy supply. The canonical value for α of 1.26 is based on field studies, but lower values commonly have been reported, and a value of 1 is theoretically predicted for the condition of "equilibrium evaporation." For the observations, after interpolation to either model grid, we obtained TMPT parameters ($\nu = 2.04/2.12$, $\alpha = 1.06/1.05$) that are consistent with those commonly found in the literature (Figures 8a and 8b). When the evapotranspiration fractions (ratio of mean evapotranspiration to mean precipitation) are compared to the observations-fitted TMPT model predictions, a strong bias toward excessive evapotranspiration (hence insufficient runoff) is apparent in both models (Figures 8c and 8d). To make ESM2G/ESM4.1 fit the TMPT model, we found it was necessary to raise the values of α to 1.75/1.80. Such large values of α imply that, except in arid regions where water supply is a strong limiting factor, both ESM2G and ESM4.1 evaporate water much more readily than observed for a given level of net radiation and temperature.

Seeking further insight into the bias in water-balance partitioning simulated by both ESM2G and ESM4.1, we computed the models' global transpiration ratios (ratios of global transpiration to global total evapotranspiration) and compared them with an estimate based on global upscaling of observations (Wei et al., 2017). The observational estimate of the transpiration ratio is 57% (SD = 57%). The global transpiration ratios of ESM2G and

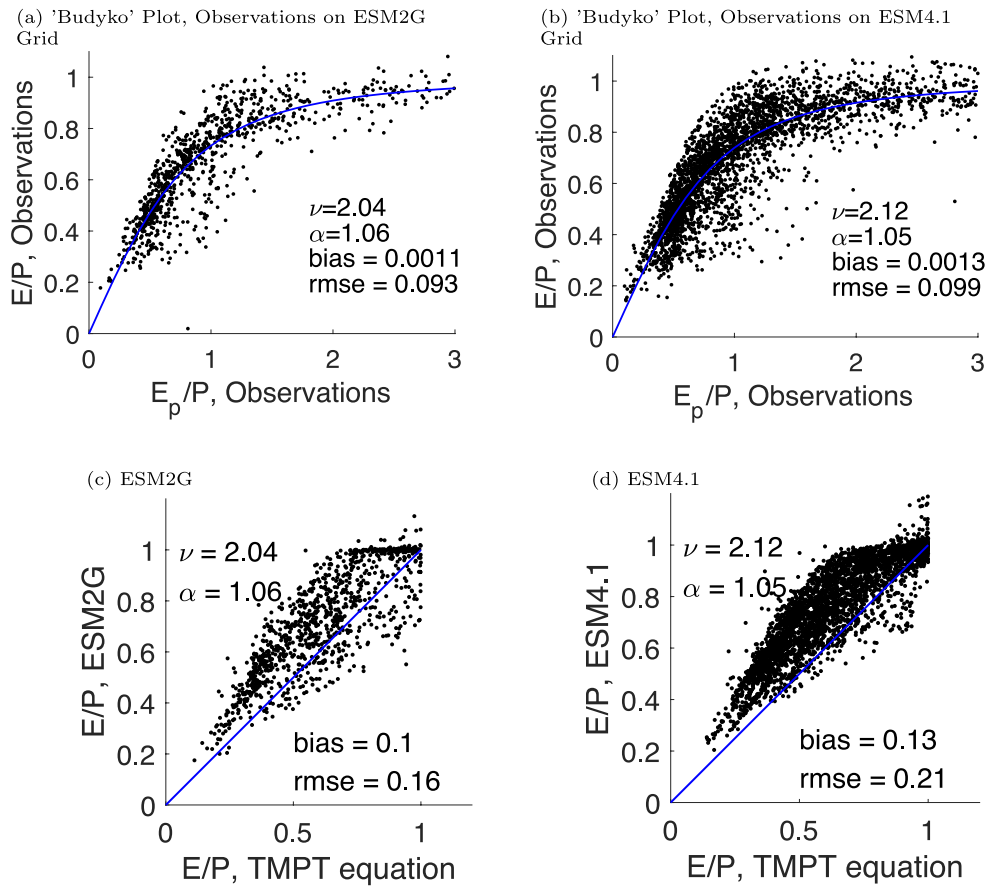

Figure 8. Application of observation-fitted TMPT equation to model outputs. (a and b) Evapotranspiration ratio versus index of dryness, observations and fitted curve (c and d) scatter plots of model evapotranspiration ratio against predictions of evapotranspiration ratio by observation-fitted TMPT equation (Appendix D). For the observations and the models, data were used only from grid cells at which the observational estimates of precipitation differed by no more than 10% from the sum of the observational estimates of runoff and evapotranspiration.

ESM4.1 are 45% and 39%, respectively, both significantly lower than the observational value. In a recent analysis (Berg & Sheffield, 2019), the global transpiration ratios for 32 CMIP6 climate models were found to range from 15% to 60%, with a median value of 42%, consistent with the values from ESM2G and ESM4.1. We speculate that the resistance to evaporation at the soil-atmosphere interface in ESM2G and ESM4.1 is unrealistically low (Milly et al., 2014), and that this deficiency of the models explains both the low bias in the global transpiration ratio and the high bias in evapotranspiration relative to what would be expected for a given supply of energy and water. While ESM4.1/LM4.1 has distinct transpiration and intercepted evaporation fluxes with associated resistances, it does not account for the effects of the laminar surface layer on evaporation from the soil. The future version of LM4.1 will explore the implications of the additional laminar resistance on land-atmosphere exchanges and the partitioning of transpiration to soil evaporation.

4.2.5. Soil Moisture

At climate timescales, the balance among the aforementioned hydrologic fluxes (precipitation, evapotranspiration, and runoff) also determines the average water storage within the soil column, such that biases in modeled (ESM2G and ESM4.1) soil moisture in a given region can be largely explained by the corresponding biases in these fluxes. Figure 9 shows the bias in annual mean soil moisture (averaged over the top 0–5 cm layer) for ESM2G and ESM4.1 relative to satellite observational estimates from the SMAP (Soil Moisture Active Passive) mission (Das et al., 2019; P. E. O'Neill et al., 2019). The geographical pattern of biases is fairly similar in both models, but with generally larger magnitudes in ESM2G, indicating improved soil moisture estimates in ESM4.1.

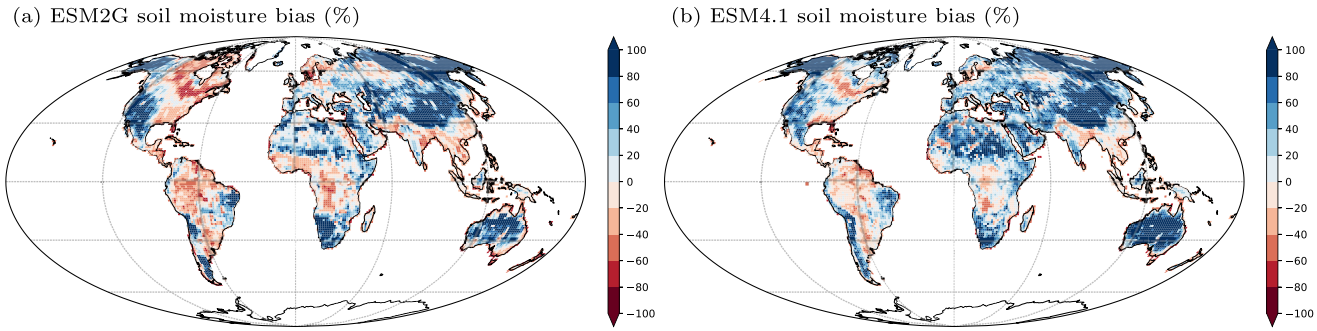

Figure 9. Bias (%) in ESM2G and ESM4.1 annual-mean soil moisture relative to observational estimates from the SMAP mission (L3 v6 product). SMAP data spans the period 2015–2019 and is representative of the top 0–5 cm soil layer (Das et al., 2019; P. E. O'Neill et al., 2019), and model outputs were averaged over the same period and depth. Both ESM2G output and SMAP data were regridded to the ESM4.1 grid.

Consistent with precipitation biases discussed earlier (Figures 6a and 6b), both ESM2G and ESM4.1 simulate wetter soils in arid and semi-arid regions (southwestern North America, Australia, and North and South Africa), and drier soils in the tropics and South Asian monsoon regions (Figures 9a and 9b). The evident negative soil moisture bias in the northeast of North America, where models exhibited a positive precipitation bias (Figures 6a and 6b) is attributed to excessive evapotranspiration in this region (Figures 6c and 6d) that exceeds its precipitation counterpart. Averaged over all land area, soil moisture bias is 0.03 $m^3\ m^{-3}$ in ESM2G (average soil moisture is 0.24 $m^3\ m^{-3}$), and 0.02 $m^3\ m^{-3}$ in ESM4.1 (average soil moisture is 0.27 $m^3\ m^{-3}$). Both models have a root mean square error (rmse) of 0.1 $m^3\ m^{-3}$.

4.2.6. Permafrost

The spatial distribution of permafrost estimated from observations is controlled largely by atmospheric temperature, with permafrost regions mostly being bounded by a contour of mean annual air temperature of −2°C or lower (R. J. E. Brown, 1960) (Figure 10a).

The model explicitly represents phase changes of water in the soil (Milly et al., 2014). The soil freezing curve is approximated as a step function: all phase change occurs at a soil-water-freezing point, which is a soil constant. The area of permafrost in ESM2G (2.4×10^7 km^2) greatly exceeds that estimated from observations (1.54×10^7 km^2), partly due to an atmospheric cold bias in the model. However, the ESM2G permafrost area extends southward beyond the model's own −2°C isotherm, suggesting that part of the permafrost area bias is attributable to a deficiency in the land component of ESM2G. Unlike ESM2G, ESM4.1 has a reduced permafrost area (1.34×10^7 km^2). The observed relation between the −2°C isotherm and the boundary of permafrost in ESM4.1 is similar to observations, but the ESM4.1 permafrost area is positioned further North of the model's own −2°C isotherm, making its permafrost area less than observations. The improvement of the overall permafrost area in ESM4.1 compared to ESM2G appears to be a result of changes in the prescribed properties of snow, with a more realistic (lower) thermal conductivity in LM4.1 (Milly et al., 2014). The lower thermal conductivity enhances the insulating effect of snow, which tends to keep the soil warmer during winter.

Figure 11 shows time series of permafrost area anomalies (departures from the 1971–2000 mean area) as well as corresponding temperature change. Both ESM2G and ESM4.1 show apparent decreasing trends of permafrost area after 1990, following the increasing trends of temperature. Most of the time, the simulated temperature in ESM4.1 is warmer than that in ESM2G, leading to a smaller area of permafrost in ESM4.1. Overall, the change in permafrost area follows the change in temperature; a smaller permafrost area is generally aligned with a warmer climate.

4.3. Trends

4.3.1. Near-Surface Air Temperature

The time evolution of the global continental LSATs from historical ESM4.1 and the Berkeley Earth Surface Temperature (BEST) data set (Rohde et al., 2013) are displayed in Figure 12. The BEST data set has the longest temporal coverage among available global LSAT data sets and is based on almost 46,000 time series. We find

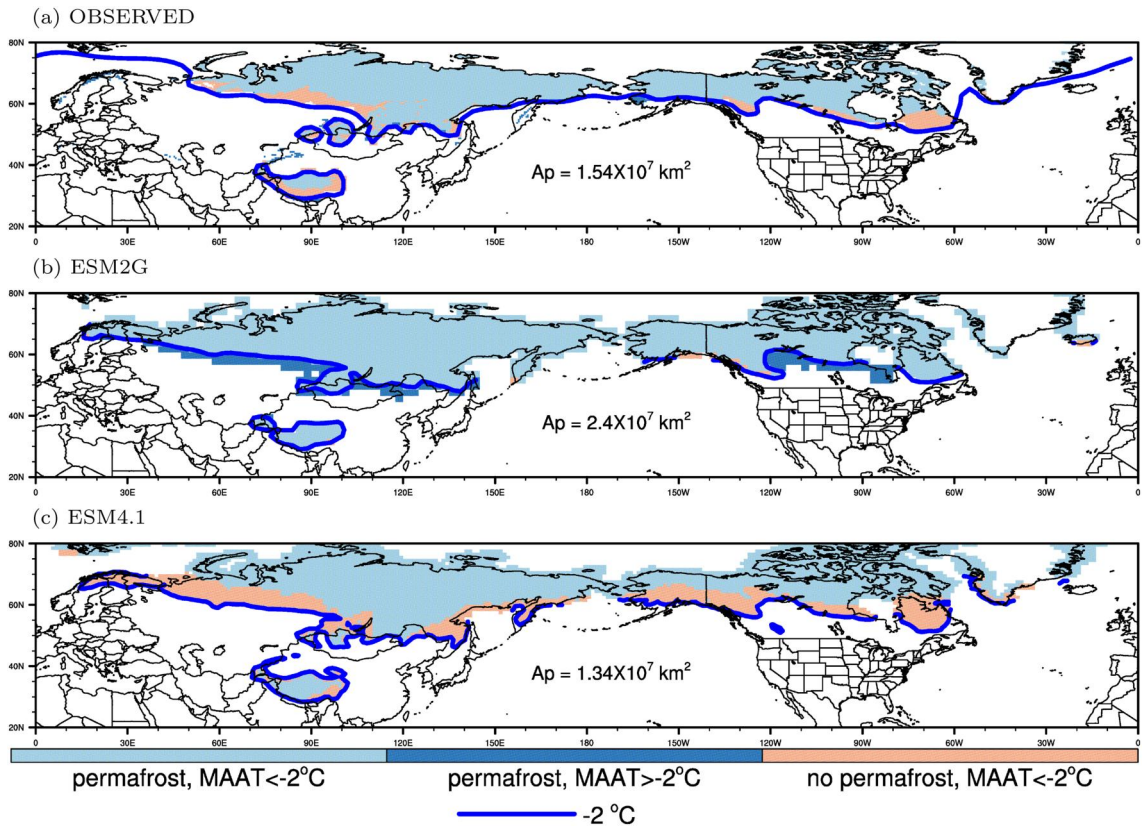

Figure 10. Observed and modeled spatial distributions of permafrost. The variable Ap is the total area of permafrost in the Northern Hemisphere. The blue line is the −2° C isotherm for mean annual near-surface air temperature (MAAT) from NCEP reanalysis, ESM2G and ESM4.1 respectively. Light blue indicates the presence of permafrost at MAAT below −2°C, dark blue indicates presence at MAAT above −2°C, and salmon color indicates absence at MAAT below −2°C. Observed permafrost presence determined by classification as continuous plus discontinuous, implying greater than 50% area underlain by permafrost (J. Brown et al., 2002). Modeled permafrost presence indicated where cells had at least 15 years in the period of 1971–2000 that were identified as permafrost. Permafrost was determined for a year if soil liquid content remains at zero from the beginning of the previous year to the end of this year at a depth of 5 m.

ESM4.1 performs well in regional temperature trends against historical observations in many regions, particularly in the second part of the twentieth century. While the overall warming from the late nineteenth century through 2014 agrees well with the warming trends in BEST data sets, there is an underestimation of warming trends in North America and Eurasia (see Figure 12b). The temperature anomalies with respect to the 1951–1980 period of LSAT in the Northern Hemisphere (NH) are similar to the behavior and biases seen in the GFDL CM4.0 model

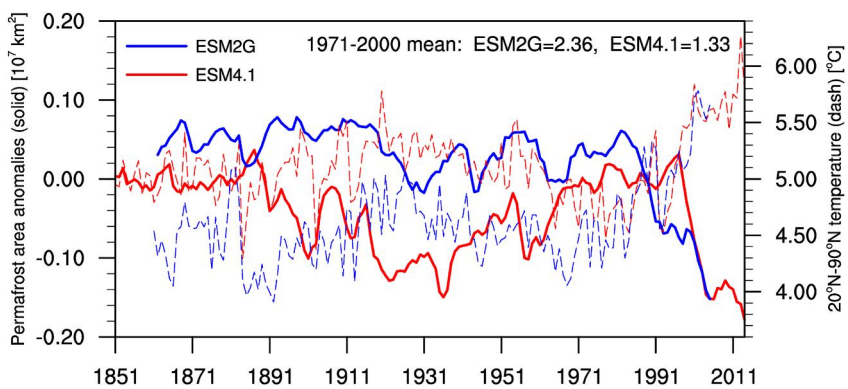

Figure 11. Time series of permafrost area anomalies (departures from the 1971–2000 mean area) and near surface temperature on land averaged over 20° to 90°N.

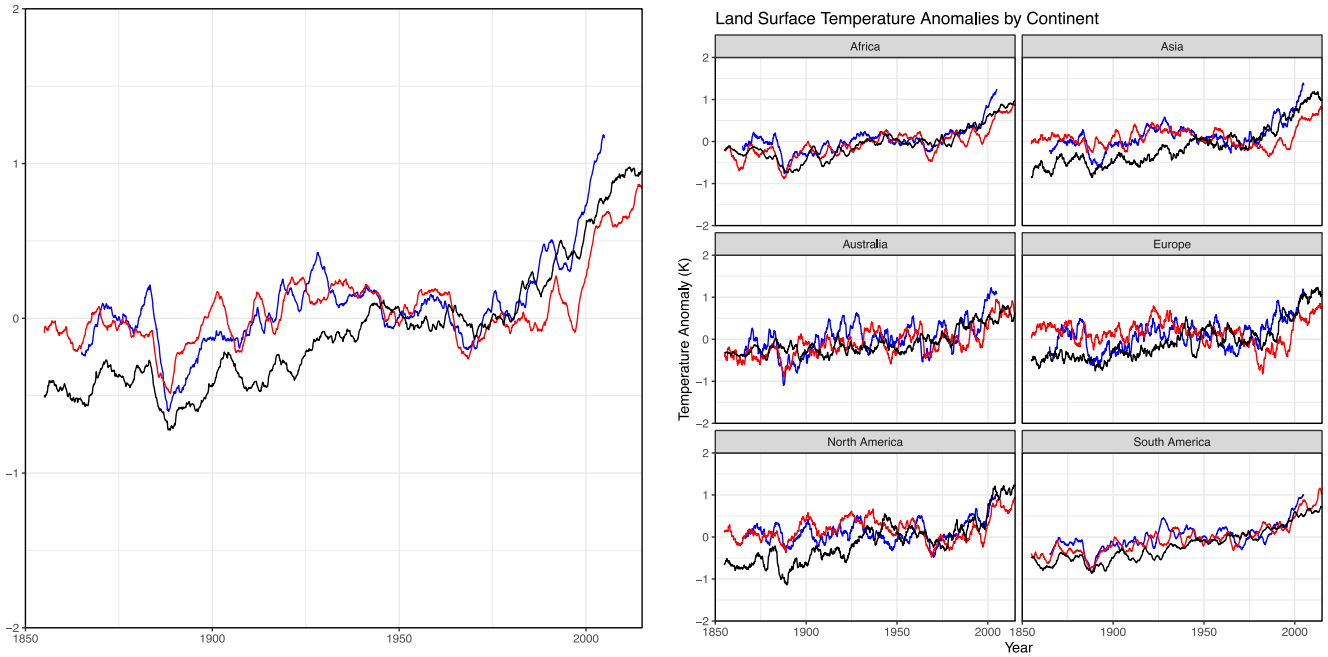

Figure 12. Historical surface air temperature anomalies over land relative to 1951–1980 period. The ESM4.1 (red line) and ESM2G (blue line) land surface air temperature anomalies were filtered using the available data mask from Berkeley Earth Surface Temperature (BEST) data set (black line) to account for missing data in the BEST data set. The plots show 60-month moving averages computed from the monthly model output and BEST data set.

(Guo et al., 2018; Held et al., 2019), which has a similar atmospheric physics (33 layers, simplified chemistry) and dynamics and ocean model (1/4° resolution) as well as the same atmospheric forcing (except for the use of prescribed ozone distributions from CMIP6) and land-use scenarios but a different land model LM4.0 (closer to LM3.0 configuration). Similarly to CM4.0 (Held et al., 2019), a strong NH aerosol forcing counteracts global warming from increases in GHG until almost the last quarter of the twentieth century. With the reduction of the aerosol forcing and continued increases in GHG, the NH land warms faster in ESM4.1 but still at a lower rate in Eurasia than indicated by the BEST data set. In the Southern Hemisphere (SH) the ESM4.1 reproduces temperature trends well but exhibits higher variability than observed in the BEST data set. The model's large SH multi-decadal variability is consistent with quasi-periodic polynya activity in the polar SH oceans as well as long-term climate variability in both CM4 and ESM4.1 simulations (Dunne et al., 2020a; Held et al., 2019).

4.3.2. Precipitation

A comparison of precipitation trends for 1901–2014 (Figures 13 and 14) over relatively well-observed global land regions indicates that while ESM4.1 captures precipitation trends over some regions (e.g., Africa, Western Europe, Central Asia), it does not capture the observed wetting trends in many regions of the world and instead simulates drying trends over large areas of South America and East and South Asia. Spatial patterns of wetting/drying trends over Australia, Northern Asia, and North America, particularly in the arctic-boreal zone differ among three historical runs of ESM4.1. These differences are likely modulated by the aforementioned multi-decadal ocean variability. The tendency toward excessive drying (decreasing precipitation) since 1901 is a common bias among CMIP5 climate models (Knutson & Zeng, 2018) and GFDL CMIP6 climate models (e.g., CM4, Zhang et al., 2023). In each case, these drying trends are much more pronounced and excessive in the ESM4.1 simulations than in the observations, although observed data quality is an important limitation, particularly for the century-scale trends over sparsely populated, less-developed regions. A comparison of precipitation trends for the recent, better globally observed 1980–2014 period (Figure 14) indicates that one ensemble member (i.e., D201) captures precipitation trends over broader regions than other ensemble members (e.g., Africa, Europe, North America, Asia), presumably by chance. Coupled climate models and ESMs generate their own ocean and atmospheric climate variability on multiple time scales. Observed data sets only provide records of one manifestation of climate variability. All ensemble members tend to overestimate a drying trend over South America and most of Australia.

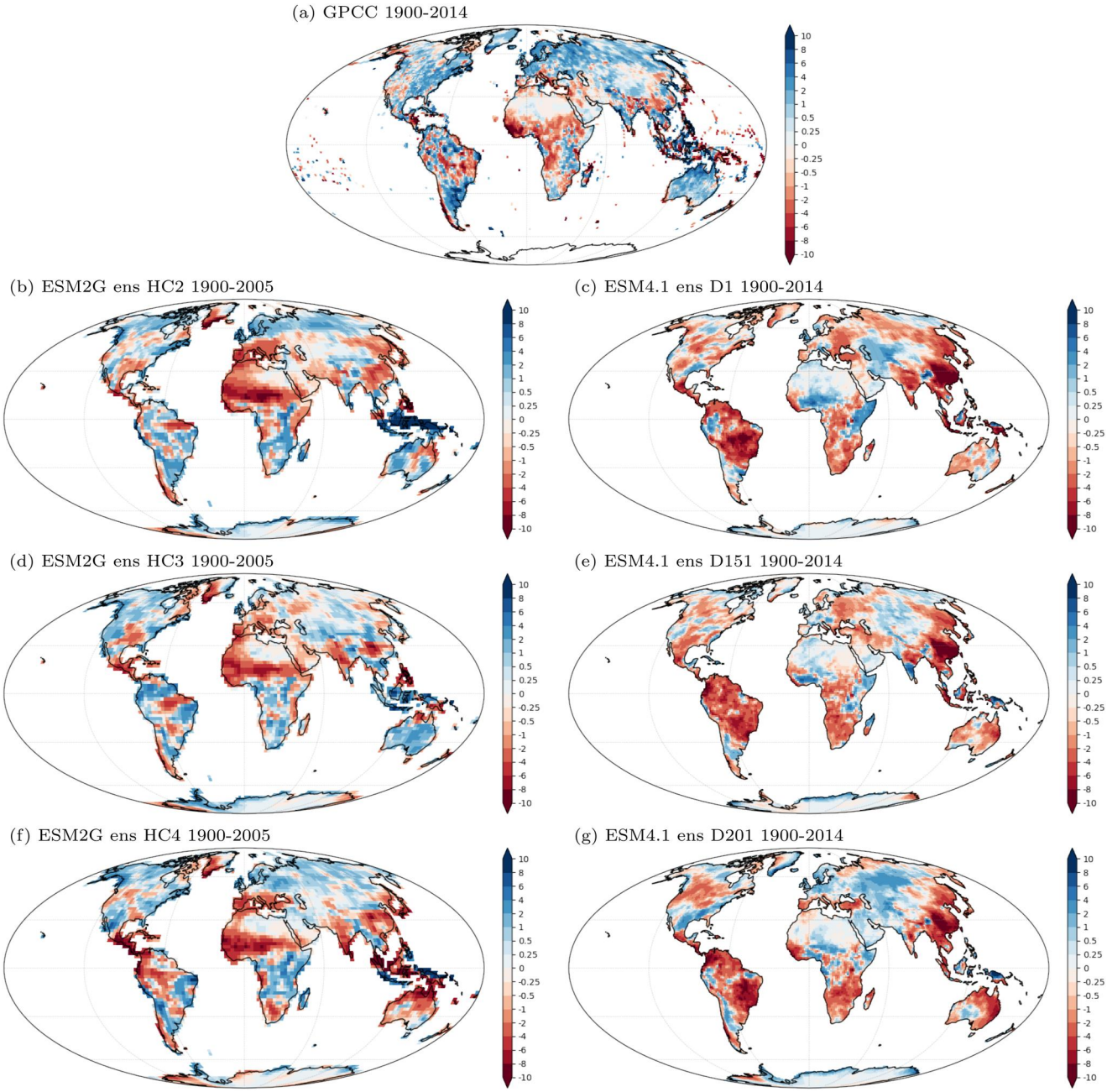

Figure 13. Observed (GPCC data over land) and simulated precipitation trends for long-term historical climate since 1900, mm/year/decade. Panels (b, d, and f) show three ensemble members of ESM2G simulation, and panels (c, e, and g)—show three ensemble members of ESM4.1. Grid cells with sparse observations in the GPCC time series are not masked out.

5. Vegetation Characteristics and Terrestrial Carbon

5.1. Vegetation Type Distribution

The distribution of major vegetation types as a function of climate provides an opportunity to test the emergence and consistency of large-scale biogeographical patterns in the LM4.1 model. LM3.0 prescribes biogeographic climate limits. We evaluated the predicted distribution of dominant vegetation types in LM4.1 with respect to gradients of temperature and precipitation simulated by the model by constructing a model-based Whittaker (1970) diagram (Figure 15). While examining the diagram, it is important to bear in mind that several vegetation types can coexist on each grid cell and that the diagram shows the dominant vegetation type according

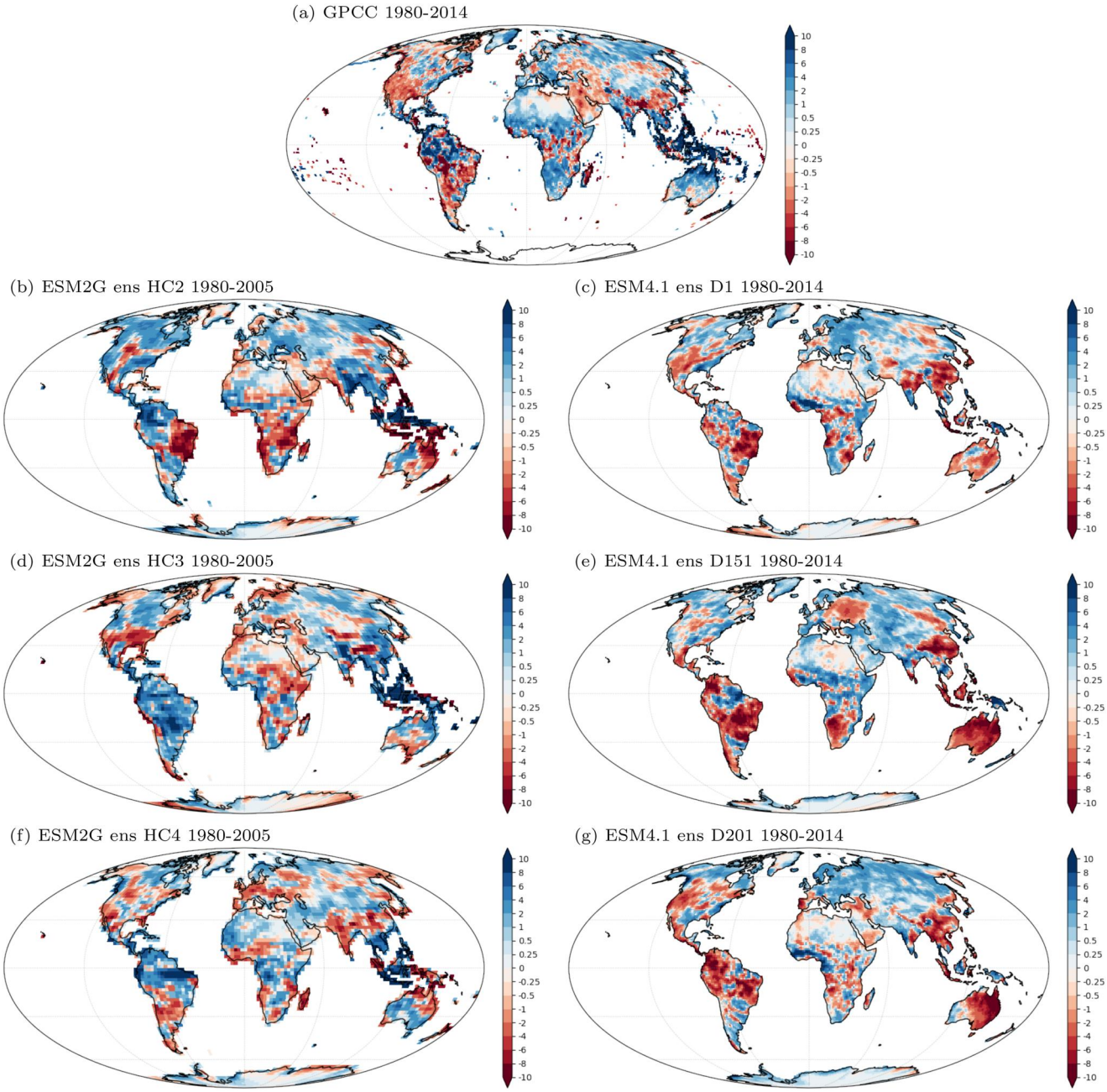

Figure 14. As in Figure 13, except for short-term historical climate since 1980.

to their biomass. This simplification leads to the predominance of high-biomass vegetation types (e.g., trees over grasses). One way to interpret the relationship between biomes, climate, and plant types mapped by Whittaker (1970) is as the illustration of relative importance of different vegetation types in distinct biological communities. For instance, the savanna is a mixed woodland-grassland ecosystem, whereas the relative dominance of coniferous trees versus grasses defines the transition from boreal forest to tundra biomes.

In general, LM4.1 captures major vegetation transitions in climate space, from bare soils occurring below −20°C to the dominance of tropical tree and grass vegetation types over temperate and conifer tree types at temperatures above −20°C. LM4.1 also captures the relationship between precipitation and the transition from grassland to forest-dominated landscapes at 1,000 mm of annual precipitation. The evergreen conifer tree is the dominant vegetation type over a wide range of conditions corresponding to tundra, boreal forests, and woodland biomes.

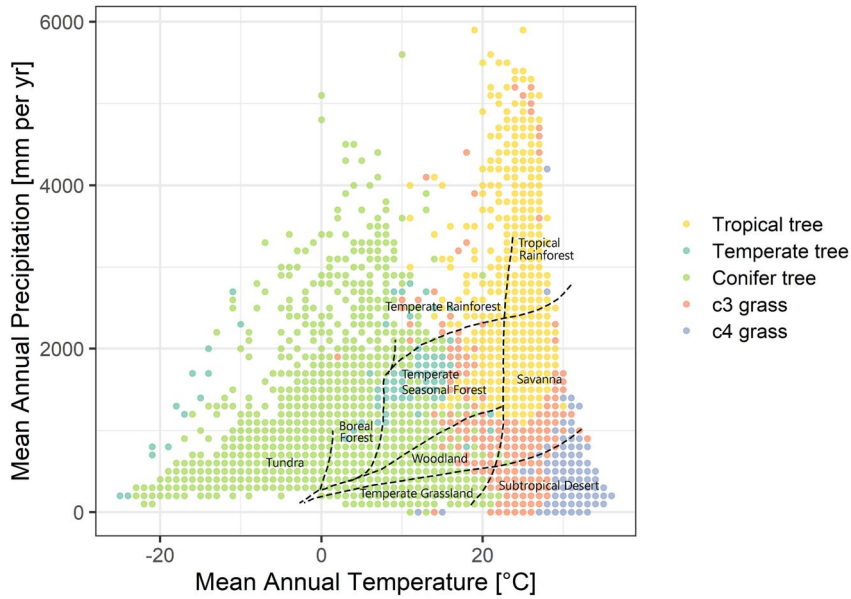

Figure 15. Distribution of dominant vegetation types in a climate space is defined by the mean annual temperature and mean annual precipitation. Each dot maps the dominant vegetation type, in terms of biomass, in tiles covered by natural and secondary vegetation. As a reference, the dashed lines show the inner boundaries of the idealized distribution of terrestrial biomes in Whittaker's diagram. Note that simulated temperature and precipitation levels extend beyond the idealized conditions, in better agreement with observed climate variability over land.

However, conifers also dominate vegetation biomass under climate conditions typically corresponding to temperate forests and temperate grasslands, suggesting the need to refine competitive dynamics in the model.

The temperate tree type occupies mild annual temperatures (5–18°C) and humid conditions (1,200–2,000 mm) and resembles the actual distribution of temperate seasonal forests, except for the displacement by the conifer tree type at the cooler end of its range. The tropical tree type dominates vegetation paralleling the distribution of tropical forests and wet tropical savannas (temperature between 20 and 30°C and precipitation above 1,000 mm). Grasses dominate the warm and dry areas, and the model correctly predicts the dominance of C4 over C3 grasses in subtropical deserts experiencing more extreme conditions (temperatures above 30°C). In the case of cold deserts, evergreen coniferous trees extend beyond the tree line into the tundra, where we expect a major prevalence of grasses.

In the very cold (e.g., high altitudes or high latitudes) climate, ESM4.1/LM4.1 simulates abundant coniferous trees and does not capture competitive dynamics well. This limitation could be partially attributed to the model's inability to capture processes limiting growth and establishment of trees. The next version of the model will explore parametrizations required to capture the implications of a short growing season and limited nutrients' availability on the tree/grass boundaries and simulations of tundra.

5.2. Gross Primary Production (GPP)

GPP is an ecosystem-level photosynthetic gain of CO_2 (Woodwell & Whittaker, 1968) and the major driver of land carbon uptake (Chapin et al., 2006). GPP is one of the key metrics in evaluating terrestrial components of ESMs (Anav et al., 2015). However, there are no direct observational measurements available to quantify GPP flux at the global ecosystem scale. The estimates of global GPP are derived via models from small-scale measurements such as eddy covariance flux towers (Beer et al., 2010; Jung et al., 2011) or remote sensing of global optical parameters related to vegetation activity such as the fraction of absorbed photosynthetically active radiation (FPAR) (e.g., MODIS data set, Running & Zhao, 2015), and, recently, observations of solar-induced chlorophyll fluorescence (Frankenberg et al., 2011), as well as from reconstructions of total global GPP based on changes in atmospheric composition (Campbell et al., 2017; Welp et al., 2011) (Figure 17). The global GPP estimates range from 90 to 210 GtC per year and vary substantially between studies employing different methods (Cheng et al., 2017). Based on eddy flux towers, Beer et al. (2010) estimated 123.6 ± 8.0 PgC yr^{-1} in the period

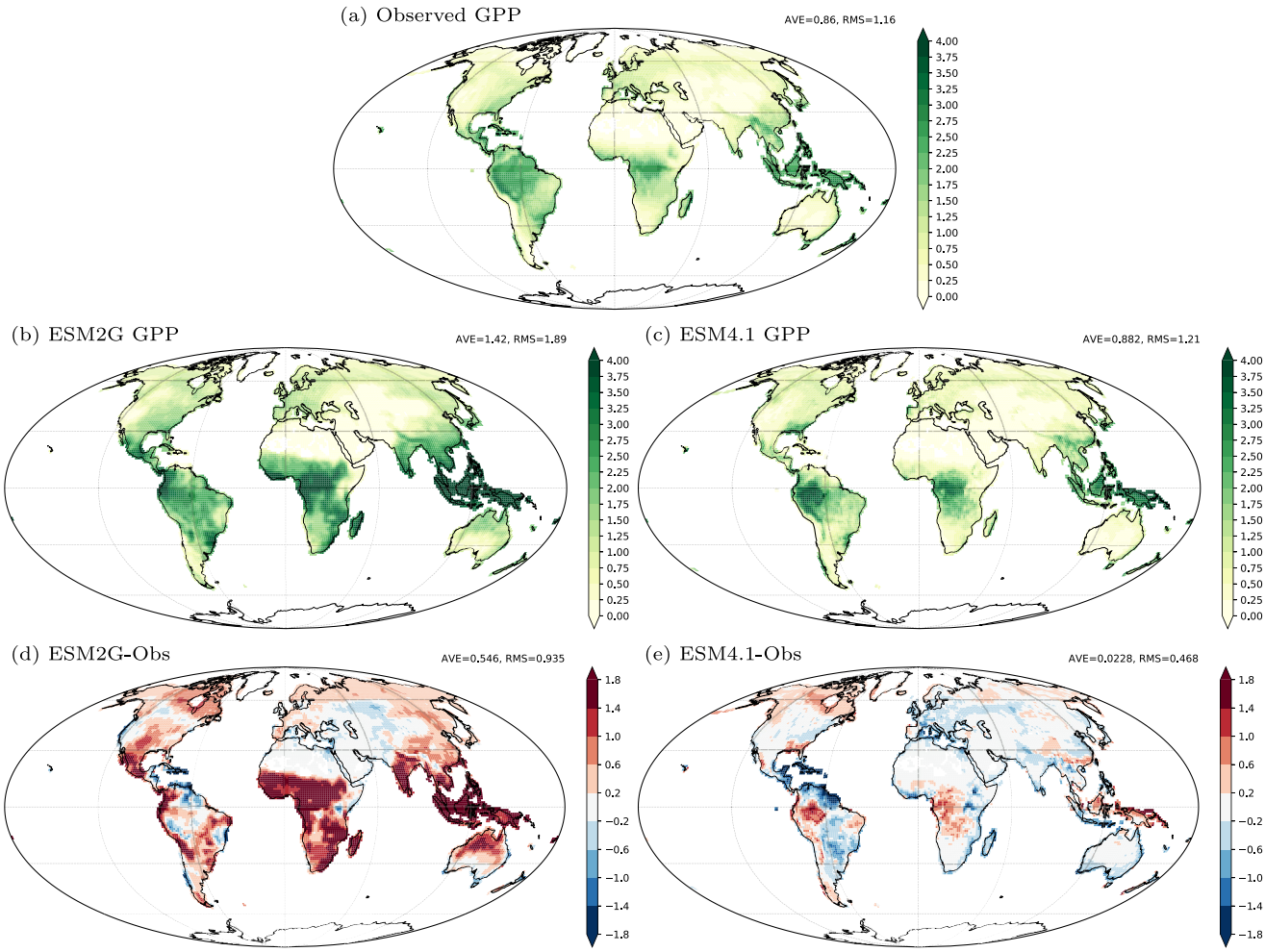

Figure 16. Distribution of annual gross primary production (GPP, kgC m^{-2} yr^{-1}) from (a) MODIS data set (Running & Zhao, 2015; Zhao et al., 2005), (b) ESM2G and (c) ESM4.1 simulations, and their difference with respect to MODIS data (d and e for ESM2G and ESM4.1, respectively).

1998–2005. Based on atmospheric CO_2 observations in a Carbon Cycle Data Assimilation System, Koffi et al. (2012) estimated global GPP at 146 ± 19 PgC yr^{-1} (1980–1999 period), similar to the Welp et al. (2011) estimate of 150–175 PgC yr^{-1} (1977–2009), based on the analysis of stable isotope ratios of atmospheric CO_2.

Here we compare spatial patterns of ESM4.1/LM4.1 and ESM2G/LM3.0 GPP (2000–2015) to the remote-sensing-based pattern from the improved Moderate Resolution Imaging Spectroradiometer (MODIS) (Running & Zhao, 2015; Zhao et al., 2005). Unlike eddy-flux-tower derived estimates, remote sensing-based estimates capture effects of natural and human disturbances (e.g., deforestation, fires, forest regrowth) and are suitable for the evaluation of GPP on decadal time scales in ESMs, which include representation of both environmental influences and land use change. Because of climate variability, one cannot expect specific disturbances and annual weather patterns to match month by month in each location. The ESM4.1/LM4.1 global mean GPP estimate is 109 PgC yr^{-1}, consistent with the MODIS-based estimate of 111 PgC yr^{-1} and is strongly correlated with a spatial pattern (Pearson correlation coefficient $r = 0.83$). The ESM2G/LM3.0 global mean GPP estimate is 180 PgC yr^{-1}, substantially higher than most estimates. The ESM2G GPP bias is related to a high bias in LAI, particularly in the NH, and to the dominance of trees on pastures instead of grasses due to annual grazing application.

Figure 16 shows that the spatial patterns in MODIS and ESM4.1/LM4.1 agree reasonably well in some areas while differing significantly in others. The ESM2G/LM3.0 positive bias in the Eastern hemisphere was substantially reduced in ESM4.1/LM4.1, likely due to revisions in the plant allocation scheme as well as the new

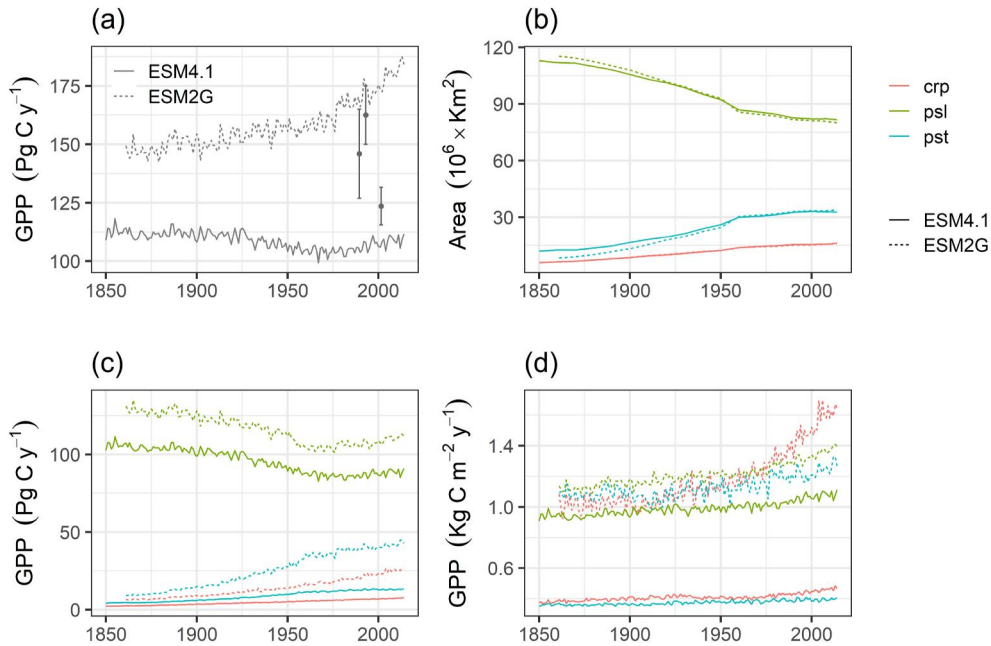

Figure 17. Evolution of gross primary production (GPP) and land use land cover change. (a) Historical total GPP (PgC yr^{-1}); (b) changes in land use area (red—croplands, blue—pastures, green—primary and secondary); (c) changes in GPP by land use type, (d) changes in GPP per unit area of land in different land use categories. Continuous and dashed lines represent ESM4.1 and ESM2G trends, respectively. Vertical brackets in (a) correspond to independent estimates of GPP by Beer et al. (2010), Koffi et al. (2012), and Welp et al. (2011) (see main text). Note that in ESM2G the historical simulations lasted until 2005, and predictions for the period 2006–2015 corresponded to scenario RCP8.5.

stomatal conductance formulation. Specifically, LM4.1 captures patterns in Asian and Eastern Europe boreal regions, Central North America, and extratropical Africa but simulates a higher level of GPP than MODIS in North America boreal zone, central Amazonia, and part of the African tropics and underestimates GPP in Northern and Eastern Amazonia and Western Europe. While MODIS and other observational data sets have the largest uncertainties in the tropics (Anav et al., 2015; Zhao et al., 2005), the discrepancy in South America is most likely due to climate biases in precipitation and moisture in both ESM2G and ESM4.1. In Western Europe, this low bias is likely induced by extensive wood harvesting prescribed through the scenarios of LULCC (Hurtt et al., 2020, https://luh.umd.edu/data.shtml) and by grazing intensity on pastures. In ESM2G/LM3.0 pastures in South America and Europe often had tree vegetation types instead of grasses as grazing was applied annually, which promoted high GPP throughout a year, accumulation of biomass, and as a result, assigned trees instead of grasses. These changes to GPP have huge benefits for the presentation of the seasonal cycle in atmospheric CO_2—decreasing biases by a factor of two, see Figure 34 in Dunne et al. (2020a).

ESM4.1/LM4.1 and ESM2G/LM3.0 simulate evergreen coniferous trees further into the tundra area, particularly in North America than observed. This overestimate of tree abundance in the North American boreal zone is likely related to the models' warm and wet biases in high latitudes as well as the lack of nutrient constraints. Weng et al. (2016) suggested that temperature affects the outcome of competition between high Leaf-Mass-per-Area (LMA) vegetation (i.e., long-lived evergreen leaves) and low-LMA vegetation (i.e., short-lived deciduous leaves) primarily due to its effect on the N mineralization rate. As a new version of LM4 with coupled C and N cycle is currently under development, we choose not to introduce into LM4.1 temperature-based biogeographic limits for boreal evergreen and temperate deciduous vegetation types and await that advance in future versions.

Recent GPP estimates derived from sun-induced chlorophyll fluorescence (SIF) suggest that GPP over croplands is much higher (50%–75%) than many terrestrial process-based models simulate because they represent agricultural areas as grasslands. The second reason for a low annual GPP bias in LM4.1 in areas dominated by croplands, particularly in the tropics, is a lack of double cropping—all crops everywhere are planted and harvested once in LM4.1. LM3.0 has no prescribed crop calendar and cropland's phenological cycle followed that of natural grasses. Another possible reason for lower GPP in arid areas is the absence of irrigation. On pasturelands,

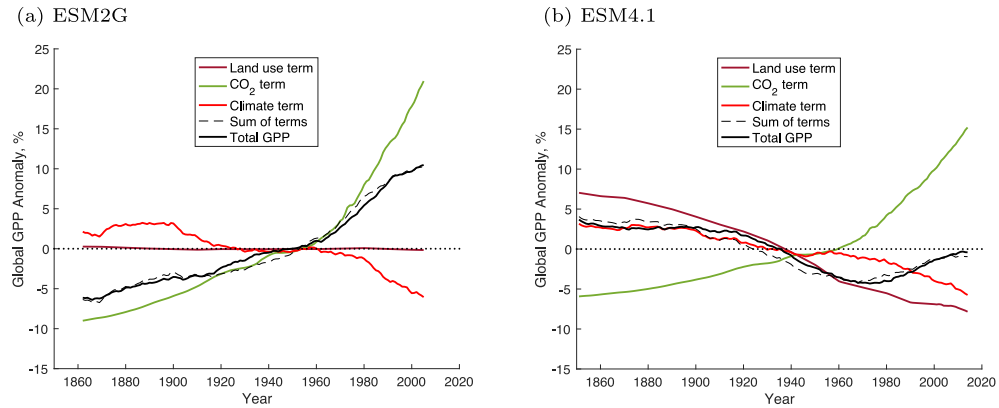

Figure 18. Approximate decomposition of temporal variation of global annual simulated gross primary production into components associated with changing land use, CO_2 fertilization, and climate. The curves showing the climate component and the total change have been processed through a 30-year LOESS smoother to highlight the long-term changes.

underestimation of GPP (Figures 17c and 17d) is related to low LAI caused by excessive grazing prescribed in LM4.1 (i.e., 5% daily and with an LAI limit of 1). It's well established that a linear relationship generally exists between annual GPP and leaf area duration, a product of LAI and growing season length (W. Wang et al., 2011), such that a lower value of daily grazing may have been more realistic.

Temporal variations in global annual GPP (Figure 17a) can be decomposed using multiple linear regression into components caused by temporal variations in land use (Figure 17b), climate (precipitation, temperature, and downward shortwave radiation), and atmospheric CO_2 concentration; an additional small term represents the interactions between land use and the other four factors (Appendix E; Figure 18). Net conversion of high-GPP natural and secondary vegetation to low-GPP (in the LM4.1 model) pasture, rangeland, and cropland results in a steady downward trend in GPP (Figure 18b). In LM3.0 land use conversion to cropland and pastures has little influence on the GPP trend (Figure 18a) because pastures were allowed to regrow, similarly to secondary vegetation, and the cropland conversion did not restrict the growing cycle in the absence of a crop calendar, particularly in tropics. Changing temperature induces a high degree of interannual variability and a steady downward trend in GPP in both models. Rising CO_2 is reflected directly in the induced rise in GPP in both models, so called CO_2 fertilization effect. The effects of changes in land use, climate, and atmospheric CO_2 concentration are additive, so the sum of all the effects closely follows the total model GPP, supporting the validity of the decomposition by multiple linear regression. Before about 1970, the decreases in LM4.1 GPP (Figure 18b) due to land use and temperature change outweigh the enhancement of GPP by CO_2 fertilization. Around 1970, the changes due to land use in LM4.1 decelerate somewhat, and the CO_2 effect accelerates so that the LM4.1 steady pre-1970 decline in global GPP is reversed, and global GPP partially recovers from the preceding decline.

5.3. Leaf Area Index

The area of leaves, measured as LAI, is a major characteristic of land vegetation, which plays a crucial role in intercepting solar radiation and precipitation as well as determining the amount of evapotranspiration and photosynthetic uptake, and therefore is an essential characteristic in predicting terrestrial carbon and energy exchanges. LAI is computed in ESM4.1/LM4.1 and ESM2G/LM3.0 from prognostic leaf biomass and vegetation type specific leaf areas (SLAs, leaf area per biomass). Both LM3.0 and LM4.1 only represent living leaves and assume that dead leaves are immediately senesced. We compared the spatial distribution of mean annual LAI (2010–2015) in ESM4.1/LM4.1 and ESM2G/LM3.0 to the remotely sensed estimates retrieved by the Terra Moderate Resolution Spectroradiometer (MODIS) (Z. Zhu et al., 2013). LAI observations from a satellite are known to have some biases and errors as compared to ground observations themselves (Fang et al., 2019), but are found to be useful in the evaluation of spatial patterns (Mahowald et al., 2016). Overall, LM4.1 captures the spatial gradients in the magnitude of LAI associated with major biome transitions (Figure 19) but tends to predict higher LAI values compared with MODIS estimates in boreal regions and parts of tropical South America and Africa. In high latitudes, model deviations arise from an excess in absorbed net radiation and precipitation that

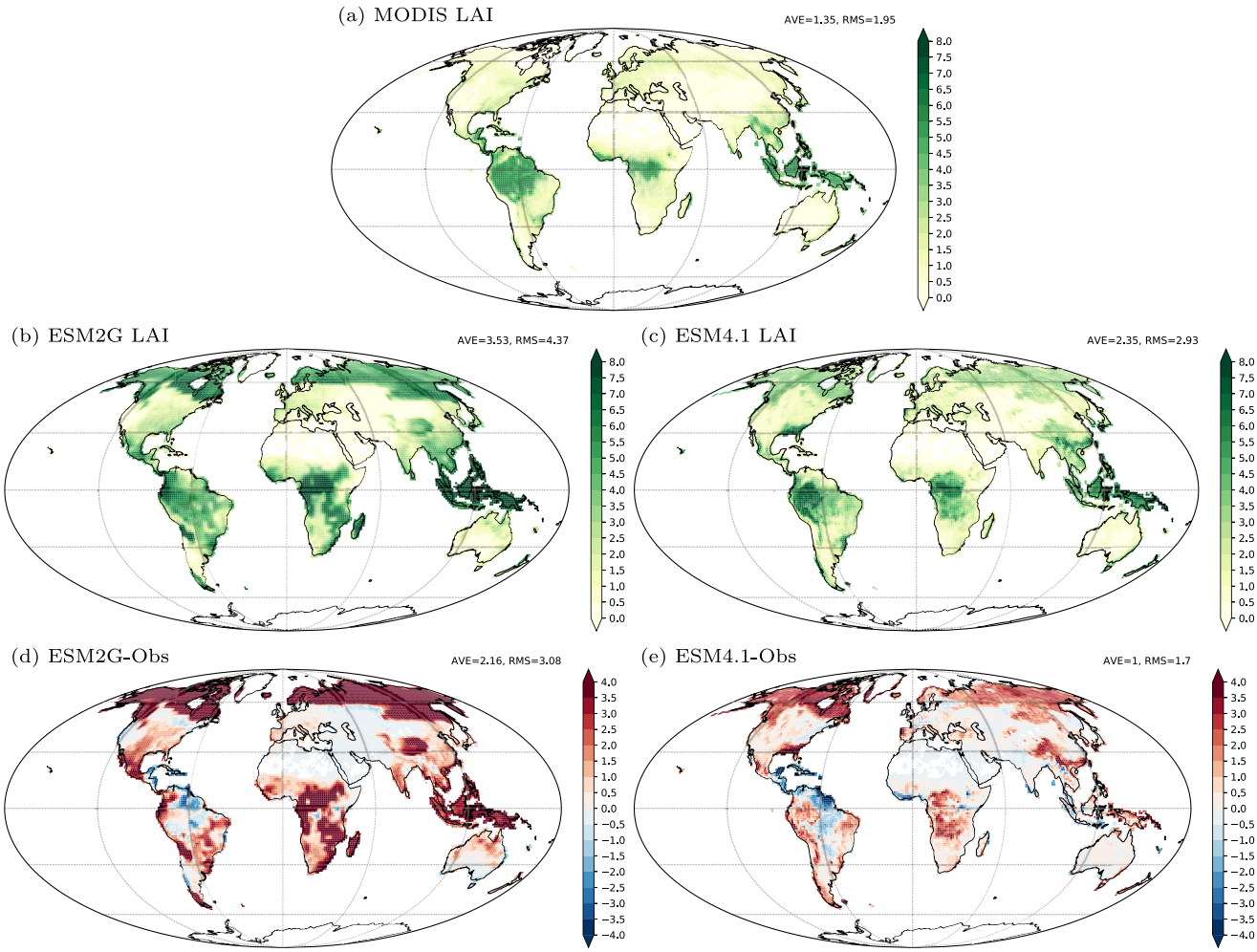

Figure 19. Comparison of annual mean leaf area index (LAI, m^2 leaf/m^2 ground) from (a) MODIS data set (Myneni et al., 2015), (b) ESM2G and (c) ESM4.1 predictions, and their difference with respect to MODIS data (d and e for ESM2G and ESM4.1, respectively).

results in a warmer climate. In Western Amazonia, the model underpredicts LAI due to substantial biases in precipitation and its inability to simulate tropical trees under a dry climate. Despite these prevailing issues, ESM4.1/LM4.1 represents a substantial advance with respect to ESM2G/LM3.0, with a decrease in the overall bias by about 50% which results mainly from a net improvement in the simulation of the boreal and tropical regions.

5.4. Aboveground Biomass and Tree Size Distribution

The ability of the model to reproduce global patterns of woody AGB is assessed in Figure 20. AGB is a major indicator of carbon stored in vegetation and has the advantage that there are reliable estimates based on direct tree field measurements and allometric models, and on remote sensing products including LiDAR. In addition, AGB plays a critical role in determining the key properties of the land surface, such as roughness, which in turn play important role in the land-atmosphere interaction. Furthermore, AGB serves as an important input for predicting fuel availability in the fire dynamics module. To assess the model's ability to capture large-scale gradients in AGB, we compared ESM4.1/LM4.1 and ESM2G/LM3.0 simulations for the period 2010–2015 with global AGB reconstructions derived from field plot estimates (Avitabile et al., 2016; Santoro et al., 2015). LM4.1 shows considerable skill and is able to capture major spatial gradients in AGB (Figure 20), with absolute deviations below 2.0 kgC m^{-2} over most of the land. The average bias suggests a slight decrease in skill with respect to its predecessor, LM3.0, where vegetation types were prescribed, but LM4.1 outperforms LM3.0 in most of the globe, except in the Neotropics. Because of biases in simulated climates and climate zones (Section 4), model skill is

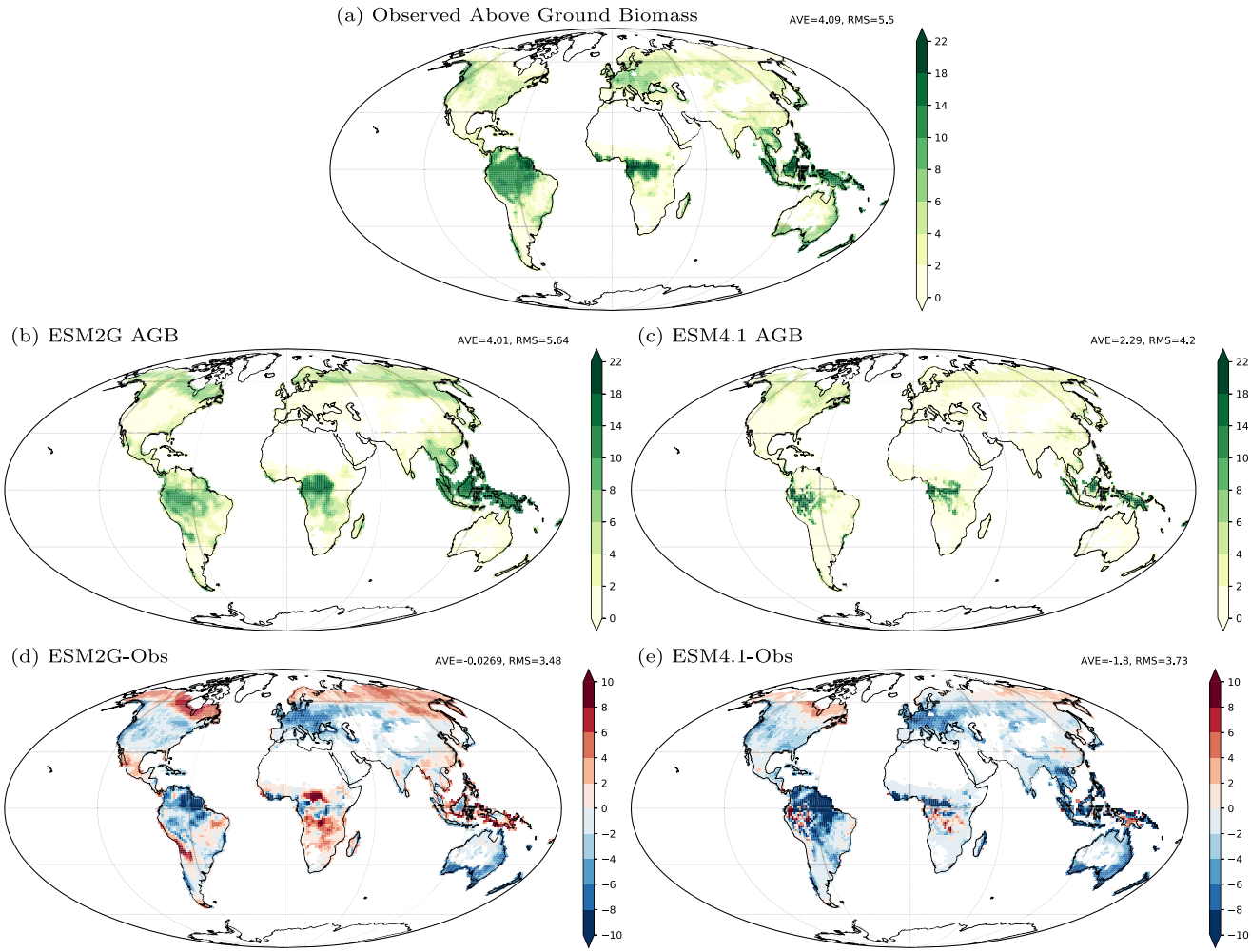

Figure 20. Maps of woody above ground biomass (AGB, kgC m^{-2}). Panel (a) shows AGB patterns generated by Avitabile et al. (2016) and Santoro et al. (2015), who interpolated AGB estimates at the plot level based on field observations and remote sensing estimates using machine learning methods. The other maps show woody AGB patterns based on (b) ESM2G and (c) ESM4.1 predictions for the period 2010–2015 and their difference with respect to observed patterns (d and e for ESM2G and ESM4.1, respectively).

somewhat degraded and does not match the location of large-scale ecotones between tropical, temperate, and boreal regions. Similarly, biases in the simulation of precipitation over the tropics lead to the underestimation of AGB in the northeastern end of the Amazon basin and central Africa. Although these biases were already present in ESM2G (Figure 20), LM4.1 exaggerates the underestimation of AGB in the Amazon basin. On the other hand, ESM4.1 substantially improves the overestimation of AGB along the boreal zone, subtropical regions of America, and vast areas in the Afrotropics in ESM2G.

The simulation of individual cohort dynamics represents a major innovation of LM4.1 that enables the characterization of forest structure in terms of size distribution patterns (i.e., the abundance of trees at different size classes and ages). Size distribution is an important emergent pattern to assess the evolution of vegetation carbon stocks, and the response and recovery potential of forest ecosystems to climate and atmospheric CO_2 perturbations and management interventions. Simulated forests in LM4.1 show a remarkable resemblance with observed patterns in size structure and captured differences across main biomes (Figure 21). Comparisons with individual-level reconstructions of size structure observed in tropical, temperate, and boreal forest plots revealed the ability of LM4.1 to reproduce the shape of the size distribution from seedlings to large trees. LM4.1 correctly captures the truncation of size distributions at comparatively small diameters in boreal forests, the smooth decline in abundance towards very large sizes in temperate latitudes, and the more equalized distribution of tree abundances in the tropics.

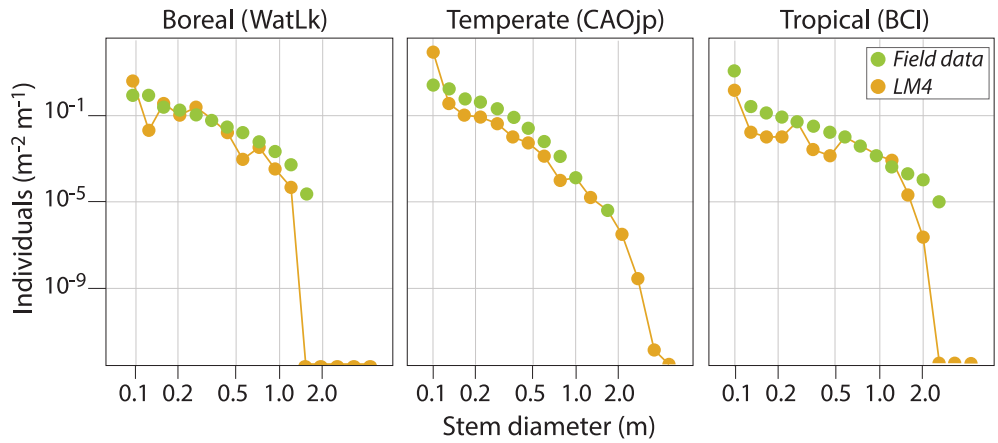

Figure 21. Comparison of tree size distribution observed at selected field locations for the main biomes (green dots) with respect to predictions derived from LM4.1 simulations (orange). Observed tree size distributions were calculated from forest plot census data retrieved at tropical (Barro Colorado Island, BCI, http://ctfs.si.edu); temperate (FIA, Forest Inventory and Analysis Program of the U.S. Forest Service for Northern lake states, following Weng et al. (2015)); and boreal (FIA, Alaska plots) biomes. Tree size distributions predicted by LM4.1 pool together individuals from all tree vegetation types. Simulated size distributions were calculated for tiles covered by natural and secondary vegetation within the closest model grid cell to each reference location. Each graph shows in a double logarithmic scale the normalized abundance of trees grouped into logarithmic bins.

5.5. Fire and Dust Emission Precursors

ESM2G/LM3.0 relies on a very simple fire parameterization with constant rates of fire return interval and lacks a dust emissions parameterization (dust aerosol concentrations are prescribed in the atmospheric component of ESM2G). This section focuses on the evaluation of fire characteristics in the ESM4.1/LM4.1 and driving variables of dust emissions. Burned fraction and fire-related carbon emission from ESM4.1 show generally similar spatial distributions as observations from GFED4.1s (van der Werf et al., 2017), Figure 22. Wildfire burned area was not archived in ESM2G experiments. Compared to observations, ESM4.1 simulates higher burned fraction and fire carbon emission across tropical and subtropical North America and Eurasia, as well as all of South America, while underestimating biomass burning activity across northeastern Australia, compared with GFED4.1s. Moreover, the global fire-related carbon emission amount from ESM4.1 is comparable with Fire Energetics and Emissions Research version 1.0 (FEER1.0; Ichoku & Ellison, 2014) and about 1.5 times that of GFED and Global Fire Assimilation System version 1.2 (GFAS; Kaiser et al., 2012). While fire carbon emissions from FEER are estimated from satellite observations of fire radiative power and aerosol optical depth (AOD) from the Moderate Resolution Imaging Spectroradiometer (MODIS), carbon emissions from GFED and GFAS are based only on satellite retrievals of burned area and no AOD constraints (Pan et al., 2019). Therefore, the amount of fire-related carbon emissions simulated by ESM4.1 is largely consistent with observation-constrained estimates. A recent extreme fire attribution study with ESM4.1/LM4.1 (Yu et al., 2021) evaluated the contributions of natural and anthropogenic ignition activities, anthropogenic climate variability and change, and human influence on the occurrence of the extreme fire season in Alaska and found that burned area and fire carbon emissions have increased since the 1950s in Alaska, especially in July, resulting in more frequent extreme events.

One of the key drivers of dust emissions is land surface bareness, which is defined in LM4.1 as areas with LAI or SAI less than 0.1 and 0.01, respectively. In LM4.1 fires can affect dust emission by creating bare surfaces that can act as dust sources. Satellite observation shows enhanced dust emission following large wildfires due to vegetation disturbance (Yu & Ginoux, 2022). Figure 23 shows the comparison of surface bareness for 2000 derived from AVHRR (Defries & Townshend, 1994) and simulated by ESM4.1. We see an overall agreement in Africa, Asia, and North America. ESM4.1 exhibits large areas across Australia and the northeast edge of South America, which could be associated with wildfires simulated during the historical run and not observed in 2000.

5.6. Land Carbon Stocks and Fluxes

For the present day, LM4.1 simulates total vegetation carbon of 345 PgC, which is within the overall range of the 42 observation-based reconstructions obtained by Erb et al. (2017) but below the mean estimate of

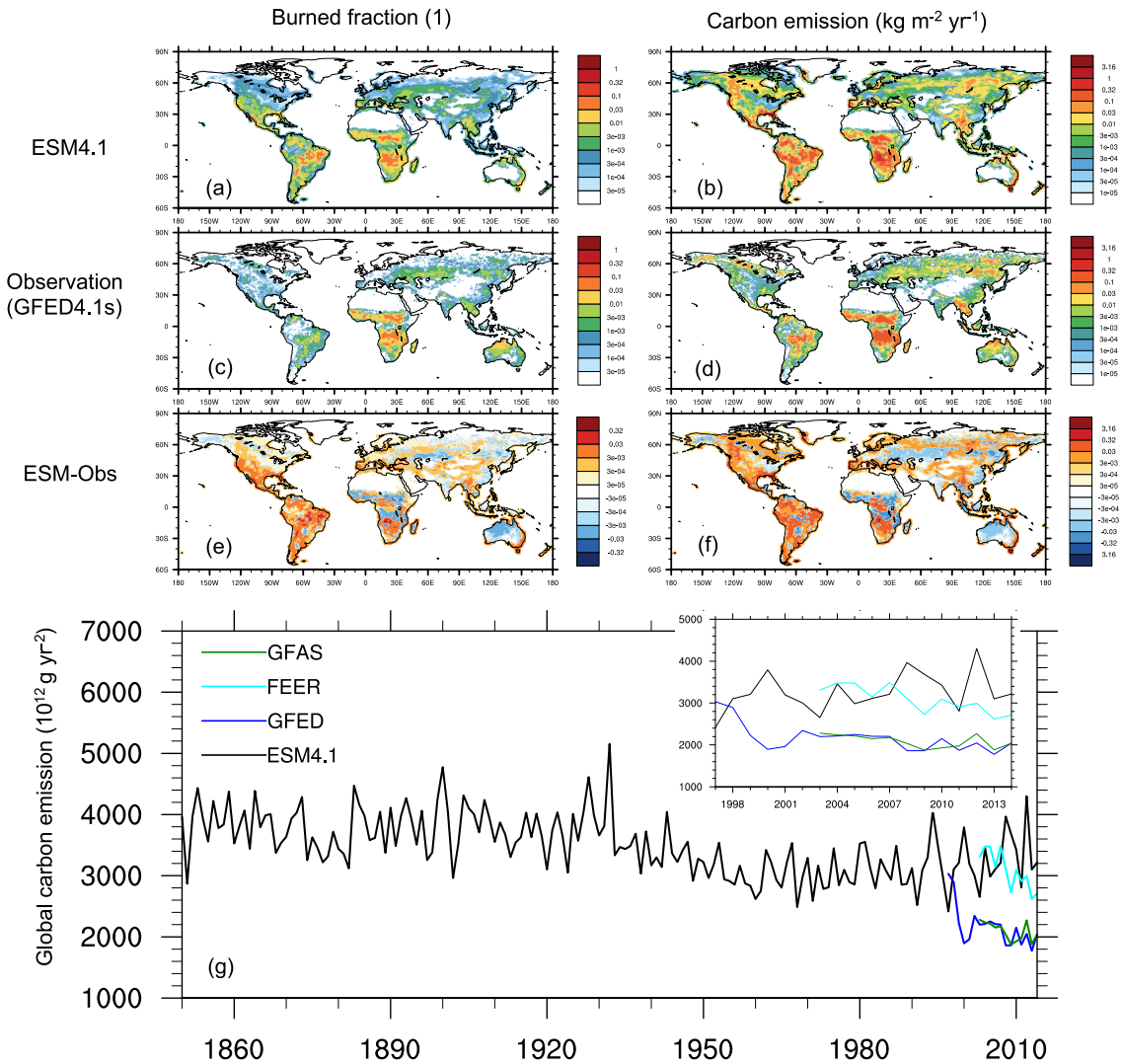

Figure 22. Comparison of biomass burning from ESM4.1 and observational data sets. (a and b) Simulated, (c and d) observed, and (e and f) their difference of annual mean (a, c, and e) burned fraction and (b, d, and f) fire carbon emission ($kgm^{-2}yr^{-1}$) during 2000–2014. (g) Time series of global fire carbon emission ($1{,}012\ gyr^{-1}$) from ESM4.1 and three observational data sets during 1997–2014. The three observational data sets include GFED4.1s (van der Werf et al., 2017), Global Fire Assimilation System version 1.2 (GFAS) (Kaiser et al., 2012), and Fire Energetics and Emissions Research version 1.0 (FEER1.0) (Ichoku & Ellison, 2014).

447 PgC (inner 50% percentiles 375 to 525 PgC). The main shortcoming of the LM4.1 simulation is an underestimation of tropical total biomass by approximately 100 Gt, particularly in Amazonia due to climate biases (e.g., very limited tropical rainforest climate zone, see Figure 6), excessive overgrazing on pastures, and, potentially, excessive biomass loss due to wildfires (Martínez-Cano et al., 2022). One potential strategy for improving the distribution of vegetation carbon in the tropics is revising the representation of competition between grass and trees during establishment. Another strategy would be to lower grazing intensity estimates and allow some trees to regrow on pastures, which currently have very low biomass in most of tropical South America and Africa.

As a result of low biases in vegetation biomass, that lead to a reduction in soil litter inputs, the soil carbon and surface litter stock of 514 PgC is lower than in previous generations of GFDL ESM2G (1,422 PgC). In addition, the LM4.1 soil carbon estimate does not include any carbon in the permafrost as its soil carbon model does not account for peat formation and cryoturbation. The LM4.1 soil carbon model simulates carbon in a vertically resolved manner and was allowed to accumulate soil carbon only in layers that were not frozen. One strategy for future efforts would be to develop a method for initializing soil carbon in frozen soil layers in preindustrial experiments as, to our knowledge, there is no observational data set available to perform such initialization in

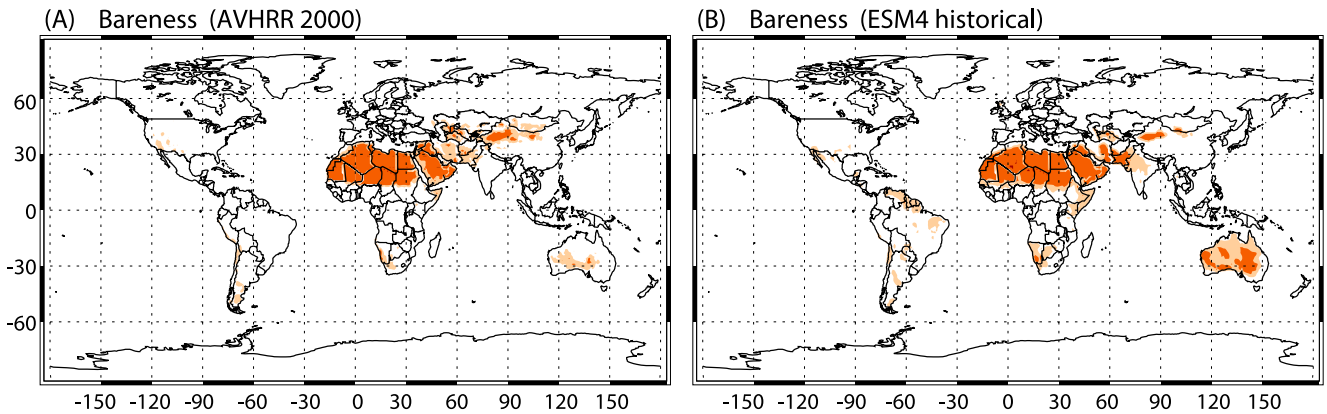

Figure 23. (a) Surface bareness (soil surface free of any vegetation) for 2000 as derived from AVHRR satellite data and (b) calculated by ESM4 historical simulation. Light and dark red shading correspond to bareness fraction greater than 0.1 and 0.5, respectively.

perpetual 1850 conditions. As a result of the underproduction of plant biomass in tropical regions due to climate biases and overgrazing on pastures, the model predicts for 2000–2009 a small land carbon sink of 0.53 PgC yr^{-1} in one of the ESM4.1 ensembles and even smaller sink in the other two ensembles, but still within the range of the Global Carbon Budget estimate (0.4–2.2 PgC yr^{-1}) (Friedlingstein et al., 2019).

6. Conclusions

The Grassl (2000) outlook for the early 21st century included anticipation of wider use of CGCM-based ESMs to better represent the implications of human activities for the climate system. A new land physics and ecosystem model LM4.1 has been developed at the GFDL as part of the new ESM4.1 model development effort (Dunne et al., 2020a). This effort builds on a laboratory-wide 4th generation model development effort over 2014–2018 that resulted in the AM4 atmosphere (Zhao et al., 2018), OM4 ocean (Adcroft et al., 2019), and CM4 coupled (Held et al., 2019) models, and unifies advances across several past development efforts. LM4.1 highlights land-atmosphere interactions, including hydrological, carbon, and mineral dust exchanges, ecosystem comprehensiveness including vegetation competition for light and water, land-use, gaily crown and multi-day fire, and prognostic dust. These features vastly improve climate mean patterns and variability from previous models. Additionally, LM4.1 includes representation of the rangelands, daily—instead of annual as in LM3.0—grazing and prescribed crop calendar.

Several critical simulation challenges also remain, however. LM4.1 likely overestimates the influence of land use and land cover change on many vegetation characteristics, particularly on pasturelands, and as a result simulates lower present-day biomass and carbon uptake compared to both observations and the previous generation of GFDL ESMs, which overestimated vegetation carbon pools and GPP (Dunne et al., 2013). In coupled mode, LM4.1 provides improvements relative to previous model versions in the fidelity of many simulated land surface characteristics including representation areas of permafrost, diurnal cycle, and historical climate warming (Section 4) as well as of general bioclimate and associated vegetation characteristics such as the spatial patterns of aboveground biomass and GPP (Section 5). However, some representational challenges remain. The Amazon dry bias and associated seasonally low productivity, while vastly improved over the previous generation of GFDL ESMs, continue to pose a challenge. Soil moisture suffers from a high bias in northern subpolar regions where coniferous vegetation extends too far poleward. Excessive overgrazing leads to the underprediction of GPP and subsequently to a lower biomass accumulation and LAI over pasturelands. Similarly, the absence of double cropping in tropical regions also contributes to lower values of both LAI and GPP. Despite the differences in simulated and observed bareness (Figure 23) in the Northeast edge of South America and Australia, the dust emissions would not necessarily be biased. As recent studies suggest substantial sources in those regions could be associated with seasonal, not muti-year bareness, and vegetation loss due to fires (Yu & Ginoux, 2022). Future GFDL land model development will integrate existing GFDL land capabilities, including the urban canopy model (Li et al., 2016a, 2016b), water quality (Lee et al., 2023), and N cycling in plants and soils (Sulman et al., 2014, 2019) and seek to improve the competitive plant dynamics (Detto et al., 2022), subgrid hydrological heterogeneity

(Chaney et al., 2018), and urban water management (Xie et al., 2021). Once biases in tropical vegetation are addressed, we expect the magnitude of the land carbon sink to increase and become more in line with observational estimates. As such, LM4.1 provides both an exciting basis for analysis in the context of the ESM4.1 contributions to CMIP6 and a promising mechanistic platform for near-term development as individual fidelity challenges are considered and addressed.

Appendix A: Equations of Energy and Mass Balance

To introduce the notation for this description, we consider a land surface tile where there are N vegetation cohorts that form M layers. Cohorts are numbered from the tallest to the shortest; layers are numbered from top to bottom. Each cohort entirely belongs to a single layer such that the cohorts do not straddle the boundaries between layers. Each cohort k is composed of identical individuals with a spatial density of n_k (1/m2) with each individual plant having a crown area a_k (m^2). Therefore, crowns of all plants that make up cohort k occupy fraction f_k of their layer's area:

$$f_k = n_k a_k (1 - \eta_k) \tag{A1}$$

where η_k is the fraction of internal gaps within plant canopies.

A1. Land Surface Multi-Layer Mass and Energy Balance

Each of the plants exchanges turbulent fluxes of heat and substances with the air in the canopy air space, which also exchanges fluxes with the ground surface and the atmosphere. The canopy air space is well mixed. The time evolution of the canopy air specific humidity q_c is given by (Figure A1)

$$m_c \frac{dq_c}{dt} = \sum_{k=1}^{N} f_k E_{v,k} + E_g - E_a \tag{A2}$$

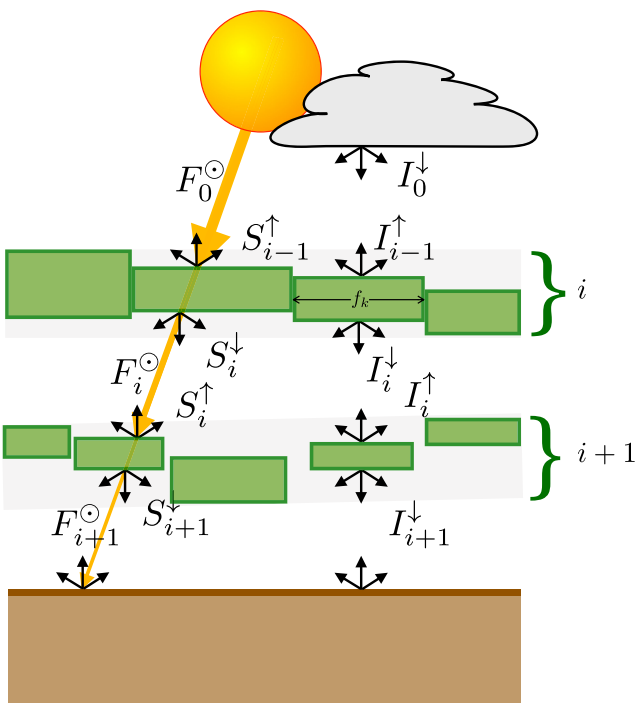

Figure A1. Schematic of multilayer and multicohort radiation propagation through the vegetation canopy in LM4.1. Cohorts are denoted in green and the ground in brown. The canopy can have an arbitrary number of layers, as generated by the Perfect Plasticity Approximation model.

where m_c is the mass of canopy air,

$$E_{v,k} \equiv E_{t,k} + E_{l,k} + E_{s,k} \tag{A3}$$

is the water vapor flux from canopy k, with $E_{t,k}$ being transpiration, $E_{t,k}$ and $E_{t,k}$—water vapor fluxes from intercepted water and snow, respectively. E_g is water vapor flux from the ground surface, and E_a is water vapor flux from canopy air to the atmosphere. Note that the fluxes between canopy and canopy air described in this section (e.g., $E_{t,k}$, $E_{l,k}$, and $E_{s,k}$ in expression A3) are calculated per unit area of the plant crown.

Similarly, the equation of the well-mixed canopy air energy balance is:

$$m_c \frac{d}{dt}\left((1 - q_c) c_p T_c + q_c c_v T_c\right) = \sum_{k=1}^{N} f_k H_{v,k} + H_g - H_a + c_v \left(\sum_{k=1}^{N} f_k T_{v,k} E_{v,k} + T_g E_g - T_c E_c \right) \tag{A4}$$

where c_p and c_v are the heat capacities of dry air and water vapor, T_c is the temperature of canopy air, $T_{v,k}$ is the temperature of cohort k canopy, $H_{v,k}$ is the sensible heat flux from canopy k to the canopy air, H_g and H_a are the sensible heat fluxes from the ground to canopy air and from the canopy air to the atmosphere, respectively.

The mass balance of intercepted liquid water and snow on the canopy of cohort k is affected by the interception of a fraction $\gamma_{I,k}$ of liquid and solid precipitation, water and snow drip $D_{l,k}$, $D_{s,k}$ and evaporation/sublimation $E_{l,k}$, $E_{s,k}$:

$$\frac{dw_{l,k}}{dt} = \gamma_{I,k} P_{l,i} - D_{l,k} - E_{l,k} \tag{A5}$$

$$\frac{dw_{s,k}}{dt} = \gamma_{I,k} P_{s,i} - D_{s,k} - E_{s,k} \tag{A6}$$

$P_{l,i}$ and $P_{s,i}$ are the rates of liquid and solid precipitation falling on top of layer i. At the top of the canopy, $P_{l,1}$ and $P_{s,1}$ are simply the rainfall and snowfall rates from the atmosphere; for the layers below the top,

$$P_{l,i} = P_{l,i-1}\left(1 - \sum_{k \in i-1} f_k \gamma_{I,k}\right) \tag{A7}$$

$$P_{s,i} = P_{s,i-1}\left(1 - \sum_{k \in i-1} f_k \gamma_{I,k}\right) \tag{A8}$$

where the summation is over all cohorts in layer $i-1$, and $\gamma_{I,k}$ is the fraction of incident precipitation that is intercepted by the canopy of cohort k:

$$\gamma_{I,k} = 1 - \exp(-\max(\mathrm{LAI}_k, \mathrm{SAI}_k)) \tag{A9}$$

The model uses a simplifying assumption that the drip from the canopies is not intercepted by the layers below but contributes directly to the water and energy balance of the underlying surface.

Water and snow drip rates from the canopy are proportional to the amount of substances on the canopy, except the cases of extremely intense precipitation, when the amount intercepted by the canopy exceeds the maximum allowed values $W_{l,\,\max} = \mathrm{LAI} \times 0.02$ kg m^{-2} and $W_{s,\,\max} = \mathrm{LAI} \times 0.3$ kg m^{-2}. The expression for drip rates of liquid water and snow:

$$D_{l,k} = \frac{w_{l,k}}{\tau_l} \tag{A10}$$

$$D_{s,k} = \frac{w_{s,k}}{\tau_s} \tag{A11}$$

The characteristic drip time scales for liquid and snow are $\tau_l = 6$ hr and $\tau_s = 3$ days respectively.

The energy balance of the cohort k canopy, in layer i is described with the following equations:

$$\begin{aligned}\frac{d}{dt}(C_{v,k}T_{v,k} + w_{l,k}c_l T_{v,k} + w_{s,k}c_s T_v) &= R_{Sv,k} + R_{Lv,k} - H_{v,k} \\ &- E_{t,k}(L_{e0} + c_v T_{v,k} - c_l T_{u,k}) \\ &- E_{l,k}(L_{e0} + c_v T_{v,k}) \\ &- E_{s,k}(L_{s0} + c_v T_{v,k}) \\ &+ H_{pl,i}\gamma_{I,k} - c_l T_{v,k} D_{l,k} + H_{ps,i}\gamma_{I,k} - c_s T_{v,k} D_{s,k}\end{aligned} \tag{A12}$$

where $T_{v,k}$ is the temperature of the vegetation canopy, $T_{u,k}$ is the average temperature of water taken up by the plant from the soil, $C_{v,k}$ is the heat capacity of the dry vegetation canopy, c_l and c_s are the specific heat capacities of liquid water and snow, $R_{Sv,k}$ and $R_{Lv,k}$ are the net short-wave and long-wave radiative balances of the canopy, $H_{v,k}$ is the sensible heat flux from the canopy to canopy air, L_{e0} and L_{s0} are the latent heats of evaporation and sublimation, $H_{pl,i}$ and $H_{ps,i}$ are the fluxes of sensible heat carried by precipitation entering canopy layer i.

Finally, the energy balance of ground surface is given by:

$$R_{Sg} + R_{Lg} - H_g - L_g E_g - G - L_f M_g = 0 \tag{A13}$$

where R_{Sg} and R_{Lg} are the net short- and long-wave radiative balances of the surface, H_g and $L_g E_g$ are the sensible and latent heat fluxes, G is the ground heat flux (positive down from the surface), and $L_f M_g$ is the latent heat due to surface water melt.

The system of equations (Equations A2–A12), together with the equations of soil energy and water balance (Milly et al., 2014), is linearized with respect to temperature and mass increments around the state variables at the beginning of each time step and solved numerically every physical time step of the model. The numerical solution is implicit, which allows relatively large time steps (e.g., 30 min).

A2. Turbulent Fluxes Between Canopies and Canopy Air

The model uses the following expressions to calculate the fluxes between canopies and canopy air:

$$H_{v,k} = \frac{\rho c_p}{r_{v,k}}(T_{v,k} - T_c) \tag{A14}$$

$$E_{t,k} = \rho \frac{f_{t,k}}{r_{s,k} + r_{v,k}}(q_{i,k} - q_c) \tag{A15}$$

$$E_{l,k} = \rho \frac{f_{l,k}}{r_{v,k}}(q_*(T_{v,k}) - q_c) \tag{A16}$$

$$E_{s,k} = \rho \frac{f_{s,k}}{r_{v,k}}(q_*(T_{v,k}) - q_c) \tag{A17}$$

where $q_{i,k}$ is the specific humidity of air within the leaf (see Appendix A5), and $q_*(T_{v,k})$ is the saturated specific humidity at canopy temperature $T_{v,k}$. $f_{l,k}$ and $f_{s,k}$ are the fractions of the canopy covered by the intercepted liquid and snow, $f_{t,k}$—fraction of the canopy that is not covered by either snow or liquid (and therefore can transpire),

$$f_{s,k} = \left(\frac{w_{s,k}}{W_{s,\max}}\right)^{p_s} \tag{A18}$$

$$f_{l,k} = \left(\frac{w_{l,k}}{W_{l,\max}}\right)^{p_l}(1 - f_{s,k}) \tag{A19}$$

$$f_{t,k} = 1 - f_{l,k} - f_{s,k} \tag{A20}$$

The turbulent fluxes between the ground surface and canopy air are expressed in a similar fashion

$$H_g = \frac{\rho c_p}{r_g}(T_g - T_c) \tag{A21}$$

$$E_g = \rho \frac{1}{r_g}(q_g - q_c) \tag{A22}$$

Near-surface specific humidity q_g is calculated based on the presence of snow and the amount of water available in the upper layer of the soil:

$$q_g = q^*(T_g) \times \begin{cases} \exp\left(g\psi_s/(R_v T_{ref})\right), & \text{for snow-free soil} \\ 1 & \text{for snow-covered soil} \end{cases} \tag{A23}$$

where $q^*(T_g)$ is the saturated water vapor specific humidity at the temperature of the surface interacting with the canopy air (soil surface for snow-free conditions and upper surface of snowpack for the snow-covered soil), $g = 9.81$ m s^{-2} is the acceleration due to gravity, ψ_s (m) is the soil water matric potential at the soil surface, and R_v (J kg^{-1} K^{-1}) is the gas constant for water vapor. $T_{ref} = 293$ K is a reference temperature.

To calculate the quasi-laminar aerodynamic resistances between canopy and canopy air $r_{v,k}$, and between ground and canopy air r_g the model follows (Bonan, 1996) in assuming that the wind speed profile u(z) within the canopy is exponential:

$$u(z) = u(H)\exp\left(-a\frac{H-z}{H}\right) \tag{A24}$$

and the vertical profile of eddy diffusivity $K_h(z)$ (m^2 s^{-1}) is also exponential:

$$K_h(z) = K_h(H)\exp\left(-a\frac{H-z}{H}\right) \tag{A25}$$

where H is the height of the top of the canopy, z is the height from the ground surface, and a is a dimensionless empirical parameter, equal to 3.0 in current model formulation. The model calculates H as the height of the tallest cohort in the tile, imposing a lower limit of 0.1 m.

The formulation of aerodynamic conductance through a leaf boundary layer can be traced through (Bonan, 1996) to (Choudhury & Monteith, 1988), to (H. G. Jones, 1983):

$$g_b(z) = \alpha\sqrt{\frac{u(z)}{d}} \tag{A26}$$

where $\alpha = 0.01$ m s$^{-1/2}$, and d is the characteristic plant surface dimension in the direction of the wind flow, assumed to be equal 4 cm in the model.

The expression (Equation A26) gives the value of quasi-laminar aerodynamic conductance per unit leaf area. To calculate the bulk aerodynamic conductance between the canopy of cohort k and canopy air, the model assumes that the plant surface elements are uniformly distributed between the top and the bottom of the canopy. Integrating in height,

$$g_{v,k} \equiv \frac{1}{r_{v,k}} = \frac{2\alpha H}{a}\sqrt{\frac{u(H)}{d}}\,\frac{\mathrm{SAI}_k + \mathrm{LAI}_k}{H_{t,k} - H_{b,k}}\left[\exp\left(-a\frac{H-H_{b,k}}{2H}\right) - \exp\left(-a\frac{H-H_{t,k}}{2H}\right)\right] \tag{A27}$$

$H_{t,k}$ is the height of the top of cohort k canopy, and $H_{b,k}$ is height of its bottom. To estimate the latter, the model uses the height of the tallest cohort in the next lower layer, or zero if there is no next vegetation layer.

To calculate the resistance between canopy air and ground surface, the model integrates expression (Equation A25) between ground surface roughness length for scalars z_{0s} and $z_1 = d_0 + z_{0m}$ where d_0 is displacement height and z_{0m} is the land surface roughness length for momentum:

$$r_g = \int_{z_{0s}}^{z_1}\frac{1}{K_h(z)}dz = \frac{H}{K_h(H)a}\left[\exp\left(a\frac{H-z_{0s}}{H}\right) - \exp\left(a\frac{H-z_1}{H}\right)\right] \tag{A28}$$

To calculate the value of turbulent diffusion coefficient at the top of the canopy $K_h(H)$, the model uses expression

$$K_h(H) = \kappa u_*(H - d_0) \tag{A29}$$

where κ is von Karman constant, and u_* is the friction velocity calculated by the Monin-Obukhov parameterization of the flux exchange between atmosphere and land surface.

A3. Radiative Balance of Canopies and Land Surface

To calculate the radiative balances of each cohort, the model first obtains the bulk radiative properties of cohorts' canopies by solving the equation of radiation propagation using the two-stream approximation for each cohort, under the assumption of plain-parallel structure of cohort canopies (Meador & Weaver, 1980; Pinty et al., 2006). The model also assumes a spherical angular distribution of leaves, with the optical properties of leaves specified separately for each species (see Table B1).

As a result, the model obtains the optical properties of each cohort k: reflectance for diffuse light α_k, transmittance for diffuse and direct light τ_k and $\tau_k^{\odot}$, and coefficients of upward and downward scattering of direct beam $s_k^{\uparrow}$ and $s_k^{\downarrow}$.

To calculate light propagation through the entire multi-layer mult-cohort vegetation, the properties of the cohorts are combined using their fractional areas within canopy layers, so that the equations of radiation transport become:

$$I_{i-1}^{\uparrow} = \sum_k f_k s_k^{\uparrow} F_{i-1}^{\odot} + \sum_k f_k \alpha_k I_{i-1}^{\downarrow} + \sum_k f_k \tau_k I_i^{\uparrow} \tag{A30}$$

$$I_i^{\downarrow} = \sum_k f_k s_k^{\downarrow} F_{i-1}^{\odot} + \sum_k f_k \alpha_k I_i^{\uparrow} + \sum_k f_k \tau_k I_{i-1}^{\downarrow} \tag{A31}$$

$$F_i^{\odot} = \sum_k f_k \tau_k^{\odot} F_{i-1}^{\odot} \tag{A32}$$

where the summation is performed over all cohorts that belong to layer i. In this notation, $I_i^{\downarrow}$, $I_i^{\uparrow}$, and $F_i^{\odot}$ are the upward and downward fluxes of diffuse radiation and downward direct flux below vegetation layer i. $F_0^{\odot}$ and $I_0^{\downarrow}$ are the inputs of downward direct and diffuse fluxes, respectively, at the top of the entire canopy. To close the system of Equations A30–A32, the flux reflected at the ground surface (below lowest canopy layer M) is

$$I_M^{\uparrow} = \alpha_g^{\odot} F_M^{\odot} + \alpha_g I_M^{\downarrow} \tag{A33}$$

where $\alpha_g^{\odot}$ and α_g are ground surface reflectances for direct and diffuse light. The short-wave radiative balance of the cohort k canopy is then:

$$R_{S,k} = \left(I_{i-1}^{\downarrow} + I_i^{\uparrow}\right)(1 - \alpha_k - \tau_k) + F_{i-1}^{\odot}\left(1 - \tau_k^{\odot} - s_k^{\uparrow} - s_k^{\downarrow}\right) \tag{A34}$$

per unit area of that canopy.

Equations of short-wave radiation balance are solved for two spectral bands (visible and near infrared), and the total radiative balance is calculated as the sum of the two. The long-wave radiation budget of the canopies is calculated similarly, except that there is no contribution from direct solar light, and each of the cohort canopies emits long-wave radiation according to the Stefan-Boltzmann law. Consequently, the individual canopies within the layer interact with the canopies in the layers above and below and with the ground surface (but not with other canopies within the same layer) through long-wave radiation emission and absorption.

A4. Plant Photosynthesis and Respiration

The computation of energy, moisture, and CO_2 exchanges requires knowledge of stomatal and aerodynamic canopy conductances. We assume that the whole cohort has leaf temperature T_l and stomata are saturated and have specific humidity $q(T_l)$. First, we compute stomatal conductance without taking into account any limitation by water availability, $g_{s,\,\max}$. Additionally, stomatal conductance has a vertical distribution $g_s(\mathrm{LAI}')$ ($\mathrm{molH_2Om^{-2}s^{-1}}$), where LAI' ($\mathrm{m^2\ m^{-2}}$) is the cumulative leaf area, measured from the top of the canopy

downward. A system of three equations with three unknowns - the stomatal conductance, $g_{s,\,\max}$, the intercellular concentration of CO_2, C_i (mol mol^{-1}), and the net photosynthesis, A_n (molCO_2 m^{-2} s^{-1}) - defines the plant uptake of CO_2 and the rate of non-water-stressed transpiration for a thin canopy layer dLAI′ at a temperature $T_l(K)$ receiving an incident photosynthetically active radiation flux Q(LAI′) (Einstein m^{-2} s^{-1}) and surrounded by canopy air with vertically uniform specific humidity q_{ca} (kg kg^{-1}) and CO_2 concentration C_{ca} (mol mol^{-1}):

$$g_{s,\max} = \frac{m \cdot A_n}{(C_i - \Gamma_*) \cdot \left(1 + \left(q_{sat}(T_l) - q_{ca}\right)/d_0\right)} \tag{A35}$$

$$A_n = \frac{g_{s,\max}}{1.6} \cdot (C_{ca} - C_i) \tag{A36}$$

for C3:

$$A_n = \min\begin{pmatrix} J_E = a\alpha_3 Q \dfrac{C_i - \Gamma_*}{C_i + 2\Gamma_*} \\ J_C = V_m(T_l) \dfrac{C_i - \Gamma_*}{C_i + K_c(T_l)\dfrac{p_{ref}}{p} \cdot (1 + [\mathrm{O_2}]/K_o(T_l))\dfrac{p_{ref}}{p}} \\ J_j = \dfrac{V_m(T_l)}{2} \end{pmatrix} - \gamma V_m(T_l) \tag{A37}$$

for C4:

$$A_n = \min\begin{pmatrix} J_E = a\alpha_4 Q \\ J_C = V_m(T_l) \\ J_{\mathrm{CO2}} = 18000 V_m(T_l)\, C_l \end{pmatrix} - \gamma V_m(T_l) \tag{A38}$$

where a is the leaf absorptance of photosynthetically active radiation, α_3 and α_4 are the intrinsic quantum efficiencies, V_m is the maximum velocity of carboxylase (molCO_2 m^{-2} s^{-1}), $\Gamma_* = \alpha_{\mathrm{CO2}}[\mathrm{O_2}]K_C/(2K_O)$ is the compensation point, K_C and K_O are the Michaelis-Menten constants for CO_2 and O_2, [O_2] is the atmospheric oxygen concentration, $p_{ref} = 1 \times 10^5$ Pa is the reference pressure and p is an atmospheric pressure. The temperature dependence of the Michaelis-Menten constants, the maximum velocity of carboxylase, and the compensation point are described by the Arrhenius function:

$$f(T) = \exp\left(E_0\left(-\frac{1}{258.16} - \frac{1}{T}\right)\right) \tag{A39}$$

where T is the temperature (Kelvin) and E_0 is a temperature sensitivity factor (Foley et al., 1996) (see Table B1 for parameter values).

Equation A35 gives the leaf stomatal conductance for vegetation if the soil water is not limiting. It links the rate of stomatal conductance for water gs to the net photosynthesis (A_n), intercellular concentration of CO_2 (C_i), and humidity deficit between intercellular space and the external environment. This equation is a simplification of Leuning (1995) empirical relationship assuming that the contribution of cuticular conductance is negligible. Equation A36 is a one-dimensional gas diffusion law. The factor of 1.6 is the ratio of diffusivities for water vapor and CO_2. We assume that the diffusion of CO_2 is mostly limited by stomatal conductance and not by leaf boundary layer conductance. Equations A37 and A38 are based on the mechanistic model of photosynthesis by Farquhar et al. (1980) and its extensions by Collatz et al. (1991, 1992).

The net photosynthesis is the difference between the gross photosynthesis and leaf respiration. The gross photosynthesis for C3 plants is the minimum of three limited rates: the light limited rate J_E, the Rubisco limited rate J_C, and the export limited rate of carboxylation J_j. Similarly, in Collatz et al. (1992) the gross photosynthesis rate for C4 plants is the minimum of the light limited rate J_E, the Rubisco limited rate J_C, and the CO_2 limited rate

J_{CO2}. Leaf respiration is computed as $R_{leaf} = \gamma V_m m(T_l)$. Although the formulation of Collatz et al. (1991) is widely used in dynamic vegetation and land surface models, it requires computationally expensive iterative solutions. The simplifying assumption made in Equation A35 that cuticular conductance is negligible, allows an analytical solution for the three unknowns.

Assuming that a PAR flux $Q(\mathrm{LAI}')$ monotonically decreases through the C3 canopy, the PAR flux $Q(\mathrm{LAI}_{eq})$ can be defined at the level L_{eq}, at which the light limited rate J_E is equal to the minimum of the Rubisco limited rate J_C and the export-limited rate of carboxylation J_j. Above the canopy level L_{eq} the gross photosynthesis will be a function of the Rubisco or export limited rate and below this level the gross photosynthesis will be a function of the light limited rate, so that average canopy net photosynthesis and average canopy stomatal conductance are:

$$\overline{A}_n = \frac{\min(J_c, J_j) \cdot \mathrm{LAI}_{eq} + \int_{\mathrm{LAI}_{eq}}^{\mathrm{LAI}} J_E\left(\mathrm{LAI}'\right) d\mathrm{LAI}'}{\mathrm{LAI}} \tag{A40}$$

$$\overline{g}_{s,\max} = \frac{m \cdot \overline{A}_n}{(C_i - \Gamma_*) \cdot \left(1 + \left(q_{sat}(T_l) - q_{ca}\right)/d_0\right)} \tag{A41}$$

Average net photosynthesis for C4 plants is computed in a similar fashion. Gross primary production is computed as a sum of an average canopy photosynthesis $\overline{A}_n$ and leaf respiration R_{leaf}.

A5. Plant Hydraulics and Water Limitations on Stomatal Conductance

Calculation of the water availability effect on transpiration and stomatal conductance follows the approach based on Wolf et al. (2016). To calculate plant transpiration, the model assumes that there is no water storage in the trunk, but the water conductance through the plant depends on plant size, cross-section of conducting tissues, and water stress within the tissues. We define Ψ_l as the water potential of the leaf (at the point of vaporization), Ψ_x as the water potential at the interface between the leaf and plant xylem (i.e., at the leaf attachment pint to the stem), and Ψ_r as the water potential at the interface between the root system and the stem. We assume no resistance inside the root system other than resistance of soil in the rhizosphere and resistance of the root skin. This simplification means that all effects of xylem resistance are conceptually assigned to the plant stem.

Since the model assumes no water storage in the plant, the mass conservation equation is:

$$u_r = u_x = u_l = E_t \tag{A42}$$

where u_r is flux of water out of the root system, u_x is the flux through the xylem, u_l is the flux through the leaves of the individual, and E_t is individual's transpiration. Flux of water through the stem xylem at any given height z is described by the Darcy (1856) law:

$$u_x = -K_x(\psi)\frac{d\psi}{dz} \tag{A43}$$

where stem conductance of individual follows Sperry et al. (1998) formulation:

$$K_x(\psi) = a_x k_x \exp\left[-\left(\frac{\psi}{d_x}\right)^{c_x}\right] \tag{A44}$$

k_x is a species-dependent xylem conductance per unit area of xylem cross-section (kg m^{-1} Pa^{-1} s^{-1}), a_x is the area of the xylem cross-section (m^2), c_x and d_x (which is negative) are species-dependent parameters describing the xylem conductance dependence on water stress. For simplicity, Equation A43 neglects the gravitational potential of the water.

To find the flow through the xylem given the boundary conditions Ψ_r and Ψ_l, we integrate both sides of Equation A43 by z, taking into account that since we assume no water storage in the xylem, u_x does not depend on z:

$$u_x = \frac{a_x k_x}{H}\frac{d_x}{c_x}\left[\Gamma\left(\frac{1}{c_x},\left(\frac{\Psi_x}{d_x}\right)^{c_x}\right) - \Gamma\left(\frac{1}{c_x},\left(\frac{\Psi_r}{d_x}\right)^{c_x}\right)\right] \tag{A45}$$

where $\Gamma(s, x)$ is upper incomplete gamma function, and H is the height of the leaf attachment point (height of the canopy).

Similarly, water flux within a leaf is given as:

$$u_l = -K_l(\psi)\frac{d\psi}{dx} \tag{A46}$$

where x is the distance within the leaf from the point where it attaches to the branch. The expression for leaf conductance is similar to the xylem conductance:

$$K_l(\psi) = a_l k_l \exp\left[-\left(\frac{\psi}{d_l}\right)^{c_l}\right] \tag{A47}$$

Similar to Equation A45, flow through the leaves can be also expressed in terms of boundary water potentials Ψ_x and Ψ_l, without explicitly representing in-leaf distribution of water potentials:

$$u_l = A_l k_l \frac{d_l}{c_l}\left[\Gamma\left(\frac{1}{c_l},\left(\frac{\Psi_l}{d_l}\right)^{c_l}\right) - \Gamma\left(\frac{1}{c_l},\left(\frac{\Psi_x}{d_l}\right)^{c_l}\right)\right] \tag{A48}$$

where A_l is the plant leaf area.

Following (Wolf et al., 2016), the scaling factor for non-water-limited stomatal conductance is

$$\phi_s(\Psi_l) = \exp\left[-\left(\frac{\Psi_l}{d_l}\right)^{c_l}\right] \tag{A49}$$

so that the water-limited stomatal conductance is:

$$g_s(\Psi_l) = \overline{g}_{s,\max} A_l \exp\left[-\left(\frac{\Psi_l}{d_l}\right)^{c_l}\right] \tag{A50}$$

The factor A_l scales the average stomatal conductance per unit leaf area $\overline{g}_{s,\max}$ to the plant level.

At the point of vaporization, the water potential Ψ_l is equal to water potential of air within a leaf:

$$\Psi_l = \Psi_{air,i} = \frac{RT_l}{V_m}\ln(\mathrm{RH}_i) \tag{A51}$$

or, equivalently

$$q_i = q_*(T_l)\exp\left(\frac{\Psi_l \mu_w}{RT_l}\right) \tag{A52}$$

where $R = 8.31$ J/mol/K is the universal gas constant, $\mu_w = 18 \times 10^{-6}$ m^3 mol^{-1} is partial molar volume of liquid water, RH_i is relative humidity inside the leaf, and $q_*(T_l)$ is the saturated specific humidity at temperature T_l and ambient pressure.

Solving the above system of equations, together with Equation A15 scaled to the plant level allows us to jointly determine plant stomatal conductance and its transpiration.

Formulation of water uptake by roots is based on the Darcy (1856) law of soil water conductance. Let u be the rate of water uptake per unit length of fine root, r_r—the fine root radius, and r—the "microscopic" distance from the root axis. For steady flow toward the root,

$$u = 2\pi r K(\psi)\frac{d\psi}{dr} \tag{A53}$$

where $K(\psi)$ is the unsaturated hydraulic conductivity of the soil, and ψ is the soil matric water potential. Integrating from root-soil interface to "bulk" soil (with matric head ψ_s at the distance R_s from the root axis):

$$\int_{r_r}^{R_s}\frac{u}{2\pi r}dr = \int_{\psi_r}^{\psi_s}K(\psi)d\psi \tag{A54}$$

or, equivalently:

$$u = \frac{2\pi}{\ln(R_s/r_r)}\int_{\psi_r}^{\psi_s}K(\psi)d\psi \tag{A55}$$

This relationship is assumed to hold at a macroscopic point, that is a model layer in this case. To find the characteristic distance R_s to the "bulk soil" with matric potential ψ_s, we assume it to be equal to the half-distance between roots. At each soil horizon, it can be expressed in terms of a cohort's specific root length λ_k (SRL, length of fine roots per unit mass of carbon) and the volumetric density of root biomass of each cohort, $b_{r,k}(z)$. The total length of roots per unit volume is:

$$L_r(z) = \sum_k n_k\lambda_k b_{r,k}(z) \tag{A56}$$

Therefore, the area of cross-section surrounding the root $A_r = 1/L_r$ giving:

$$R_s = \frac{1}{\sqrt{\pi L_r}} \tag{A57}$$

On the other hand, the water flux through the root skin per unit length of the root is:

$$u = 2\pi r_r K_r(\psi_r - \psi_x) \tag{A58}$$

The vertical distribution of plant fine root biomass is assumed to be exponential (Jackson et al., 1996), with $e-$folding depth ζ:

$$b_{r,k}(z) = \frac{B_{r,k}}{\zeta_k}\exp\left(\frac{z}{\zeta}\right) \tag{A59}$$

where $B_{r,k}$ is the total fine root biomass of a plant.

Solving Equations A55 and A58 gives the resulting water uptake per unit length of root for each cohort, and, after appropriate scaling, the total water uptake of the plant. This plant uptake is in turn used to solve the plant hydraulics equation and obtain the total evapotranspiration, water potentials, and stomatal conductance of the plant. The solution is performed numerically, using linearization around the state at the previous time step.

A6. Plant Allometry and Carbon Allocation

Plant allometry and carbon allocation are based on the parameterizations described in LM3PPA-TV (Martínez Cano et al., 2020), which is an updated version of the first implementation of the PPA dynamics in GFDL LM3.0 version, LM3-PPA model (Weng et al., 2015). LM4.1 represents tree and grass biomass as six dynamic carbon pools: leaves (L), fine roots (FR), reproductive pools (F), labile nonstructural carbohydrates (NSC), sapwood (SW) and heartwood (HW). The crown area of each plant or grass tussock is A_C is described as:

$$A_C = a_C D^{b_C} \tag{A60}$$

where a_C and b_C are parameters determining the shape of the crown and D is the plant or tussock diameter. The plant height $H(D)$ is defined as a saturating function of trunk diameter using a generalized Michaelis-Menten function following Martínez Cano et al. (2020):

$$H(D) = \frac{a_H D^{b_H}}{k_H + D^{b_H}} \tag{A61}$$

where a_H is the asymptotic tree height, and b_H and k_H determine the rate of tree height increase with diameter. This form of height function avoids accelerating the rate of tree height growth with trunk diameter. Changes in the plant biomass $B_w(D)$ is then represented as:

$$B_W(D) = \alpha_{BM} \rho D^2 H \tag{A62}$$

where ρ is the wood density.

The plants' pools are defined by the following relationships. The allocation of new carbon to each pool depends on the instantaneous deviation between the biomass of each pool and its target. Similarly to Weng et al. (2015), we define the following targets for the biomass of leaves L^*, fine roots FR^*, nonstructural carbohydrates NSC^*, branches BR^*, and sapwood BSW^*:

Similarly to LM3, the leaf and fine root biomass target equations follow the pipe model (Shinozaki et al., 1964). Target leaf biomass L^* is the product of the leaf mass per area, LMA, and the target total leaf area, A_L^*, which is defined as a product of crown leaf area index LAI^*, crown area A_C, corrected for the fraction of internal canopy gaps $1 - \eta$. The canopy and understory canopy layers have different target values LAI^*. The fine root target biomass FR^* is the product of the specific root area SRA and the total root area target A_R^*, which is computed as the root surface area per leaf area ϕ_{RL} times the target total leaf area, A_L^*. The target nonstructural carbohydrates NSC^* is proportional to leaf biomass L^*, with proportionality constant q_{NSC}. The target branch biomass BR^* is a constant fraction p_{BR} of wood biomass $B_w(D)$. The target sapwood biomass is computed as a difference with heartwood biomass, defined in terms of an equivalent diameter of heartwood. Conversion of biomass from sapwood to heartwood follows Weng et al. (2015) and Martínez Cano et al. (2020).

Leaf biomass:

$$L^* = LMA \times A_L^* = LMA \times LAI^*(1 - \eta)A_C \tag{A63}$$

fine root biomass:

$$FR^* = \frac{A_R^*}{SRA} = \frac{\phi_{RL} A_L^*}{SRA} \tag{A64}$$

biomass of nonstructural carbohydrates

$$NSC^* = q_{NSC} L^* \tag{A65}$$

branch biomass

$$BR^* = p_{BR} B_W = p_{BR} \alpha_{BM} \rho D^2 H \tag{A66}$$

sapwood biomass

$$B_{SW}^* = \alpha_{BM} \rho \left(D^2 - {D_{HW}^*}^2 \right) H \tag{A67}$$

Appendix B: Model Parameters for Different Vegetation Types in the Equations Presented in Appendix A

Table B1 shows the model parameters for different vegetation types.

Table B1
Model Parameters for Different Vegetation Types in the Equations Presented in Appendix A

	Tropical tree	Evergreen coniferous	Temperate tree	C4 grass	C3 grass
η, internal gap fraction	0.1	0.1	0.1	0.1	0.1
λ_l, length of fine roots per unit mass of carbon, m (kg C)$^{-1}$	43.9×10^3	43.9×10^3	43.9×10^3	112.0×10^3	150.0×10^3
m, stomatal conductance factor	7.0	7.0	7.0	4.0	7.0
V_m, maximum Rubisco-limited carboxylation rate mol CO_2 m^2 s^{-1}	3.0×10^{-5}	2.1×10^{-5}	2.0×10^{-5}	1.0×10^{-5}	2.0×10^{-5}
γ, leaf respiration factor	1.0×10^{-2}	3.0×10^{-2}	3.5×10^{-2}	3×10^{-2}	1.5×10^{-2}
d_0, reference value of canopy air water vapor deficit, kg H_2O (kg air)$^{-1}$	0.09	0.09	0.09	0.09	0.09
α, photosynthetic quantum yield, mol CO_2 Einstein^{-1}	0.04	0.04	0.04	0.03	0.06
$[O_2]$ intercellular concentration of oxygen, mol O_2 (mol air)$^{-1}$	0.209	0.209	0.209	0.209	0.209
a_H, asymptotic height, m	60.98	29.83	49.12	1.41	1.41
b_H, exponent of tree height allometry	0.863	1.452	0.759	2.611	2.611
k_H, inflection parameter of tree height allometry	0.684	0.110	0.531	1.410×10^{-3}	1.410×10^{-3}
a_C, intercept of crown area allometry	243.78	111.06	150.0	95.0	95.0
b_C, scaling parameter of crown area allometry	1.182	1.580	1.5	1.5	1.5
a_{BM}, biomass allometry parameter	0.559	0.414	0.368	1.0	1.0
LMA, leaf mass per unit area, kg C m^{-2}	3.5×10^{-2}	0.1	3.8×10^{-2}	2.655×10^{-2}	2.655×10^{-2}
ρ, wood density, kg C m^{-3}	215.95	185.0	245.0	69.4	69.4
LAI*, target crown leaf area index	6.0	5.0	3.5	2.5	2.5
Understory LAI factor	0.25	0.25	0.25	0.25	0.25
ϕ_{RL}, ratio of root surface area to leaf area	1.4	1.4	0.8	0.8	0.8
SRA, specific fine root area, m^2 (kg C)$^{-1}$	33.1	33.1	33.1	84.45	113.1
q_{NSC}, proportionality constant of NSC target to leaf biomass	4	4	4	4	4
k_l, leaf conductance per unit area kg m^{-2} s^{-1} MPa^{-1}	3×10^{-7}	3×10^{-7}	3×10^{-7}	3×10^{-7}	3×10^{-7}
d_l, leaf conductance dependence on water stress	-3×10^6	-3×10^6	-3×10^6	-3×10^6	-3×10^6
c_l, leaf conductance dependence on water stress	1.5	1.5	1.5	1.5	1.5
k_x, xylem conductance kg m^{-2} s^{-1} MPa^{-1}	3×10^{-6}	3×10^{-6}	3×10^{-6}	3×10^{-6}	3×10^{-6}
d_x, xylem conductance dependence on water stress	-3×10^6	-3×10^6	-3×10^6	-3×10^6	-3×10^6
c_x, xylem conductance dependence on water stress	1.5	1.5	1.5	1.5	1.5
$\alpha_{leaf,VIS}$, leaf reflectance in VIS band	0.1	0.1	0.1	0.11	0.11
$\alpha_{leaf,NIR}$, leaf reflectance in NIR band	0.45	0.39	0.45	0.45	0.45
$\tau_{leaf,VIS}$ leaf transmittance in VIS band	5×10^{-2}	5×10^{-2}	5×10^{-2}	5×10^{-2}	5×10^{-2}
$\tau_{leaf,NIR}$, leaf transmittance in NIR band	0.25	0.25	0.25	0.25	0.25
p_{BR}, proportionality constant for branchwood target	0.1525	0.2065217	0.2065217	0.0	0.0
ζ_k, e-folding depth parameter	0.25813	0.25813	0.25813	0.35212	0.17039

Appendix C: Soil Carbon Dynamics Model

The soil carbon dynamics model used in this study follows Sulman et al. (2014) paper, except few changes that were motivated by the need for the soil carbon state to reach a steady state—which is essential for the formulation to be useable in the framework of ESM.

First, in this configuration of the model the carbon isotope tracking was not enabled, so for simplicity in the equations below we omit the isotope index j that was present in original Sulman et al. (2014) manuscript.

Second, the accumulation of soil carbon in protected pools was disabled. Therefore, equation 1 of Sulman et al. (2014) Supplementary Information (SI) was in effect replaced with a simplified form, that excluded the protected carbon from consideration:

$$\frac{dC_i}{dt} = T_i - D_i \tag{C1}$$

where i indicates chemical class, C is unprotected carbon, T represents carbon transfers between pools such as inputs or litter deposition, and D is decomposition rate for this chemical class. This change effectively excludes Equations 6 and 7 of Sulman et al. (2014) SI that describe protected pool accumulation and decomposition from the model formulation.

Third, we imposed the minimum decomposition rates on all carbon chemical classes:

$$D_i = \max\left[\frac{1}{\tau_{\max}}, V_{\max,i}(T)\left(\frac{\theta}{\theta_{sat}}\right)^3\left(1-\frac{\theta}{\theta_{sat}}\right)^{2.5} C_i \frac{\frac{M}{\sum_i C_i}}{\frac{M}{\sum_i C_i} + k_M}\right] \tag{C2}$$

In the equation above, the second term in the square brackets is identical to Sulman et al. (2014) original formulation, while the first term imposes the upper limit on the time scale of carbon decomposition. In the simulations discussed in this manuscript, the value of $\tau_{\max}$ was set to 500 years.

Appendix D: The Turc-Mezentsev-Priestley-Taylor (TMPT) Model

The Turc-Mezentsev equation (Lebecherel et al., 2013) relates the evapotranspiration ratio (evapotranspiration divided by precipitation) to the dryness index (ratio of potential evapotranspiration to precipitation),

$$\frac{E}{P} = \left[1 + (E_p/P)^{-\nu}\right]^{-1/\nu} \tag{D1}$$

in which ν is commonly taken as 2, yielding a relation very close to that of Budyko (1974). To quantify E_p, we use the Priestley-Taylor equation for evapotranspiration from a non-water-stressed surface under conditions of minimal advection (Priestley & Taylor, 1972),

$$E_p = \frac{\alpha\Delta(R_n - G)}{\Delta + \gamma} \tag{D2}$$

in which α is commonly in the range 1–1.3. Here, Δ is the slope of the saturation vapor pressure curve of water (a function of temperature), γ is the psychrometric constant (a function of pressure), R_n is surface net radiation, and G is the heat flux into the ground. To estimate annual E_p, we apply the Priestley-Taylor equation at a monthly time scale, ignoring G, and then sum monthly values up to the annual scale.

In the application of the TMPT model, we used only data for locations in which the observation-based estimates of precipitation, runoff, and evapotranspiration balanced to within 10% of precipitation. The balance discrepancy is shown in the figure below, where locations exceeding the 10% criterion have been masked out.

Appendix E: Decomposition of GPP Trend Into Components

For each grid cell and each water year, the time-varying GPP, $G(t)$, is represented as the sum over land uses of the product of the land-use area, a_{LU}, and the GPP per unit area of land use within the cell, $G_{LU}(t)$. The area of each land use is represented as the sum of the time mean area, $\overline{a_{LU}}$, and the deviations therefrom, $\delta a_{LU}(t)$. Thus,

$$G(t) = \sum_{LU}\left[\overline{a_{LU}} + \delta a_{LU}(t)\right] G_{LU}(t) \tag{E1}$$

The three land-use categories used are natural and secondary vegetation, pasture and rangeland, and cropland. The dependence of $G_{LU}(t)$ on climate and atmospheric CO_2 is approximated by the use of multiple linear regression,

$$G_{LU}(t) = G_{LU0} + \alpha_{LU}\delta P(t) + \beta_{LU}\delta T_{LU}(t) + \gamma_{LU}\delta C(t) + \epsilon\delta S(t) \tag{E2}$$

The sum over land uses of the product of $\overline{a_{LU}}$ and G_{LU0} is the constant part of $G(t)$. The contribution of changing land use to the temporal variation of $G_LU(t)$ can be estimated as the product of $\delta a_{LU}(t)$ and G_{LU0}. The contribution

from precipitation can be estimated by $\sum_{LU}\overline{a_{LU}}\alpha_{LU}\delta P(t)$ and the contributions from temperature, downward shortwave radiation, and CO_2 can be estimated in a similar fashion. Interactions between changing land use and changing climate and CO_2 are represented by the sums of products of the deviation terms.

Appendix F: Köppen Climate Zones

Table F1 lists the abbreviated names of Köppen Climate Zones used in Figure 3 legend.

Table F1
Köppen Climate Zone Legend

Code	Köppen climate zone
Af	Tropical rainforest
Am	Tropical monsoon
Aw	Tropical wet and dry
BWh	Hot desert
BWk	Cold desert
BSh	Hot semi-arid
BSk	Cold semi-arid
Csa	Hot-summer Mediterranean
Csb	Warm-summer Mediterranean
Csc	Cold-summer Mediterranean
Cwa	Hot-summer temperate monsoon
Cwb	Warm-summer temperate monsoon
Cwc	Cold-summer temperate monsoon
Cfa	Humid Subtropical
Cfb	Oceanic
Cfc	Subpolar oceanic
Dsa	Hot-summer Mediterranean continental
Dsb	Warm-summer Mediterranean continental
Dsc	Mediterranean subarctic
Dsd	Severe-winter Mediterranean subarctic
Dwa	Hot-summer continental monsoon
Dwb	Warm-summer continental monsoon
Dwc	Subarctic monsoon
Dwd	Severe-winter subarctic monsoon
Dfa	Hot-summer humid continental
Dfb	Warm-summer humid continental
Dfc	Subarctic
Dfd	Severe-winter subarctic
ET	Tundra
EF	Polar

Data Availability Statement

ESM4.1 data and model code are provided online at Krasting et al. (2018, https://doi.org/10.22033/ESGF/CMIP6.1407 and http://doi.org/10.5281/zenodo.3836405, respectively). ESM2G (Dunne et al., 2012, 2013) data can be found on ESGF Data Portal CMIP5 section (https://esgf-node.llnl.gov/search/cmip5/).

Acknowledgments
We thank GFDL's Modeling Systems and Operations for keeping LM4.1 development and implementation going through many technical challenges. We appreciate the graphics support provided by Cathy Raphael. This manuscript benefited from the comments and suggestions by the two anonymous reviewers.

References

Adcroft, A., Anderson, W., Balaji, V., Blanton, C., Bushuk, M., Dufour, C. O., et al. (2019). The GFDL global ocean and sea ice model OM4.0: Model description and simulation features. *Journal of Advances in Modeling Earth Systems*, *11*(10), 3167–3211. https://doi.org/10.1029/2019ms001726

Anav, A., Friedlingstein, P., Beer, C., Ciais, P., Harper, A., Jones, C., et al. (2015). Spatiotemporal patterns of terrestrial gross primary production: A review. *Reviews of Geophysics*, *53*(3), 785–818. https://doi.org/10.1002/2015rg000483

Arvor, D., Dubreuil, V., Ronchail, J., Simões, M., & Funatsu, B. M. (2013). Spatial patterns of rainfall regimes related to levels of double cropping agriculture systems in Mato Grosso (Brazil). *International Journal of Climatology*, *34*(8), 2622–2633. https://doi.org/10.1002/joc.3863

Avitabile, V., Herold, M., Heuvelink, G. B. M., Lewis, S. L., Phillips, O. L., Asner, G. P., et al. (2016). An integrated pan-tropical biomass map using multiple reference datasets. *Global Change Biology*, *22*(4), 1406–1420. https://doi.org/10.1111/gcb.13139

Balsamo, G., Beljaars, A., Scipal, K., Viterbo, P., van den Hurk, B., Hirschi, M., & Betts, A. K. (2009). A revised hydrology for the ECMWF model: Verification from field site to terrestrial water storage and impact in the integrated forecast system. *Journal of Hydrometeorology*, *10*(3), 623–643. https://doi.org/10.1175/2008jhm1068.1

Beck, H. E., Zimmermann, N. E., McVicar, T. R., Vergopolan, N., Berg, A., & Wood, E. F. (2018). Present and future Köppen-Geiger climate classification maps at 1-km resolution. *Scientific Data*, *5*(1), 180214. https://doi.org/10.1038/sdata.2018.214

Beer, C., Reichstein, M., Tomelleri, E., Ciais, P., Jung, M., Carvalhais, N., et al. (2010). Terrestrial gross carbon dioxide uptake: Global distribution and covariation with climate. *Science*, *329*(5993), 834–838. https://doi.org/10.1126/science.1184984

Berg, A., & Sheffield, J. (2019). Evapotranspiration partitioning in CMIP5 models: Uncertainties and future projections. *Journal of Climate*, *32*(10), 2653–2671. https://doi.org/10.1175/jcli-d-18-0583.1

Beven, K., & Germann, P. (1982). Macropores and water flow in soils. *Water Resources Research*, *18*(5), 1311–1325. https://doi.org/10.1029/wr018i005p01311

Bonan, G. B. (1996). *A Land Surface Model (LSM version 1.0) for ecological, hydrological, and atmospheric studies: Technical description and user's guide* (Technical Note Nos. NCAR/TN-417+STR). NCAR. https://doi.org/10.5065/D6DF6P5X

Broecker, W. S., Takahashi, T., Simpson, H. J., & Peng, T. H. (1979). Fate of fossil fuel carbon dioxide and the global carbon budget. *Science*, *206*(4417), 409–418. https://doi.org/10.1126/science.206.4417.409

Brown, J., Ferrians, O. J., Jr., Heginbottom, J. A., & Melnikov, E. S. (2002). *Circum-arctic map of permafrost and ground-ice conditions, version 2.0*. NSIDC: National Snow and Ice Data Center. Retrieved from http://nsidc.org/data/ggd318

Brown, R. J. E. (1960). The distribution of permafrost and its relation to air temperature in Canada and the USSR. *Arctic*, *13*(3), 163–177. https://doi.org/10.14430/arctic3697

Budyko, M. I. (1974). *Climate and life*. Academic Press.

Campbell, J. E., Berry, J. A., Seibt, U., Smith, S. J., Montzka, S. A., Launois, T., et al. (2017). Large historical growth in global terrestrial gross primary production. *Nature*, *544*(7648), 84–87. https://doi.org/10.1038/nature22030

Chaney, N. W., Van Huijgevoort, M. H. J., Shevliakova, E., Malyshev, S., Milly, P. C. D., Gauthier, P. P. G., & Sulman, B. N. (2018). Harnessing big data to rethink land heterogeneity in Earth System Models. *Hydrology and Earth System Sciences*, *22*(6), 3311–3330. https://doi.org/10.5194/hess-22-3311-2018

Chapin, III, F. S., Woodwell, G. M., Randerson, J. T., Rastetter, E. B., Lovett, G. M., Baldocchi, D. D., et al. (2006). Reconciling carbon-cycle concepts, terminology, and methods. *Ecosystems*, *9*(7), 1041–1050. https://doi.org/10.1007/s10021-005-0105-7

Cheng, L., Zhang, L., Wang, Y.-P., Canadell, J. G., Chiew, F. H. S., Beringer, J., et al. (2017). Recent increases in terrestrial carbon uptake at little cost to the water cycle. *Nature Communications*, *8*(1), 110. https://doi.org/10.1038/s41467-017-00114-5

Cheruy, F., Ducharne, A., Hourdin, F., Musat, I., Vignon, É., Gastineau, G., et al. (2020). Improved near-surface continental climate in IPSL-CM6A-LR by combined evolutions of atmospheric and land surface physics. *Journal of Advances in Modeling Earth Systems*, *12*(10). e2019MS002005. https://doi.org/10.1029/2019ms002005

Choudhury, B. J., & Monteith, J. L. (1988). A four-layer model for the heat budget of homogeneous land surfaces. *Quarterly Journal of the Royal Meteorological Society*, *114*(480), 373–398. https://doi.org/10.1002/qj.49711448006

Collatz, G., Ball, J., Grivet, C., & Berry, J. A. (1991). Physiological and environmental regulation of stomatal conductance, photosynthesis and transpiration: A model that includes a laminar boundary layer. *Agricultural and Forest Meteorology*, *54*(2–4), 107–136. https://doi.org/10.1016/0168-1923(91)90002-8

Collatz, G., Ribas-Carbo, M., & Berry, J. (1992). Coupled photosynthesis-stomatal conductance model for leaves of C4 plants. *Functional Plant Biology*, *19*(5), 519. https://doi.org/10.1071/pp9920519

Collins, W. J., Lamarque, J.-F., Schulz, M., Boucher, O., Eyring, V., Hegglin, M. I., et al. (2017). AerChemMIP: Quantifying the effects of chemistry and aerosols in CMIP6. *Geoscientific Model Development*, *10*(2), 585–607. https://doi.org/10.5194/gmd-10-585-2017

Cox, P. M., Betts, R. A., Jones, C. D., Spall, S. A., & Totterdell, I. J. (2000). Acceleration of global warming due to carbon-cycle feedbacks in a coupled climate model. *Nature*, *408*(6809), 184–187. https://doi.org/10.1038/35041539

Darcy, H. (1856). *Les fontaines publiques de la ville de dijon: Exposition et application des principes à suivre et des formules à employer dans les questions de distribution d'eau: Ouvrage terminé par un appendice relatif aux fournitures d'eau de plusieurs villes au filtrage des eaux et à la fabrication des tuyaux de fonte, de plomb, de tole et de bitume*. Dalmont.

Das, N. N., Entekhabi, D., Dunbar, R. S., Chaubell, M. J., Colliander, A., Yueh, S., et al. (2019). The SMAP and Copernicus Sentinel 1A/B microwave active-passive high resolution surface soil moisture product. *Remote Sensing of Environment*, *233*, 111380. https://doi.org/10.1016/j.rse.2019.111380

Defries, R. S., & Townshend, J. R. G. (1994). NDVI-derived land cover classifications at a global scale. *International Journal of Remote Sensing*, *15*(17), 3567–3586. https://doi.org/10.1080/01431169408954345

Delworth, T. L., Cooke, W. F., Adcroft, A., Bushuk, M., Chen, J., Dunne, K. A., et al. (2020). SPEAR: The next generation GFDL modeling system for seasonal to multidecadal prediction and projection. *Journal of Advances in Modeling Earth Systems*, *12*(3), e2019MS001895. https://doi.org/10.1029/2019ms001895

Detto, M., Levine, J. M., & Pacala, S. W. (2022). Maintenance of high diversity in mechanistic forest dynamics models of competition for light. *Ecological Monographs*, *92*(2), e1500. https://doi.org/10.1002/ecm.1500

Donner, L. J., Wyman, B. L., Hemler, R. S., Horowitz, L. W., Ming, Y., Zhao, M., et al. (2011). The dynamical core, physical parameterizations, and basic simulation characteristics of the atmospheric component AM3 of the GFDL global coupled model CM3. *Journal of Climate*, *24*, 3484–3519. https://doi.org/10.1175/2011JCLI3955.1

Döscher, R., Acosta, M., Alessandri, A., Anthoni, P., Arsouze, T., Bergman, T., et al. (2022). The EC-Earth3 Earth System Model for the Coupled Model Intercomparison Project 6. *Geoscientific Model Development*, *15*(7), 2973–3020. https://doi.org/10.5194/gmd-15-2973-2022

Dunne, J. P., Horowitz, L. W., Adcroft, A. J., Ginoux, P., Held, I. M., John, J. G., et al. (2020a). The GFDL Earth System Model version 4.1 (GFDL-ESM 4.1): Overall coupled model description and simulation characteristics. *Journal of Advances in Modeling Earth Systems*, *12*(11), e2019MS002015. https://doi.org/10.1029/2019ms002015

Dunne, J. P., Horowitz, L. W., Adcroft, A., Ginoux, P., Held, I. M., John, J., et al. (2020b). NOAA-GFDL/ESM4: GFDL Earth System Model 4 [Software]. Zenodo. https://doi.org/10.5281/zenodo.3836405

Dunne, J. P., John, J. G., Adcroft, A. J., Griffies, S. M., Hallberg, R. W., Shevliakova, E., et al. (2012). GFDL's ESM2 global coupled climate–carbon Earth System Models. Part I: Physical formulation and baseline simulation characteristics. *Journal of Climate*, *25*(19), 6646–6665. https://doi.org/10.1175/jcli-d-11-00560.1

Dunne, J. P., John, J. G., Shevliakova, E., Stouffer, R. J., Krasting, J. P., Malyshev, S. L., et al. (2013). GFDL's ESM2 global coupled climate–carbon Earth System Models. Part II: Carbon system formulation and baseline simulation characteristics. *Journal of Climate*, *26*(7), 2247–2267. https://doi.org/10.1175/jcli-d-12-00150.1

Erb, K.-H., Kastner, T., Plutzar, C., Bais, A. L. S., Carvalhais, N., Fetzel, T., et al. (2017). Unexpectedly large impact of forest management and grazing on global vegetation biomass. *Nature*, *553*(7686), 73–76. https://doi.org/10.1038/nature25138

Evans, S., Ginoux, P., Malyshev, S., & Shevliakova, E. (2016). Climate-vegetation interaction and amplification of Australian dust variability. *Geophysical Research Letters*, *43*(22), 11823–11830. https://doi.org/10.1002/2016gl071016

Evans, S., Malyshev, S., Ginoux, P., & Shevliakova, E. (2019). The impacts of the dust radiative effect on vegetation growth in the Sahel. *Global Biogeochemical Cycles*, *33*(12), 1582–1593. https://doi.org/10.1029/2018gb006128

Eyring, V., Bony, S., Meehl, G. A., Senior, C. A., Stevens, B., Stouffer, R. J., & Taylor, K. E. (2016). Overview of the Coupled Model Intercomparison Project phase 6 (CMIP6) experimental design and organization. *Geoscientific Model Development*, *9*(5), 1937–1958. https://doi.org/10.5194/gmd-9-1937-2016

Fang, H., Baret, F., Plummer, S., & Schaepman-Strub, G. (2019). An overview of global leaf area index (LAI): Methods, products, validation, and applications. *Reviews of Geophysics*, *57*(3), 739–799. https://doi.org/10.1029/2018rg000608

Farquhar, G. D., von Caemmerer, S., & Berry, J. A. (1980). A biochemical model of photosynthetic CO_2 assimilation in leaves of C_3 species. *Planta*, *149*(1), 78–90. https://doi.org/10.1007/bf00386231

Fekete, B. M., Vorosmarty, C., Hall, F., Collatz, G., Meeson, B., Los, S., et al. (2011). *ISLSCP II UNH/GRDC composite monthly runoff*. ORNL Distributed Active Archive Center. https://doi.org/10.3334/ORNLDAAC/994

Fisher, R. A., Koven, C. D., Anderegg, W. R. L., Christoffersen, B. O., Dietze, M. C., Farrior, C. E., et al. (2017). Vegetation demographics in Earth System Models: A review of progress and priorities. *Global Change Biology*, *24*(1), 35–54. https://doi.org/10.1111/gcb.13910

Foley, J. A., Prentice, I. C., Ramankutty, N., Levis, S., Pollard, D., Sitch, S., & Haxeltine, A. (1996). An integrated biosphere model of land surface processes, terrestrial carbon balance, and vegetation dynamics. *Global Biogeochemical Cycles*, *10*(4), 603–628. https://doi.org/10.1029/96gb02692

Frankenberg, C., Fisher, J. B., Worden, J., Badgley, G., Saatchi, S. S., Lee, J.-E., et al. (2011). New global observations of the terrestrial carbon cycle from GOSAT: Patterns of plant fluorescence with gross primary productivity. *Geophysical Research Letters*, *38*(17), L17706. https://doi.org/10.1029/2011gl048738

Friedlingstein, P., Jones, M. W., O'Sullivan, M., Andrew, R. M., Hauck, J., Peters, G. P., et al. (2019). Global carbon budget 2019. *Earth System Science Data*, *11*(4), 1783–1838. https://doi.org/10.5194/essd-11-1783-2019

Gillett, N. P., Shiogama, H., Funke, B., Hegerl, G., Knutti, R., Matthes, K., et al. (2016). The detection and attribution model intercomparison project (DAMIP v1.0) contribution to CMIP6. *Geoscientific Model Development*, *9*(10), 3685–3697. https://doi.org/10.5194/gmd-9-3685-2016

Ginoux, P., Chin, M., Tegen, I., Prospero, J. M., Holben, B., Dubovik, O., & Lin, S.-J. (2001). Sources and distributions of dust aerosols simulated with the GOCART model. *Journal of Geophysical Research*, *106*(D17), 20255–20273. https://doi.org/10.1029/2000jd000053

Grassl, H. (2000). Status and improvements of coupled general circulation models. *Science*, *288*(5473), 1991–1997. https://doi.org/10.1126/science.288.5473.1991

Guo, H., John, J. G., Blanton, C., McHugh, C., Nikonov, S., Radhakrishnan, A., et al. (2018). *NOAA-GFDL GFDL-CM4 model output prepared for CMIP6 CMIP historical*. Earth System Grid Federation. https://doi.org/10.22033/ESGF/CMIP6.8594

Hall, A., & Qu, X. (2006). Using the current seasonal cycle to constrain snow albedo feedback in future climate change. *Geophysical Research Letters*, *33*(3), L03502. https://doi.org/10.1029/2005gl025127

Harper, A. B., Wiltshire, A. J., Cox, P. M., Friedlingstein, P., Jones, C. D., Mercado, L. M., et al. (2018). Vegetation distribution and terrestrial carbon cycle in a carbon cycle configuration of JULES4.6 with new plant functional types. *Geoscientific Model Development*, *11*(7), 2857–2873. https://doi.org/10.5194/gmd-11-2857-2018

Held, I. M., Guo, H., Adcroft, A., Dunne, J. P., Horowitz, L. W., Krasting, J., et al. (2019). Structure and performance of GFDL's CM4.0 climate model. *Journal of Advances in Modeling Earth Systems*, *11*(11), 3691–3727. https://doi.org/10.1029/2019ms001829

Hillel, D. (1980). *Fundamentals of soil physics*. Academic Press.

Horowitz, L. W., Naik, V., Paulot, F., Ginoux, P. A., Dunne, J. P., Mao, J., et al. (2020). The GFDL global atmospheric chemistry-climate model AM4.1: Model description and simulation characteristics. *Journal of Advances in Modeling Earth Systems*, *12*(10), e2019MS002032. https://doi.org/10.1029/2019ms002032

Hurtt, G. C., Chini, L., Sahajpal, R., Frolking, S., Bodirsky, B. L., Calvin, K., et al. (2020). Harmonization of global land use change and management for the period 850-2100 (LUH2) for CMIP6. *Geoscientific Model Development*, *13*(11), 5425–5464. https://doi.org/10.5194/gmd-13-5425-2020

Ichoku, C., & Ellison, L. (2014). Global top-down smoke-aerosol emissions estimation using satellite fire radiative power measurements. *Atmospheric Chemistry and Physics*, *14*(13), 6643–6667. https://doi.org/10.5194/acp-14-6643-2014

IPCC. (2019). Summary for policymakers. In P. Shukla, J. Skea, E. Calvo Buendia, V. Masson-Delmotte, H.-O. Pörtner, D. C. Roberts, et al. (Eds.), *Climate change and land: An IPCC special report on climate change, desertification, land degradation, sustainable land management, food security, and greenhouse gas fluxes in terrestrial ecosystems*. In press. Retrieved from https://www.ipcc.ch/srccl/chapter/summary-for-policymakers/

Jackson, R. B., Canadell, J., Ehleringer, J. R., Mooney, H. A., Sala, O. E., & Schulze, E. D. (1996). A global analysis of root distributions for terrestrial biomes. *Oecologia*, *108*(3), 389–411. https://doi.org/10.1007/bf00333714

Jia, G., Shevliakova, E., Artaxo, P., De Noblet-Ducoudré, N., Houghton, R., House, J., et al. (2019). Land–climate interactions. In P. Shukla, J. Skea, E. Calvo Buendia, V. Masson-Delmotte, H.-O. Pörtner, D. C. Roberts, et al. (Eds.), *Climate change and land: An IPCC special report on climate change, desertification, land degradation, sustainable land management, food security, and greenhouse gas fluxes in terrestrial ecosystems*. In press. Retrieved from https://www.ipcc.ch/srccl/chapter/chapter-2/

Jones, B., & O'Neill, B. C. (2016). Spatially explicit global population scenarios consistent with the shared socioeconomic pathways. *Environmental Research Letters*, *11*(8), 084003. https://doi.org/10.1088/1748-9326/11/8/084003

Jones, C. D., Arora, V., Friedlingstein, P., Bopp, L., Brovkin, V., Dunne, J., et al. (2016). C4MIP – The coupled climate–carbon cycle model intercomparison project: Experimental protocol for CMIP6. *Geoscientific Model Development*, *9*(8), 2853–2880. https://doi.org/10.5194/gmd-9-2853-2016

Jones, H. G. (1983). *Plants and microclimate*. Cambridge University Press.

Jung, M., Reichstein, M., Margolis, H. A., Cescatti, A., Richardson, A. D., Arain, M. A., et al. (2011). Global patterns of land-atmosphere fluxes of carbon dioxide, latent heat, and sensible heat derived from eddy covariance, satellite, and meteorological observations. *Journal of Geophysical Research*, *116*, G00J07. https://doi.org/10.1029/2010jg001566

Kaiser, J. W., Heil, A., Andreae, M. O., Benedetti, A., Chubarova, N., Jones, L., et al. (2012). Biomass burning emissions estimated with a global fire assimilation system based on observed fire radiative power. *Biogeosciences*, *9*(1), 527–554. https://doi.org/10.5194/bg-9-527-2012

Kato, S., Rose, F. G., Rutan, D. A., Thorsen, T. J., Loeb, N. G., Doelling, D. R., et al. (2018). Surface irradiances of edition 4.0 clouds and the earth's radiant energy system (CERES) energy balanced and filled (EBAF) data product. *Journal of Climate*, *31*(11), 4501–4527. https://doi.org/10.1175/jcli-d-17-0523.1

Keller, D. P., Lenton, A., Scott, V., Vaughan, N. E., Bauer, N., Ji, D., et al. (2018). The carbon dioxide removal model intercomparison project (CDRMIP): Rationale and experimental protocol for CMIP6. *Geoscientific Model Development*, *11*(3), 1133–1160. https://doi.org/10.5194/gmd-11-1133-2018

Knutson, T. R., & Zeng, F. (2018). Model assessment of observed precipitation trends over land regions: Detectable human influences and possible low bias in model trends. *Journal of Climate*, *31*(12), 4617–4637. https://doi.org/10.1175/jcli-d-17-0672.1

Koffi, E. N., Rayner, P. J., Scholze, M., & Beer, C. (2012). Atmospheric constraints on gross primary productivity and net ecosystem productivity: Results from a carbon-cycle data assimilation system. *Global Biogeochemical Cycles*, *26*(1), GB1024. https://doi.org/10.1029/2010gb003900

Kottek, M., Grieser, J., Beck, C., Rudolf, B., & Rubel, F. (2006). World map of the Köppen-Geiger climate classification updated. *Meteorologische Zeitschrift*, *15*(3), 259–263. https://doi.org/10.1127/0941-2948/2006/0130

Koven, C. D., Knox, R. G., Fisher, R. A., Chambers, J., Christoffersen, B. O., Davies, S. J., et al. (2019). Benchmarking and parameter sensitivity of physiological and vegetation dynamics using the functionally assembled terrestrial ecosystem simulator (FATES) at Barro Colorado island, Panama. *Biogeosciences*, *17*(11), 3017–3044. https://doi.org/10.5194/bg-2019-409

Krasting, J. P., John, J. G., Blanton, C., McHugh, C., Nikonov, S., Radhakrishnan, A., et al. (2018). NOAA-GFDL GFDL-ESM4 model output prepared for CMIP6 CMIP [Dataset]. Earth System Grid Federation. https://doi.org/10.22033/ESGF/CMIP6.1407

Lawrence, D. M., Fisher, R. A., Koven, C. D., Oleson, K. W., Swenson, S. C., Bonan, G., et al. (2019). The community land model version 5: Description of new features, benchmarking, and impact of forcing uncertainty. *Journal of Advances in Modeling Earth Systems*, *11*(12), 4245–4287. https://doi.org/10.1029/2018ms001583

Lawrence, D. M., Hurtt, G. C., Arneth, A., Brovkin, V., Calvin, K. V., Jones, A. D., et al. (2016). The land use model intercomparison project (LUMIP) contribution to CMIP6: Rationale and experimental design. *Geoscientific Model Development*, *9*(9), 2973–2998. https://doi.org/10.5194/gmd-9-2973-2016

Lebecherel, L., Andréassian, V., & Perrin, C. (2013). On regionalizing the Turc-Mezentsev water balance formula. *Water Resources Research*, *49*(11), 7508–7517. https://doi.org/10.1002/2013wr013575

Lee, M., Shevliakova, E., Stock, C. A., Malyshev, S., & Milly, P. C. D. (2019). Prominence of the tropics in the recent rise of global nitrogen pollution. *Nature Communications*, *10*(1), 1437. https://doi.org/10.1038/s41467-019-09468-4

Lee, M., Stock, C. A., Dunne, J. P., & Shevliakova, E. (2023). Linking global terrestrial and ocean biogeochemistry with process-based, coupled freshwater algae-nutrient-solid dynamics in LM3-FANSY v1.0. *Geoscientific Model Development Discussions*, 1–42. https://doi.org/10.5194/gmd-2022-236

Leopold, L. B., & Maddock, T. (1953). The hydraulic geometry of stream channels and some physiographic implications. Professional Paper. https://doi.org/10.3133/pp252

Leuning, R. (1995). A critical appraisal of a combined stomatal-photosynthesis model for C_3 plants. *Plant, Cell and Environment*, *18*(4), 339–355. https://doi.org/10.1111/j.1365-3040.1995.tb00370.x

Li, D., Malyshev, S., & Shevliakova, E. (2016a). Exploring historical and future urban climate in the earth system modeling framework: 1. Model development and evaluation. *Journal of Advances in Modeling Earth Systems*, *8*(2), 917–935. https://doi.org/10.1002/2015MS000578

Li, D., Malyshev, S., & Shevliakova, E. (2016b). Exploring historical and future urban climate in the earth system modeling framework: 2. Impact of urban land use over the continental United States. *Journal of Advances in Modeling Earth Systems*, *8*(2), 936–953. https://doi.org/10.1002/2015MS000579

Longo, M., Knox, R. G., Medvigy, D. M., Levine, N. M., Dietze, M. C., Kim, Y., et al. (2019). The biophysics, ecology, and biogeochemistry of functionally diverse, vertically and horizontally heterogeneous ecosystems: The ecosystem demography model, version 2.2 – Part 1: Model description. *Geoscientific Model Development*, *12*(10), 4309–4346. https://doi.org/10.5194/gmd-12-4309-2019

Mahowald, N., Lo, F., Zheng, Y., Harrison, L., Funk, C., Lombardozzi, D., & Goodale, C. (2016). Projections of leaf area index in Earth System Models. *Earth System Dynamics*, *7*(1), 211–229. https://doi.org/10.5194/esd-7-211-2016

Martínez-Cano, I., Shevliakova, E., Malyshev, S., John, J. G., Yu, Y., Smith, B., & Pacala, S. W. (2022). Abrupt loss and uncertain recovery from fires of Amazon forests under low climate mitigation scenarios. *Proceedings of the National Academy of Sciences*, *119*(52), e2203200119. https://doi.org/10.1073/pnas.2203200119

Martínez Cano, I., Shevliakova, E., Malyshev, S., Wright, S. J., Detto, M., Pacala, S. W., & Muller-Landau, H. C. (2020). Allometric constraints and competition enable the simulation of size structure and carbon fluxes in a dynamic vegetation model of tropical forests (LM3PPA-TV). *Global Change Biology*, *26*(8), 4478–4494. https://doi.org/10.1111/gcb.15188

Mauritsen, T., Bader, J., Becker, T., Behrens, J., Bittner, M., Brokopf, R., et al. (2019). Developments in the MPI-m Earth System Model version 1.2 (MPI-ESM1.2) and its response to increasing CO_2. *Journal of Advances in Modeling Earth Systems*, *11*(4), 998–1038. https://doi.org/10.1029/2018ms001400

Meador, W. E., & Weaver, W. R. (1980). Two-stream approximations to radiative transfer in planetary atmospheres: A unified description of existing methods and a new improvement. *Journal of the Atmospheric Sciences*, *37*(3), 630–643. https://doi.org/10.1175/1520-0469(1980)037⟨0630:tsatrt⟩2.0.co;2

Medvigy, D., Wofsy, S. C., Munger, J. W., Hollinger, D. Y., & Moorcroft, P. R. (2009). Mechanistic scaling of ecosystem function and dynamics in space and time: Ecosystem Demography model version 2. *Journal of Geophysical Research*, *114*(G1), G01002. https://doi.org/10.1029/2008jg000812

Milly, P. C. D., Malyshev, S. L., Shevliakova, E., Dunne, K. A., Findell, K. L., Gleeson, T., et al. (2014). An enhanced model of land water and energy for global hydrologic and earth-system studies. *Journal of Hydrometeorology*, *15*(5), 1739–1761. https://doi.org/10.1175/jhm-d-13-0162.1

Moorcroft, P. R., Hurtt, G. C., & Pacala, S. W. (2001). A method for scaling vegetation dynamics: The ecosystem demography model (ED). *Ecological Monographs*, *71*(4), 557–586. https://doi.org/10.1890/0012-9615(2001)071[0557:amfsvd]2.0.co;2

Morillas, L., Hund, S. V., & Johnson, M. S. (2019). Water use dynamics in double cropping of rainfed upland rice and irrigated melons produced under drought-prone tropical conditions. *Water Resources Research*, *55*(5), 4110–4127. https://doi.org/10.1029/2018wr023757

Myneni, R., Knyazikhin, Y., & Park, T. (2015). *MOD15A2H MODIS/Terra leaf area index/FPAR 8-day L4 global 500 m SIN grid V006*. NASA EOSDIS Land Processes DAAC.

O'Neill, B. C., Tebaldi, C., van Vuuren, D. P., Eyring, V., Friedlingstein, P., Hurtt, G., et al. (2016). The scenario model intercomparison project (ScenarioMIP) for CMIP6. *Geoscientific Model Development*, *9*(9), 3461–3482. https://doi.org/10.5194/gmd-9-3461-2016

O'Neill, P. E., Chan, S., Njoku, E. G., Jackson, T., & Bindlish, R. (2019). *SMAP L3 radiometer global daily 36 km EASE-grid soil moisture, version 6*. NASA National Snow and Ice Data Center Distributed Active Archive Center. https://doi.org/10.5067/EVYDQ32FNWTH

Pan, X., Ichoku, C., Chin, M., Bian, H., Darmenov, A., Colarco, P., et al. (2019). Six global biomass burning emission datasets: Inter-comparison and application in one global aerosol model. *Atmospheric Chemistry and Physics Discussions*, *20*(2), 969–994. https://doi.org/10.5194/acp-2019-475

Paulot, F., Malyshev, S., Nguyen, T., Crounse, J. D., Shevliakova, E., & Horowitz, L. W. (2018). Representing sub-grid scale variations in nitrogen deposition associated with land use in a global Earth System Model: Implications for present and future nitrogen deposition fluxes over North America. *Atmospheric Chemistry and Physics*, *18*(24), 17963–17978. https://doi.org/10.5194/acp-18-17963-2018

Peel, M. C., Finlayson, B. L., & McMahon, T. A. (2007). Updated world map of the Köppen-Geiger climate classification. *Hydrology and Earth System Sciences*, *11*(5), 1633–1644. https://doi.org/10.5194/hess-11-1633-2007

Pinty, B., Lavergne, T., Dickinson, R. E., Widlowski, J.-L., Gobron, N., & Verstraete, M. M. (2006). Simplifying the interaction of land surfaces with radiation for relating remote sensing products to climate models. *Journal of Geophysical Research*, *111*(D2), D02116. https://doi.org/10.1029/2005jd005952

Portmann, F. T., Siebert, S., & Döll, P. (2010). MIRCA2000-global monthly irrigated and rainfed crop areas around the year 2000: A new high-resolution data set for agricultural and hydrological modeling. *Global Biogeochemical Cycles*, *24*(1), GB1011. https://doi.org/10.1029/2008gb003435

Priestley, C. H. B., & Taylor, R. J. (1972). On the assessment of surface heat flux and evaporation using large-scale parameters. *Monthly Weather Review*, *100*(2), 81–92. https://doi.org/10.1175/1520-0493(1972)100<0081:OTAOSH>2.3.CO;2

Prospero, J. M. (1996). The atmospheric transport of particles to the ocean. In V. Ittekkot, P. Schaffer, S. Honjo, & P. J. Depetris (Eds.), *Particle flux in the ocean*. John Wiley.

Pu, B., Ginoux, P., Guo, H., Hsu, N. C., Kimball, J., Marticorena, B., et al. (2020). Retrieving the global distribution of the threshold of wind erosion from satellite data and implementing it into the geophysical fluid dynamics laboratory land–atmosphere model (gfdl am4.0/lm4.0). *Atmospheric Chemistry and Physics*, *20*(1), 55–81. https://doi.org/10.5194/acp-20-55-2020

Qu, X., & Hall, A. (2006). Assessing snow albedo feedback in simulated climate change. *Journal of Climate*, *19*(11), 2617–2630. https://doi.org/10.1175/jcli3750.1

Rabin, S. S., Magi, B. I., Shevliakova, E., & Pacala, S. W. (2015). Quantifying regional, time-varying effects of cropland and pasture on vegetation fire. *Biogeosciences*, *12*(22), 6591–6604. https://doi.org/10.5194/bg-12-6591-2015

Rabin, S. S., Ward, D. S., Malyshev, S. L., Magi, B. I., Shevliakova, E., & Pacala, S. W. (2018). A fire model with distinct crop, pasture, and non-agricultural burning: Use of new data and a model-fitting algorithm for FINAL.1. *Geoscientific Model Development*, *11*(2), 815–842. https://doi.org/10.5194/gmd-11-815-2018

Reick, C. H., Gayler, V., Goll, D., Hagemann, S., Heidkamp, M., Nabel, J. E. M. S., et al. (2021). JSBACH 3—The land component of the MPI Earth System Model: Documentation of version 3.2. *Berichte zur Erdsystemforschung*, *240*. https://doi.org/10.17617/2.3279802

Rohde, R., Muller, R. A., Jacobsen, R., Muller, E., & Wickham, C. (2013). A new estimate of the average earth surface land temperature spanning 1753 to 2011. *Geoinformatics and Geostatistics: An Overview*, *1*, 1. https://doi.org/10.4172/2327-4581.1000101

Running, S. W., & Zhao, M. (2015). *Daily GPP and annual NPP (MOD17A2/A3) products NASA earth observing system MODIS land algorithm (MOD17 User's Guide)*. NASA.

Santoro, M., Beaudoin, A., Beer, C., Cartus, O., Fransson, J. E., Hall, R. J., et al. (2015). Forest growing stock volume of the northern hemisphere: Spatially explicit estimates for 2010 derived from Envisat ASAR. *Remote Sensing of Environment*, *168*, 316–334. https://doi.org/10.1016/j.rse.2015.07.005

Schneider, U., Becker, A., Finger, P., Meyer-Christoffer, A., & Ziese, M. (2018). GPCC full data monthly product version 2018 at 0.5°: Monthly land-surface precipitation from rain-gauges built on GTS-based and historical data. https://doi.org/10.5676/DWD_GPCC/FD_M_V2018_050

Sellar, A. A., Jones, C. G., Mulcahy, J. P., Tang, Y., Yool, A., Wiltshire, A., et al. (2019). UKESM1: Description and evaluation of the U.K. Earth System Model. *Journal of Advances in Modeling Earth Systems*, *11*(12), 4513–4558. https://doi.org/10.1029/2019ms001739

Shangguan, W., Dai, Y., Duan, Q., Liu, B., & Yuan, H. (2014). A global soil data set for earth system modeling. *Journal of Advances in Modeling Earth Systems*, *6*(1), 249–263. https://doi.org/10.1002/2013ms000293

Shevliakova, E., Pacala, S. W., Malyshev, S., Hurtt, G. C., Milly, P. C. D., Caspersen, J. P., et al. (2009). Carbon cycling under 300 years of land use change: Importance of the secondary vegetation sink. *Global Biogeochemical Cycles*, *23*(2), GB2022. https://doi.org/10.1029/2007gb003176

Shevliakova, E., Stouffer, R. J., Malyshev, S., Krasting, J. P., Hurtt, G. C., & Pacala, S. W. (2013). Historical warming reduced due to enhanced land carbon uptake. *Proceedings of the National Academy of Sciences*, *110*(42), 16730–16735. https://doi.org/10.1073/pnas.1314047110

Shi, X., Lohmann, G., Sidorenko, D., & Yang, H. (2020). Early-Holocene simulations using different forcings and resolutions in AWI-ESM. *The Holocene*, *30*(7), 996–1015. https://doi.org/10.1177/0959683620908634

Shinozaki, K., Yoda, K., Hozumi, K., & Kira, T. (1964). A quantitative analysis of plant form-the pipe model theory: II. Further evidence of the theory and its application in forest ecology. *Japanese Journal of Ecology*, *14*(4), 133–139. https://doi.org/10.18960/seitai.14.4_133

Siegenthaler, U., & Oeschger, H. (1978). Predicting future atmospheric carbon dioxide levels. *Science*, *199*(4327), 388–395. https://doi.org/10.1126/science.199.4327.388

Smith, B., Prentice, I. C., & Sykes, M. T. (2001). Representation of vegetation dynamics in the modelling of terrestrial ecosystems: Comparing two contrasting approaches within European climate space. *Global Ecology and Biogeography*, *10*(6), 621–637. https://doi.org/10.1046/j.1466-822x.2001.t01-1-00256.x

Smith, B., Wårlind, D., Arneth, A., Hickler, T., Leadley, P., Siltberg, J., & Zaehle, S. (2014). Implications of incorporating N cycling and N limitations on primary production in an individual-based dynamic vegetation model. *Biogeosciences*, *11*(7), 2027–2054. https://doi.org/10.5194/bg-11-2027-2014

Sperry, J. S., Adler, F. R., Campbell, G. S., & Comstock, J. P. (1998). Limitation of plant water use by rhizosphere and xylem conductance: Results from a model. *Plant, Cell and Environment*, *21*(4), 347–359. https://doi.org/10.1046/j.1365-3040.1998.00287.x

Stevens, B., Giorgetta, M., Esch, M., Mauritsen, T., Crueger, T., Rast, S., et al. (2013). Atmospheric component of the MPI-M Earth system model: ECHAM6. *Journal of Advances in Modeling Earth Systems*, *5*(2), 146–172. https://doi.org/10.1002/jame.20015

Stock, C. A., Dunne, J. P., Fan, S., Ginoux, P., John, J., Krasting, J. P., et al. (2020). Ocean biogeochemistry in GFDL's Earth System Model 4.1 and its response to increasing atmospheric CO_2. *Journal of Advances in Modeling Earth Systems*, *12*(10), e2019MS002043. https://doi.org/10.1029/2019ms002043

Strigul, N., Pristinski, D., Purves, D., Dushoff, J., & Pacala, S. (2008). Scaling from trees to forests: Tractable macroscopic equations for forest dynamics. *Ecological Monographs*, *78*(4), 523–545. https://doi.org/10.1890/08-0082.1

Sulman, B. N., Phillips, R. P., Oishi, A. C., Shevliakova, E., & Pacala, S. W. (2014). Microbe-driven turnover offsets mineral-mediated storage of soil carbon under elevated CO_2. *Nature Climate Change*, *4*(12), 1099–1102. https://doi.org/10.1038/nclimate2436

Sulman, B. N., Shevliakova, E., Brzostek, E. R., Kivlin, S. N., Malyshev, S., Menge, D. N., & Zhang, X. (2019). Diverse mycorrhizal associations enhance terrestrial C storage in a global model. *Global Biogeochemical Cycles*, *33*(4), 501–523. https://doi.org/10.1029/2018gb005973

Taylor, K. E., Stouffer, R. J., & Meehl, G. A. (2012). An overview of CMIP5 and the experiment design. *Bulletin of the American Meteorological Society*, *93*(4), 485–498. https://doi.org/10.1175/bams-d-11-00094.1

van der Werf, G. R., Randerson, J. T., Giglio, L., van Leeuwen, T. T., Chen, Y., Rogers, B. M., et al. (2017). Global fire emissions estimates during 1997-2016. *Earth System Science Data*, *9*(2), 697–720. https://doi.org/10.5194/essd-9-697-2017

Wang, A., & Zeng, X. (2013). Development of global hourly 0.5° land surface air temperature datasets. *Journal of Climate*, *26*(19), 7676–7691. https://doi.org/10.1175/jcli-d-12-00682.1

Wang, W., Dungan, J., Hashimoto, H., Michaelis, A. R., Milesi, C., Ichii, K., & Nemani, R. R. (2011). Diagnosing and assessing uncertainties of terrestrial ecosystem models in a multimodel ensemble experiment: 1. Primary production. *Global Change Biology*, *17*(3), 1350–1366. https://doi.org/10.1111/j.1365-2486.2010.02309.x

Ward, D. S., Shevliakova, E., Malyshev, S., & Rabin, S. (2018). Trends and variability of global fire emissions due to historical anthropogenic activities. *Global Biogeochemical Cycles*, *32*(1), 122–142. https://doi.org/10.1002/2017gb005787

Wei, Z., Yoshimura, K., Wang, L., Miralles, D. G., Jasechko, S., & Lee, X. (2017). Revisiting the contribution of transpiration to global terrestrial evapotranspiration. *Geophysical Research Letters*, *44*(6), 2792–2801. https://doi.org/10.1002/2016gl072235

Welp, L. R., Keeling, R. F., Meijer, H. A. J., Bollenbacher, A. F., Piper, S. C., Yoshimura, K., et al. (2011). Interannual variability in the oxygen isotopes of atmospheric CO_2 driven by El Niño. *Nature*, *477*(7366), 579–582. https://doi.org/10.1038/nature10421

Weng, E., Farrior, C. E., Dybzinski, R., & Pacala, S. W. (2016). Predicting vegetation type through physiological and environmental interactions with leaf traits: Evergreen and deciduous forests in an earth system modeling framework. *Global Change Biology*, *23*(6), 2482–2498. https://doi.org/10.1111/gcb.13542

Weng, E., Malyshev, S., Lichstein, J. W., Farrior, C. E., Dybzinski, R., Zhang, T., et al. (2015). Scaling from individual trees to forests in an Earth system modeling framework using a mathematically tractable model of height-structured competition. *Biogeosciences*, *12*(9), 2655–2694. https://doi.org/10.5194/bg-12-2655-2015

Whittaker, R. H. (1970). *Communities and ecosystems*. MacMillan.

Wolf, A., Anderegg, W. R. L., & Pacala, S. W. (2016). Optimal stomatal behavior with competition for water and risk of hydraulic impairment. *Proceedings of the National Academy of Sciences*, *113*(46), E7222–E7230. https://doi.org/10.1073/pnas.1615144113

Woodwell, G. M., & Whittaker, R. H. (1968). Primary production in terrestrial ecosystems. *American Zoologist*, *8*(1), 19–30. https://doi.org/10.1093/icb/8.1.19

Xie, J., Xie, Z., Jia, B., Qin, P., Liu, B., Wang, L., et al. (2021). Coupling of the CAS-LSM land-surface model with the CAS-FGOALS-g3 climate system model. *Journal of Advances in Modeling Earth Systems*, *13*(1), e2020MS002171. https://doi.org/10.1029/2020ms002171

Yokohata, T., Kinoshita, T., Sakurai, G., Pokhrel, Y., Ito, A., Okada, M., et al. (2020). MIROC-INTEG-LAND version 1: A global biogeochemical land surface model with human water management, crop growth, and land-use change. *Geoscientific Model Development*, *13*(10), 4713–4747. https://doi.org/10.5194/gmd-13-4713-2020

Yu, Y., Dunne, J. P., Shevliakova, E., Ginoux, P., Malyshev, S., John, J. G., & Krasting, J. P. (2021). Increased risk of the 2019 Alaskan July fires due to anthropogenic activity. *Bulletin of the American Meteorological Society*, *102*(1), S1–S7. https://doi.org/10.1175/bams-d-20-0154.1

Yu, Y., & Ginoux, P. (2022). Enhanced dust emission following large wildfires due to vegetation disturbance. *Nature Geoscience*, *15*(11), 878–884. https://doi.org/10.1038/s41561-022-01046-6

Zhang, Y., Knutson, T. R., Shevliakova, E., & Paynter, D. (2023). The long-term trends of global land precipitation in GFDL's CM4 and ESM4 climate models. *Journal of Climate*, *36*(18), 1–55. https://doi.org/10.1175/jcli-d-22-0764.1

Zhang, Y., Peña-Arancibia, J. L., McVicar, T. R., Chiew, F. H. S., Vaze, J., Liu, C., et al. (2016). Multi-decadal trends in global terrestrial evapotranspiration and its components. *Scientific Reports*, *6*(1), 19124. https://doi.org/10.1038/srep19124

Zhao, M., Golaz, J.-C., Held, I. M., Guo, H., Balaji, V., Benson, R., et al. (2018). The GFDL global atmosphere and land model AM4.0/LM4.0: 1. Simulation characteristics with prescribed SSTs. *Journal of Advances in Modeling Earth Systems*, *10*(3), 691–734. https://doi.org/10.1002/2017ms001208

Zhao, M., Heinsch, F. A., Nemani, R. R., & Running, S. W. (2005). Improvements of the MODIS terrestrial gross and net primary production global data set. *Remote Sensing of Environment*, *95*(2), 164–176. https://doi.org/10.1016/j.rse.2004.12.011

Zhu, Q., Riley, W. J., Tang, J., Collier, N., Hoffman, F. M., Yang, X., & Bisht, G. (2019). Representing nitrogen, phosphorus, and carbon interactions in the E3SM land model: Development and global benchmarking. *Journal of Advances in Modeling Earth Systems*, *11*(7), 2238–2258. https://doi.org/10.1029/2018ms001571

Zhu, Z., Bi, J., Pan, Y., Ganguly, S., Anav, A., Xu, L., et al. (2013). Global data sets of vegetation leaf area index (LAI)3g and fraction of photosynthetically active radiation (FPAR)3g derived from global inventory modeling and mapping studies (GIMMS) normalized difference vegetation index (NDVI3g) for the period 1981 to 2011. *Remote Sensing*, *5*(2), 927–948. https://doi.org/10.3390/rs5020927